Reconstruction of Star Formation Histories of Resolved Stellar Populations

Andrew E. Dolphin

A dissertation submitted in partial fulfillment
of the requirements for the degree of

Doctor of Philosophy

University of Washington

1999

Program Authorized to Offer Degree: Astronomy

University of Washington

Graduate School

This is to certify that I have examined this copy of a doctoral dissertation by

Andrew E. Dolphin

and have found that it is complete and satisfactory in all respects,

and that any and all revisions required by the final

examining committee have been made.

Chair of Supervisory Committee:

Paul Hodge

Reading Committee:

Gary Christian

Julianne Dalcanton

Gene Magnier

Tom Quinn

Chris Stubbs

Date:

University of Washington

Abstract

Reconstruction of Star Formation Histories of Resolved Stellar Populations

by Andrew E. Dolphin

Chair of Supervisory Committee

Professor Paul Hodge
Astronomy

A method for the study of star formation histories of resolved galaxies is presented. It is tested with both simulated data of a composite population and observed data of a globular cluster, which is expected to be a single population. The method is then used to study the star formation histories of WLM, the LMC, and LGS 3.

For WLM, HST F555W and F814W photometry of a portion of the galaxy is presented, with the chips aligned such that sample of both the bar and halo populations were present in the data. The distance modulus for the globular cluster is calculated to be 24.72 $\pm$ 0.09 from color-magnitude diagram fitting, with [Fe/H] of -1.51 $\pm$ 0.09 and age of 14.8 $\pm$ 0.7 Gyr. The distance is consistent with distances calculated for the cluster HB and the field star TRGB. Large-scale star formation in the galaxy began about 12 Gyr with a short but large burst. Intermediate age star formation rates are uncertain, but the bar has shown increased star formation during the past 1.5 Gyr.

The LMC data is ground-based UBV photometry of two fields in the northern part of the disk. A distance modulus of 18.40 $\pm$ 0.05 is calculated. Large-scale star formation began about 12 Gyr ago in this part of the LMC with a large burst, and

slowly decreased. A recent burst began between 1.0 and 2.5 Gyr ago, and shows different recent star formation rates in the two fields.

The LGS 3 data is HST-based F555W and F814W photometry, and includes most of the galaxy's core and part of the galaxy's halo. The distance modulus is calculated to be 23.89 ± 0.05, and is consistent with HB and TRGB distances. LGS 3 had two bursts of star formation, one beginning 14.5 ± 0.8 Gyr ago and one beginning between 2.5 and 5 Gyr ago, and ending at least 200 Myr ago. The recent burst was constrained to the body of the galaxy.

TABLE OF CONTENTS

LIST OF FIGURES

LIST OF TABLES

ACKNOWLEDGMENTS

I wish to thank my advisor, Paul Hodge, for his encouragement and insightful comments during the past few years. I also appreciate the comments and questions raised during group meetings by John Collier, Knut Olsen, Brooke Skelton, Dan Zucker, and Ted Wyder, as well as the collaborations with Knut Olsen and Ted Wyder using the method developed here on HST data for the LMC and M100.

Chapter 1

INTRODUCTION

The study of star formation histories of galaxies is an attempt to build a time machine to view the past. While observations at high redshift provide a "large picture" view of the history of the universe, they do not have the ability to follow the evolution of a single galaxy over the many billions of years since its formation. Studies of the star formation histories of specific galaxies, while not giving the direct images of their previous states, do guarantee that measurements of the past are directly related to observations of the present. This can be an exceedingly difficult task, however, as the stellar populations left behind by past star formation are extremely difficult to untangle.

Despite the difficulties involved, star formation history studies are critical to our understanding of the evolution of the universe. Studies of isolated galaxies will constrain models of how galaxies evolve over time, setting limits on star formation rates and metallicity enrichment. Studies of interacting (or previously interacting) galaxies will help constrain our understanding of the long-term global effects of an interaction or merger of galaxies.

The presence or absence of certain indicators, such as RR Lyrae stars, Cepheids, AGB stars, and other unique stages of stellar evolution, can give only a qualitative account of a galaxy's history. For example, if a galaxy contains RR Lyrae stars we can be certain that its contains a very old (13 Gyr or older) population. However, the comparison of *all* stars with those predicted from models, despite difficulties, will succeed in producing a star formation history with much smaller uncertainties. Because getting spectra of a large fraction of the stars in a galaxy is impossible, these studies will be will be made by examining the color-magnitude diagrams (CMDs) of galaxies' stars. This study will concentrate on attempting to find the star formation history that would best reconstruct the observed CMD giving the stellar evolutionary models available.

This will require three major steps. The first will be to develop a method for such a study and the second will be to test the accuracy of the method by application to synthetic data with known star formation histories, as well as application to observed data with well-constrained star formation histories. Both of these will be done in chapter 2. The remaining chapters will apply the method to observed data for three galaxies: WLM, the LMC, and LGS 3.

1.1 Methods of Reconstructing Star Formation Histories

The use of evolutionary models for studying composite stellar populations is a relatively new science. One early such work was by Ferraro et al (1989), who generated a set of synthetic CMDs based on guesses of plausible star formation histories of WLM. These synthetic CMDs were based on five sets of evolutionary models, and used incompleteness and standard photometric errors to simulate the observed data quality. Comparisons of the data with the synthetic CMDs were made subjectively, rather than by a detailed quantitative comparison. Although this technique is rather qualitative compared with current techniques, the fundamentals - generating synthetic CMDs and comparing with observed data - are still in use.

Two major improvements to this method were made by Gallart et al (1996) in their study of NGC 6822. First was the model generation, which although still confined to a small number of potential star formation histories, used artificial star results rather than photometric errors for the generation of the synthetic CMDs. The effect was that non-symmetric errors were introduced, providing an accurate simulation of the observational effect that stars tend to be scattered towards brighter magnitudes and average colors. Second was the comparison technique, which found eight quantitative parameters for the fitting. Rather than merely making a qualitative look at the synthetic and observed CMDs, it was now possible to give a proposed star formation history a grade based on how well it fit each of the eight parameters.

Tolstoy & Saha (1996) proposed that a single fit parameter be used, rather than a subjective comparison or an application of many parameters. (In fact, Tosi et al 1991 had remarked that a single fit parameter could not be used for such work.) Their fit parameter was derived using Bayesian inference, and was similar to a χ^2, which was employed by Tolstoy (1996) in an analysis of Leo A's stellar population. In practice, a single fit parameter was only partially used, as the constituents of the fit were broken up and analyzed as a set. Still, this marked a major step forward from merely finding a set of good fits towards finding the *best* fit.

Despite the improvements, the state of the field is still one that is limited by methodology rather than by the available data or evolutionary models. What is needed is a method that, first, can generate an enormous number of accurate synthetic CMDs quickly, which will allow for a much larger search of parameter space than the previous, relatively limited studies. With such a CMD generation procedure, it will be possible to solve for not only past star formation rates, but also the chemical enrichment history, distance, and extinction. Second, the method must determine a single fit parameter that can decisively determine the star formation history best fitting the observed data. This will allow for an automatic processing of the generated CMDs, which will create faster and more objective star formation history results. A method meeting these criteria is what is proposed and tested in Chapter 2.

1.2 Populations of Local Group Galaxies

1.2.1 Wolf-Lundmark-Melotte (WLM)

The WLM galaxy (DDO 221) is a Local Group dwarf irregular (class Irr IV-V), in an isolated part of the Local Group approximately 900 kpc from the Milky Way. It was discovered by Wolf (1909) and rediscovered by Lundmark and Melotte (Melotte 1926), thus earning its name of Wolf-Lundmark-Melotte, abbreviated WLM. Its distance is approximately 900 kpc, making it close enough to allow ground-based studies of its red giant branch (RGB) tip ($V =\sim 22.5$) and upper main sequence, but distant enough that such studies will not reach the horizontal branch ($V =\sim 25.4$).

The galaxy has a total mass of $1.5 \times 10^8 M_\odot$, about 40% of which is neutral HI (Mateo 1998). Hodge & Miller (1995) identified 21 HII regions in the galaxy, with a total H_α luminosity of 1.2×10^{38} ergs/sec. Thus it has active star formation at present, although with a formation timescale (average SFR divided by current SFR) of 150 Gyr, its current star formation rate is only $\sim$10% of its lifetime average.

Ables & Ables (1977) used electrographic techniques to make photometric measurements of supergiants in WLM, getting B and V photometry for 50 stars, the faintest having a magnitude B of 21.6. With this photometry, they were able to estimate a distance modulus of $(m - M) = 26.23 \pm 0.14$. They also noted a "slightly diffuse starlike object about 2' west of the center" of the galaxy, which they determined was most likely a globular cluster with $V = 16.56$ and $(B-V) = 0.67$. Finally, they made contour maps in B and V of the galaxy, finding a color gradient with $(B - V) = 0.26$ in the core and $(B - V) = 0.95$ in the outer regions. Sandage & Carlson (1985) studied the brightest supergiants in WLM using a photometer and determined periods for 15 Cepheids. With the Cepheid results, the distance modulus was heavily revised to $(m - M) = 24.93$, a drop of 1.3 magnitudes.

The first CCD study of this galaxy was made by Ferraro et al (1989), with later work made by Minniti & Zijlstra (1997). Both works reached $V =\sim 24$, deep enough to accurately measure the RGB tip but not the HB. The Ferraro et al (1989) data consisted of two fields, both partially in the bar and partially in the halo. They were able to conclude that the two fields had different star formation rates in the very recent past (and therefore that WLM's star formation was localized rather than global), and that a Salpeter IMF was adequate for their data.

Minniti & Zijlstra (1997) made a V and I study of WLM, which allowed them to study the older stars in greater detail. They found that star formation began at least 10 Gyr ago in the galaxy, with a metallicity [Fe/H] of -1.45 $\pm$ 0.2. A distance modulus of $(m-M)_0 = 24.75 \pm 0.1$ was calculated from the RGB tip. Importantly, they observed that there was a lack of bright main sequence stars in the galaxy's halo, and therefore the color gradient observed by Ables & Ables (1977) was due to a stellar population gradient.

With HST, we are able to go far deeper than previous studies, beyond V of 27, with image clarity that provides outstanding stellar photometry. This will provide an opportunity to refine the distance measurements and study the stellar populations in much greater detail with quantitative results, which are presented in Chapter 3. Additionally, the resolution of HST transforms Ables & Ables' "slightly diffuse starlike object" into a resolved globular cluster, which is used in Chapter 2 to test the star formation history technique.

1.2.2 Large Magellanic Cloud (LMC)

The LMC is the Milky Way's best-studied companion galaxy, a result of both its proximity (~50 kpc) and high galactic latitude. Its stellar content is easily accessible from ground-based telescopes, allowing 1m-class telescopes to obtain effectively deeper data than the HST can in more distant Local Group members such as WLM and LGS 3.

The global properties of the LMC are well-studied, with a total mass of $3.5 \times 10^9 M_\odot$ and neutral gas mass of $5.2 \times 10^8 M_\odot$ (15% of the total), including HeI, determined by Kim et al (1998b). Kim et al (1998a) also overlaid an Hα map over their HI map, showing the Hα to be concentrated around the 30 Doradus region and scattered elsewhere in the galaxy.

As a result of the LMC's proximity, much work has already been done on this subject, much of which is well summarized in a review by Olszewski et al (1996). The brightest star clusters, which are relatively easy to date, seem to have mostly formed in the past 4 Gyr, with the remaining clusters formed over 12 Gyr ago. The clusters also show a rise in metallicity over the galaxy's history, from -1.8 15 Gyr ago to -0.5 at present, both values with a spread of ± 0.5 dex. Whether the formation times and metallicities of the clusters trace those of the global star formation, however, is uncertain.

The distribution of ages of the field stars is more difficult to measure. An early attempt at studying the disk stars was made by Butcher (1977), who identified a break in the main-sequence LF as indicating that most of the stars have been formed in the past 3-5 Gyr. A study of the star formation history of the LMC field stars using comparisons with synthetic CMDs was made by Bertelli et al (1992), which confirmed the Butcher (1977) results. It was determined that a burst of star formation activity began some 3-5 Gyr ago, with a star formation rate as high as ten times the rate at older ages. These results confirm the expectations from the cluster studies.

Recently, however, HST results have brought this seemingly firm picture into question. Holtzman et al (1997) take HST data for the same field studied by Butcher (1977) and Bertelli et al (1992), and obtain a different result. They find that the star formation rate increase happened more recently (2-3 Gyr ago) and that, more importantly, the rate increase was only approximately a factor of 3. This result was confirmed with the addition of ground-based data of the same field and surrounding regions by Stappers et al (1997), and Geha et al (1998) find that this star formation history is also correct for two other outer LMC fields. It has also been hinted that the star formation rates may have begun to decrease during the past Gyr.

Olsen (1998) studied the HST field surrounding NGC 1754, which also lies in the northern part of the disk, as well as the fields surrounding four globular clusters in the bar. Using a method much like that used in this work, he found that the Holtzman et al (1997) results were qualitatively correct, but that the star formation enhancement during the past 3 Gyr has not been a uniform star formation rate. Olsen (1998) also finds evidence of the decrease in star formation rate during the past 0.5 Gyr.

Chapter 4 presents additional ground-based photometry of two fields in the northern part of the LMC disk, with an analysis of the star formation history of those regions.

1.2.3 LGS 3

LGS 3, sometimes known as the Pisces dwarf, was discovered by Karachentseva (1976), and is one of the less luminous galaxies in the Local Group (Mateo 1998). The galaxy has a total mass of $2.1 \times 10^7 M_\odot$ (Mateo 1998), with an HI mass of $4.2 \times 10^5 M_\odot$ (Young & Lo 1997), or about 2% of the total mass of the galaxy. (For comparison, Mateo (1998) lists no dwarf irregular galaxies with HI masses less than $2 \times 10^6 M_\odot$.) Hodge & Miller (1995) found no HII regions in LGS 3, indicating that there is little or no star formation at the present time. These facts place LGS 3 into the transition category of irregular/spheroidal galaxies, as it does not have the HII luminosity and high gas mass typical of irregulars, but has a higher fraction of gas mass than most dwarf spheroidals. (Mateo (1998) lists no dwarf spheroidal or elliptical galaxies with HI fractions greater than 0.4%.)

Since its relatively recent discovery, LGS 3 has been the target of several stellar population studies, such as that by Schild (1980). Two distance estimates were attempted with the data (CCD photometry to $R = 18.6$), both of which were highly uncertain and inconsistent with each other. A measurement assuming that the stellar population was similar to that of that dwarf spheroidal Sculptor gave $(m-M) = 21.7$, while one assuming it was an irregular (Sandage & Tammann 1974) produced a value of $(m-M) = 29.4$. We now know that the galaxy is an intermediate type dwarf, and interestingly, the current value of 24.54 ± 0.15, as quoted by Mateo (1998), lies nearly halfway in magnitude between those two. An improvement on this work was made by Christian & Tully (1983), who obtained R photometry of 66 stars and VR photometry of 17. Although their data was not deep enough to study the star formation history, they were able to constrain the galaxy's distance to between 0.7 and 1.2 Mpc ($(m-M)$ between 24.2 and 25.4), with the actual value depending on the ages of the stars.

Lee (1995) presented a CMD of LGS 3 that contained 490 stars. With these data, parameters of the galaxy could begin to be more firmly established. Lee used the IRGB tip method to find a distance modulus of $(m-M)_0 = 24.54 \pm 0.21$, using an extinction $A_V = 0.08$ adopted from Burstein & Heiles (1984). The mean metallicity of the RGB stars was found to be $[Fe/H] = -2.10 \pm 0.22$.

Mould (1997) and Aparicio et al (1997) have begun the study of the galaxy's star formation history. Aparicio et al (1997) used photometry to constrain the distance modulus, obtaining a best value of $(m-M)_0 = 24.43 \pm 0.04$, using an extinction $A_V = 0.12$, also adopted from Burstein & Heiles (1984). However, they also found an alternate distance of $(m-M)_0 = 24.93 \pm 0.03$ that gave moderately good fits to the data. These papers found very different results for the star formation histories. Mould (1997) found an initial burst of star formation activity, which concluded no less than 10 Gyr ago. Since then, star formation has either been constant, at a level $\sim 10\%$ that of the initial burst, or was stopped until a second burst approximately 0.1 Gyr ago. Aparicio et al (1997), on the other hand, found a much less dramatic initial burst. With their favored distance modulus of 24.43, they found that star formation rates were constant since the creation of the galaxy, decreasing by a factor of 3 only in the past Gyr. With the larger distance, a smooth exponentially decreasing star formation rate was favored. Aparicio et al (1997) were also able to constrain the current metallicity to [Fe/H] between -1.0 and -1.45. With no HII regions in the galaxy

(Hodge & Miller 1995), these photometric measurements remain our best estimates of LGS 3's metallicity.

HST presents the opportunity to go beyond the observational limits of ground-based work. With the Mateo (1998) distance modulus of 24.54, photometry down to $M_V = 2 - 3$ is easily obtainable. The most noticeable effect of this is that the horizontal branch will clearly defined, and the photometry and analysis of these data are presented in Chapter 5.

1.3 Dissertation Goals

The primary goal of this dissertation is to present a method that can be used in star formation history analysis study. Although adopting the basic premises of traditional methods, this will make for a more flexible approach to such work. Once this method is described and tested, it will be applied to three data sets: HST VI observations of a region of WLM, ground-based BV observations of two fields in the northern disk of the LMC, and HST VI observations of LGS 3. Each of these galaxies has its own set of questions in its star formation history, regarding star formation rates, ages of the oldest stars, abundances, local star formation history differences, etc, for which this dissertation will attempt to move towards finding answers. Specific goals for the study of each galaxy are given in the introductions of each of the chapters.

Chapter 2

PROPOSED METHOD FOR RECONSTRUCTING STAR FORMATION HISTORIES

2.1 Introduction

The study of star formation histories of stellar populations through CMD analysis involves comparing the observed stellar population with synthetic populations created from evolutionary tracks. Even for a system with only a single population of stars (for example, Flower 1976), such as a star cluster or association, this is not a trivial task. In addition to the obvious free parameter of age, the distance, extinction, IMF, and metallicity of the stars are parameters that generally have large uncertainties. For old stars, where isochrones are very close, it can be nearly impossible to disentangle the effects of these parameters. The analysis of a composite population, with stars of a range of ages and metallicities, and possibly a range of extinctions, is an even more difficult problem, and only recently has been attempted.

The simplest approach to this problem is to create a large number of CMDs based on evolutionary models, which cover the range of "likely" star formation histories. The CMD that most closely resembles the observed CMD is then taken as the best fit, and its star formation history is assumed to be the best of the possibilities. One can also estimate the uncertainty in the answer by looking at other CMDs that closely fit the data, and comparing their star formation histories with the best-fit results. This is largely what has been done in the past (Gallart et al 1996, Greggio et al 1993, Tolstoy 1996, Tosi et al 1991), and is also the basis for the method presented here.

Two large steps must comprise such a method. First is the generation of the synthetic CMDs to be compared with the observations. In order to make a full search of parameter space (star formation rates, IMF, distance, extinction, and metallicity enrichment) in under a week, a solution for each combination of distance, extinction, and metallicity enrichment must be made in a scale of minutes. This is not possible under previously developed methods, so a new technique of generating any number of models with the same parameters other than star formation rates had to be developed. This was done by dividing the lifetime of the star formation into many time segments, each of which having its CMD calculated separately. Any composite star formation history is thus a linear combination of these partial CMDs, meaning that the computer time required for the CMD generation is only that needed to go through the star formation history once, greatly reducing the time spent on computations.

The second half is determining what will be used to determine how similar a model CMD is to the observed CMD. Although many factors are taken into consideration when one compares two CMDs with a third by eye, only one of the two can be the better fit. Thus despite some claims to the contrary (Tosi et al 1991), it is appropriate to develop a single goodness of fit parameter for the comparison of CMDs. If this parameter can be defined quantitatively, it will allow for a numerical solution of the star formation history. Such a quantitative fit parameter will also have the advantage of being able to use CMDs with more than two axes, something that would be impossible if fitting by eye. The tests involving synthetic photometry use three-dimensional CMDs (axes B, $B-V$, and $V-I$), which will contain more information than a standard two-dimensional CMD (B vs. $B-V$ for example) and be less sensitive to photometric errors. As the fit parameter is to compress all of the information contained in two CMDs into a single number, it is important to choose it well. A final incentive to find a single goodness of fit value is that the fit can be made according to statistics rather than subjective judgment.

By using both of these modifications to standard star formation history methods, it is possible to determine the star formation history for a single set of distance, extinction, IMF, and enrichment history parameters very quickly, thus satisfying the need for a fast and accurate method.

This chapter details this proposed new method for star formation history reconstruction, and runs a thorough battery of tests on it. The first tests will show the sensitivity of the chosen fit parameter to variations in the input parameters, the second will test how well this method can reconstruct a synthetic composite population, and the final will apply it to an observed globular cluster.

2.2 Method Description

2.2.1 Data Storage

In order to make an accurate comparison of observed and synthetic photometry, a uniform data storage system must be applied to each. In order to maximize the detail in the diagram while giving good statistics, the CMDs are divided into bins in both dimensions, the size of the bins determined by the detail level in the CMDs. The value of each bin, then, is the number of observed stars that falls in the bin (in the case of the observed data) or the number of stars expected to fall within the bin (in the case of the synthetic data). For example, if one wishes to make fits based on a structure that is 0.05 magnitudes across in $B-V$, the bin size should be 0.05 magnitudes in color. The solutions in the following chapters used bin sizes of 0.05 and 0.1 magnitudes in color and between 0.15 and 0.3 in magnitude. The higher resolution gives better sensitivity for smaller features, while the lower resolution gives better sensitivity for larger features. The solutions given in the following chapters use both resolutions, the average of the two giving the final results.

These binned CMDs are then smoothed as necessary to minimize the random noise due to the small number of stars in each bin. The smoothing here was done with a Gaussian kernel, of $\sigma = 1$ bin. With the small bins and smoothing, one is able to achieve reasonable statistics, while preventing features such as main sequence shapes from getting destroyed by large binning. This avoids problems caused by the positioning of the grid on the CMD, as the sharp edges of the bins get smoothed out.

A significant improvement over previous methods made here is the ability to use more than two axes for the color-magnitude grids. The method can be used with any number of axes, but the tests below with synthetic data will all be done with three-color photometry. Using the smoothing, it will not be necessary to increase the bin sizes with larger numbers of axes in order to keep sufficient stars per bin to fit accurately. The limits to the number of axes used are (1) the requirement that all stars have photometry in every color (thus $UBVI$ would be a poor choice for an old population), (2) the CPU and memory consumption, and (3) the availability of data. This third limit will be significant, as most available data is in the form of two-band photometry.

2.2.2 Input Data

The first piece of information needed is, of course, the photometry of the stars to be studied. Since the stars are to be placed on a single color-magnitude grid, it is essential to have photometry in every color for a star in order to use it. Photometric uncertainties are not needed; rather, artificial star data are used to degrade the synthetic CMDs to the quality of the observed data. Other photometric errors such as zero point problems can be dealt with in the determinations of star formation histories, as will be shown below.

In addition to photometry of stars and results of artificial star additions, the following information is needed to run the program: distance, extinction, metallicity, and initial mass function (IMF). Additionally, internal extinction, metallicity, and IMF can be allowed to vary with time. In practice, not all of these quantities are known to sufficient accuracy. Therefore it will often be necessary to run the program multiple times with different combinations of input parameters.

2.2.3 Artificial Stars

The artificial star library provides the link between the theoretical models and the observed data; it is used to degrade the sharp isochrones to the quality of the observations so that a valid comparison can be made. What is necessary, then, is a library of artificial star results that can provide not only the completeness as a function of magnitude and color, but also the distribution of recovered magnitudes.

In order to ensure that the primary source of error is the observations rather than the artificial stars, it will be important to have many more artificial stars than observed stars at each point on the CMD. In all work shown here, the density of artificial stars on the CMD was between 5 and 16 times the density of observed stars on the CMD. Because the noise is proportional to the square-root of the number of stars, this ensures that the uncertainty created by the artificial stars is roughly one-third that created by the observed stars. In addition to signal-to-noise issues, it is crucial that the artificial star tests go faint enough that they reach the point that the completeness is truly zero. This will generate an accurate photometry cutoff, as the number of stars just below the cutoff is higher than the number of stars above it.

Finally is the issue of the distribution of the artificial stars. Distributing the artificial stars according to the distribution of observed stars is tempting, but ignores the fact that the completeness can vary widely over an image. (For an example of this, see the WLM globular cluster section later in this chapter.) Thus the light distribution (after sky subtraction) is a better estimate of the stellar content of a field, as stars need not be resolved to be counted. In cases in which the field is likely to be broken up and analyzed separately, care should be taken that a representative sample of magnitudes and colors (as discussed above) is present in each section.

2.2.4 Model Data

The final ingredient required for the program is a routine that can calculate an isochrone given any age and any of the metallicities input. For the tests using synthetic data below, the Schaller et al (1992) evolutionary models are being used, due to the availability of interpolation routines for those models. These models lack the horizontal branch, red clump, and AGB phase, which is an obvious shortcoming. But they will suffice for this testing of the method, as the "stars" being studied are created from the same models used for their analysis.

All studies of observed data in this paper use interpolated Padova isochrones (Girardi et al 1996, Fagotto et al 1994), for which interpolation routines were not provided and had to be written. These models also have their shortcomings. Most notably is the lack of a blue horizontal branch, and the incorrect position of the AGB tail. Smaller issues are that the red clump is frequently too spread-out and that blue loops are always uncertain.

The horizontal branch issue only really affects Chapter 5, as neither the WLM or LMC fields showed a noticeable horizontal branch. (The WLM globular does have one, but the problem was avoided there by ignoring that part of the CMD.) In LGS 3, the red HB was well-reconstructed by the models, but the blue HB stars, as one might expect, gave the appearance of main sequence stars and affected the fit.

The other issues affect the aesthetic value of the reconstructed CMDs more than the affect the quality of the fits. Chapter 3 shows that the diffuse red clump will be used to fit the data if necessary, thus providing a reconstructed CMD with a red clump that is too broad, but an accurate SFH analysis nevertheless. In these data sets, the AGB and blue loop phases are populated thinly enough that errors in the models contribute very little to the overall fits.

The various input parameters are then used to create a set of theoretical color-magnitude grids. Each grid is specified by an initial and final time, IMF, and metallicity, as well as the global properties extinction and distance for all grids. Between the initial and final time for a given grid, star formation is assumed to be constant. One $M_{\odot}$/yr is used so that the coefficients of the solution will be in terms of $M_{\odot}$/yr of star formation.

A number of isochrones between the initial and final time are then calculated, with the number being sufficiently large that the largest distance between adjacent isochrones is smaller than the bin size used in the grid. Each isochrone is then stepped along, again with the step size much smaller than the bin size of the color-magnitude grid. At each point along the isochrone, all artificial star results of the appropriate magnitude and color are used to determine not only the probability of detection of a star at that point, but also the distribution of recovered colors and magnitudes. This data is then used to increment the color-magnitude grid at every bin in which the star could be recovered.

The final result of this is a set of color-magnitude grids covering all necessary times, each of which contains what the observed stars should look like if star formation proceeded between the initial and final times of the grid at a constant rate, and there was no star formation at any other time.

An uncertainty grid should be calculated for each color-magnitude grid. Without smoothing, each bin of an uncertainty grid is simply equal to the square-root of the value of the same bin in the color-magnitude grid. With smoothing, however, standard rules of error propagation will need to be used.

2.2.5 Fitting

The procedure outlined above should produce a set of synthetic color-magnitude grids containing the positions where stars would be expected to fall given the input parameters (age range, metallicity, etc) for each grid. The final task of the SFH determination will then be to determine the best linear combination of the theoretical grids to match the observed data. Each bin of the combined theoretical color-magnitude grid is given by

$$\sum_j c_j M_{i,j}, \tag{2.1}$$

where c_j is the linear coefficient for model j (which is the SFR), and $M_{i,j}$ is the number of stars in the ith bin of the jth model, assuming 1 $M_{\odot}$/yr of star formation.

As mentioned above, a single goodness-of-fit parameter is required to solve for the star formation history. Since these data are synthetic and include no cosmic rays, PSF-fitting errors, binary stars, or other sources of "unfittable" contamination, a χ^2 is the correct choice. A more sophisticated parameter may be needed in cases where the data might have large wings in the scatter caused by the sources mentioned above. The goodness-of-fit parameter χ^2 is given by

$$\chi^2 = \sum_i \frac{(O_i - \sum_j c_j M_{i,j})^2}{\sum_j c_j \sigma_{i,j}^2}, \tag{2.2}$$

where O_i is the ith bin of the observed grid and $\sigma_{i,j}$ is the ith bin of the uncertainty grid for model j.

2.2.6 Determining Uncertainties

Finally, it is important to check the answer to evaluate the uncertainties of the star formation rates and to test the uniqueness of the solution. The easiest way of doing this is to create artificial stars from the determined star formation history, and re-run these stars through the analysis. The variations in the coefficients of the fit in this Monte Carlo simulation will determine the uncertainties.

The program used here to create the artificial stars is of course not the same one used for the fitting. A more traditional population synthesis approach is taken here. For each time bin, a pool of mass equal to the total star formation of the bin is created, and stars are formed from the pool with mass distributions given by the assumed IMF and ages given by the initial and final times of the theoretical grid.

It will also be necessary to determine uncertainties due to assumptions of the metallicity enrichment, IMF, extinction, and distance used. To calculate these, it will be necessary to run a set of solutions using various combinations of these parameters. The range of parameters returning reasonably fit CMDs is treated as the uncertainty in the parameters, while the standard deviation of determined star formation rate coefficients is added in quadrature to the uncertainties determined from the Monte Carlo run, for a true uncertainty in star formation rates.

Naturally, distance, metallicity, extinction, and age errors are highly related. Although not true, it is often claimed that distance, metallicity, and age are degenerate, in the sense that the same CMD (for old ages) can be produced through multiple combinations of the three parameters. Nevertheless, the four parameters do have highly correlated errors, and the Monte Carlo tests will provide an estimate of the total uncertainty of every parameter (including uncertainties from correlations with other uncertain parameters).

2.2.7 Contamination

Inevitably the stars studied will also be contaminated by foreground or background stars. Rather than attempting to subtract stars from the data set to eliminate contamination, it is better in this case to make a color-magnitude grid of the field stars, in exactly the same way the grid of the sample is made, which can then be included into the fit. The coefficient for this grid will normally be set to one, in the case of taking an image of the object to be studied and a second image of a nearby field. For this, χ_i^2 is given by

$$\chi_i^2 = \frac{(O_i - C_i - \sum_j c_j M_{i,j})^2}{\sum_j c_j \sigma_{i,j}^2 + \sigma_{Ci}^2}, \tag{2.3}$$

where C_i is the color-magnitude grid of the contaminating stars. Alternately, a theoretical foreground star data set could be used, with the absolute number of contaminating stars left to be fit. χ_i^2 for this is given by

$$\chi_i^2 = \frac{(O_i - c_c C_i - \sum_j c_j M_{i,j})^2}{\sum_j c_j \sigma_{i,j}^2 + c_c \sigma_{Ci}^2}, \tag{2.4}$$

where c_c is the coefficient for the contaminating stars.

2.2.8 Uncertainties in Models

Due to the uncertainties in stellar evolutionary models, a method that relies upon the models to determine star formation histories must be able to account for the uncertainties as well as possible. There are two straightforward ways in which this can be done in the context of this SFH determination method.

The first is that the bins in the color-magnitude grid that correspond to the less certain phases of evolution can be given less weight in the goodness of fit parameter, meaning that this f(χ_i^2) would instead be f(χ_i^2,i). This is useful when the existence of a phase is uncertain (for example blue loops, where the question whether or not some stars have a blue loop at all is determined by the input physics the model uses). An extreme case of this can be used if the available models are incomplete, such as the ones used to compute the models in this section. In that case, one could give no weight to regions of the grid where the missing phases would be.

The second is that the smoothing of the grid can be larger in areas that are more uncertain. This will be more useful when it is well known that a phase happens, but the position of a star on the CMD is uncertain. An example here will be supergiants, where different models will all have a supergiant phase, but may predict different colors and magnitudes.

In the end, however, the quality of the solution will be no better than the quality of the models. Ideally, one would make solutions with different sets of theoretical models and thus different choices of calibrations, post-RGB evolutionary models, and assumptions of physical processes (especially rotation and convection). Although this might be possible if one were building his own models, in this work only one set of models will be used for each data set. The synthetic data used for tests in this chapter use the Schaller et al (1992) models, while all work involving real observations are uses interpolated Padova isochrones (Girardi et al 1996, Fagotto et al 1994).

2.3 *Initial Tests*

The first tests to be run are made in order to determine the sensitivity of the fit parameter to various changes in the input parameters, and to make sure the best fit is indeed the one with the correct input parameters. Determination of what errors would be caused by incorrect measurements of the input parameters is also important, and is done below.

First, a model galaxy must be created, with some set of input parameters. The ones used here are as follows:

- power law IMF, $\phi(m)dm = m^{-1.5}$
- Mass range 0.8 $M_{\odot}$ to 120.0 $M_{\odot}$
- Star formation constant at 1.5×10^{-5} $M_{\odot}$/yr from 0 to 15 Gyr
- Extinction=0.0
- Distance modulus=0.0
- Limiting magnitudes $B = 5$, $V = 5$, $I = 4$

This will create a set of roughly 13000 to 14000 stars, which is a reasonable number for the study of dwarf galaxies. Photometric errors are Gaussian with 1 σ values varying from roughly 0.14 magnitudes at the magnitude cutoffs to about 0.03 for the bright stars.

Table 2.1: Derived Star Formation Rates, varying IMF slope

Age (Gyr)/IMF slope	-1.05	-1.20	-1.35	-1.50	-1.65	-1.80	-1.95
0−1	0.82	0.88	0.94	1.00	1.06	1.12	1.18
1−2	0.99	0.99	1.00	1.00	1.00	1.01	1.01
2−5	1.07	1.05	1.03	1.00	0.99	0.96	0.94
5−10	1.17	1.11	1.05	1.00	0.94	0.89	0.85
10−15	0.94	0.97	0.98	1.00	1.01	1.02	1.03

Note that the distance modulus is zero, so that the terms absolute and apparent magnitude can be used interchangeably.

The star formation history solving program is then run, with identical input parameters to those listed above, except that one parameter is allowed to vary. For the solutions, the star formation rates were solved for at five different time intervals: 0-1 Gyr, 1-2 Gyr, 2-5 Gyr, 5-10 Gyr, and 10-15 Gyr.

2.3.1 IMF slope

Table 2.1 shows the dependence of determined star formation rate upon the chosen IMF slope. Values in the table are normalized to 1.00 for IMF slope of -1.50 for the sake of ease of comparison. The IMF slope giving the best fit was -1.45±0.16. The most obvious trend is that there is more recent star formation needed with a steeper IMF slope, which is expected as the 0-1 Gyr stars are the ones that make up the majority of the visible main sequence. Trends in the other time bins are primarily in reaction to the trend in the youngest bin.

Given an uncertainty in the IMF slope of roughly 0.15, the uncertainty in the star formation rates should be increased by roughly 5% with 14000 stars and time bins of these sizes. An uncertainty of 0.30 in the IMF slope will result in an increased uncertainty of approximately 10% in the star formation rate under these circumstances.

Table 2.2: Derived Star Formation Rates, varying log(Z)

Age (Gyr)/log(Z)	−0.09	−0.06	−0.03	0.00	0.03	0.06	0.09
0−1	0.87	0.91	0.96	1.00	1.04	1.09	1.13
1−2	0.89	0.93	0.96	1.00	1.05	1.09	1.14
2−5	0.97	0.99	1.00	1.00	1.01	1.00	1.00
5−10	0.88	0.92	0.96	1.00	1.04	1.08	1.12
10−15	1.74	1.49	1.24	1.00	0.76	0.52	0.30

This is an important result, as in most situations (such as the data sets in this paper) the data are not of sufficient quality to discern between different IMF slopes.

2.3.2 Metallicity

Table 2.2 shows the dependence of determined star formation rate upon the chosen metallicity. Values in the table are normalized to 1.00 for solar abundance for the sake of ease of comparison. The metallicity giving the best fit was log(Z)=0.003±0.002. The primary noteworthy effect is that the past star formation rates given for very old stars change strongly with metallicity, while the past star formation rates for other ages are affected very little, relative to each other. The primary reason for this is that metal poor stars have bluer and more luminous isochrones, so that estimating too low a metal abundance will create brighter, bluer stars from the models, causing the stars to look older than they really are.

A metallicity error of 0.06 will have little effect on the determined star formation rates for anything but the oldest stars, which can have errors increased by roughly 50%. Clearly this is a major effect for the oldest stars, but the solution's high sensitivity to metallicity should help to constrain the value.

Table 2.3: Derived Star Formation Rates, varying distance

Age (Gyr)/$(m-M)$	-0.06	-0.04	-0.02	0.00	0.02	0.04	0.06
0−1	1.00	1.00	1.00	1.00	1.00	1.00	1.00
1−2	0.90	0.93	0.97	1.00	1.03	1.07	1.10
2−5	1.00	1.00	1.01	1.00	1.00	0.99	0.98
5−10	0.82	0.88	0.93	1.00	1.07	1.16	1.25
10−15	1.16	1.13	1.07	1.00	0.89	0.74	0.57

2.3.3 Distance

Table 2.3 shows the dependence of determined star formation rate upon the chosen distance. Values in the table are normalized to 1.00 for distance modulus of 0 for the sake of ease of comparison. The distance modulus of the best fit is 0.011±0.015. The first thing to note is that the estimated amount of recent star formation is correct, regardless of errors in the distance modulus. This is because, while minor differences in the luminosity of a red giant branch make a large difference, minor differences in the luminosity of a main sequence matter little. For older stars, an error in the distance modulus has a similar effect of shifting the red giant branch as an error in the metallicity.

Because of the sensitivity of the fit parameter to the distance modulus, the large deviations from the correct star formation history created by errors in the adopted distance modulus should account for no more than 10% in this case.

2.3.4 Extinction

Table 2.4 shows the dependence of determined star formation rate upon the chosen extinction. Values in the table are normalized to 1.00 for extinction of 0 for the sake of ease of comparison. The extinction giving the best fit was A_v=0.003±0.006. Similar

Table 2.4: Derived Star Formation Rates, varying A_V

Age (Gyr)/A_V	-0.06	-0.04	-0.02	0.00	0.02	0.04	0.06
0–1	0.95	0.97	0.99	1.00	1.02	1.04	1.06
1–2	0.85	0.90	0.95	1.00	1.07	1.13	1.20
2–5	0.95	0.97	0.99	1.00	1.01	1.01	1.02
5–10	0.80	0.86	0.92	1.00	1.09	1.20	1.28
10–15	1.46	1.36	1.21	1.00	0.71	0.36	0.00

to errors from incorrect metallicity and distance, errors from extinction are most pronounced in that they shift the red giant branch and cause errors in the determined star formation rates at old times. A moderate error in the extinction will have little effect on anything but the oldest stars, which would have an extra 10% of uncertainty from extinction uncertainties in this example.

It is interesting to note that extinction, distance, and metallicity uncertainties have very similar effects on the overall star formation history determination. Therefore, when studying a set of data, it is extremely important to test various values of these variables to determine which are correct.

2.3.5 Star Formation History

Considering only the runs in which the input parameters into the solving program were correct, we can estimate how well the method is able to determine star formation rates. By analyzing the variations between the five different sets of stars created, the scatter in the fits can also be determined.

As is seen in Table 2.5, the star formation rates determined from the program are within uncertainties of the input value, 1.5×10^{-5} $M_{\odot}$/yr. The uncertainties are all under 20%, with all but the oldest stars being under 10%.

Table 2.5: Derived SFR$\times 10^5 M_\odot$/yr, with different runs

Age (Gyr)	Run 1	Run 2	Run 3	Run 4	Run 5	Average
0−1	1.47	1.64	1.56	1.55	1.59	1.56±0.06
1−2	1.70	1.33	1.48	1.53	1.58	1.52±0.14
2−5	1.42	1.53	1.54	1.50	1.48	1.49±0.05
5−10	1.67	1.67	1.40	1.48	1.48	1.54±0.12
10−15	1.05	1.15	1.68	1.49	1.51	1.38±0.26

2.4 Example Analysis

A last test on synthetic data is to create a set of stars resembling a typical dwarf elliptical galaxy, and to attempt to derive its star formation history. The observational limits will be the same as in previous tests. As the stars being created are devised with a different algorithm than the SFH solution, the only property the solution shares with the input stars is the use of the same evolutionary tracks. This means that this will test everything except for problems caused by inaccurate models and foreground contamination.

2.4.1 Input

The input star formation history will be a combination of some low-level star formation plus two one Gyr bursts, in which the SFR was five times the normal rate, as shown in Figure 2.1. There is also a change between higher SFRs in the early epoch of the galaxy, as well as some metal enrichment. The synthetic CMDs produced are shown in Figures 2.2 and 2.3, and appear to be, as expected, old systems with a non-trivial SFH.

The lack of horizontal branch, red clump, and AGB stars is, as mentioned above, the result of the stellar evolutionary models used for this test. (For the purpose of this test, this should suffice, as the same incomplete models are used to create the stars that are also used to analyze the data.) The effect on the estimated errors is uncertain. On one hand, a CMD with two crucial parts (the AGB and horizontal branch or red clump) missing contains significantly less information, and thus the analysis is handicapped by the omission. On the other hand, because these phases are generally modeled poorly by model sets that include them, their omission will reduce possible sources of error, such as blue HB stars that get solved as main sequence stars, seen in Chapter 5. Regardless, these phases make up a relatively small fraction of a galaxy's stellar content, and because the strength of this method is its ability to use all stars, the effect should be small.

The effect is therefore one of some low-level constant star formation rate, with two bursts, during which time the rate was five times the normal rate. From the artificial star creation program, 13839 stars were created to be analyzed. Presumably the ranges of metallicities of the stars can be determined spectroscopically, as can the overall extinction to the galaxy and the lack of internal extinction, as explained in Section 2.4.2.

The following information will be solved for:

- number of bursts
- strengths of the bursts
- ages of the bursts
- metal enrichment history
- age of the youngest and oldest stars
- IMF

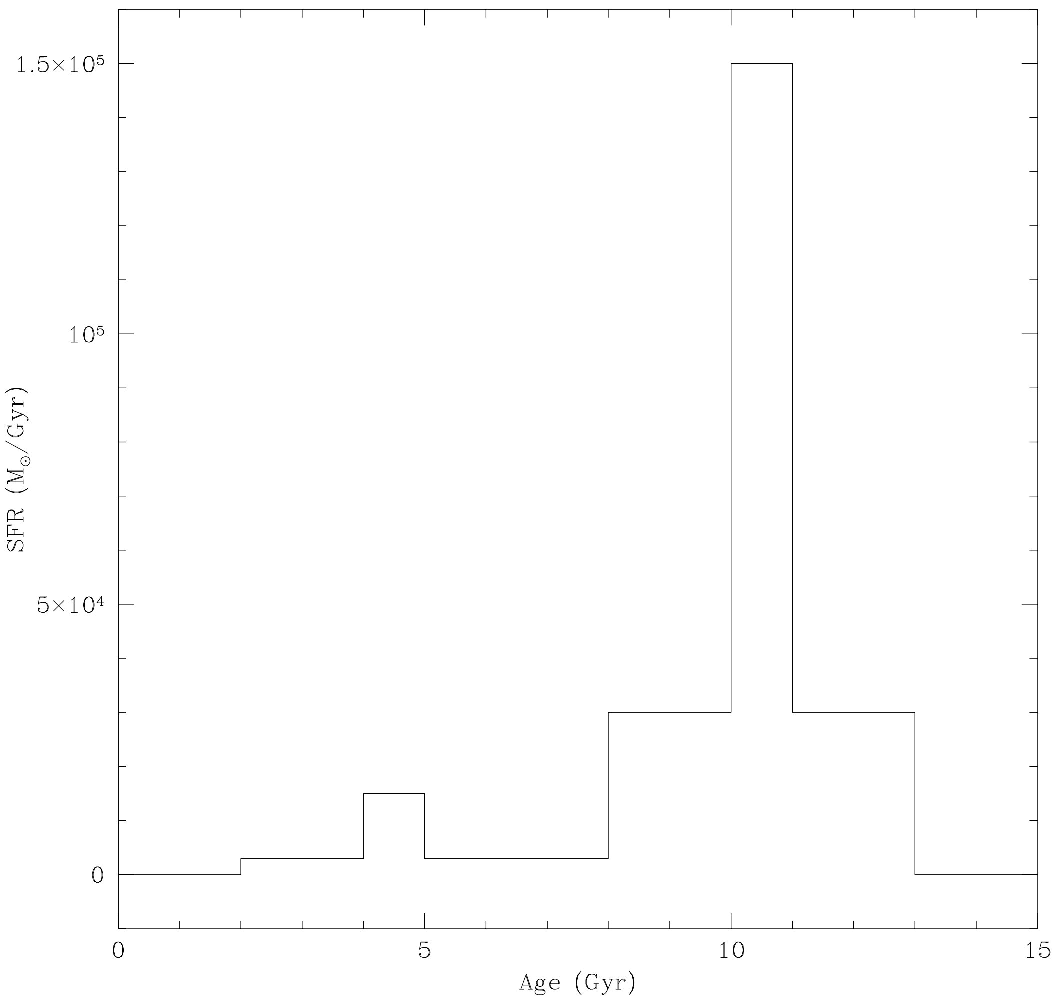

Figure 2.1: Input star formation rates, shown on relative scale. In all star formation history diagrams, old stars are shown with large age.

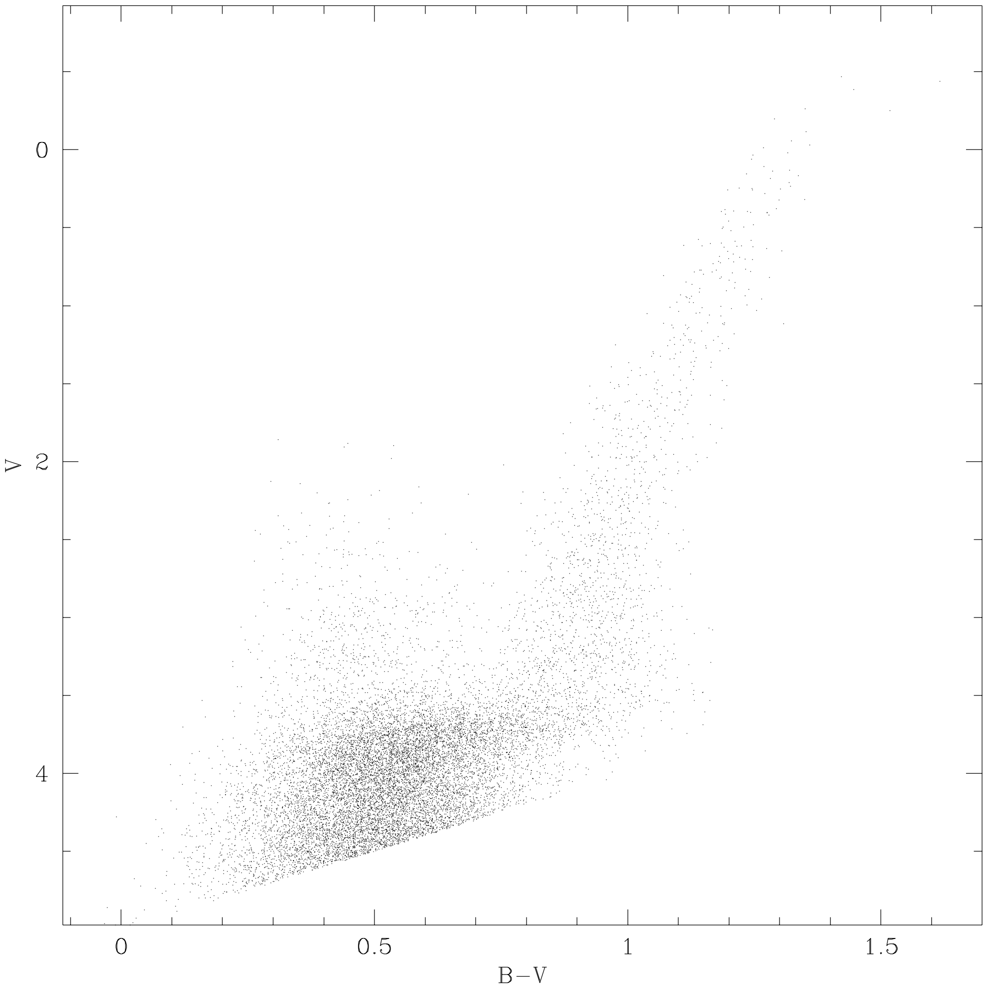

Figure 2.2: $(V,\, B-V)$ synthetic CMD

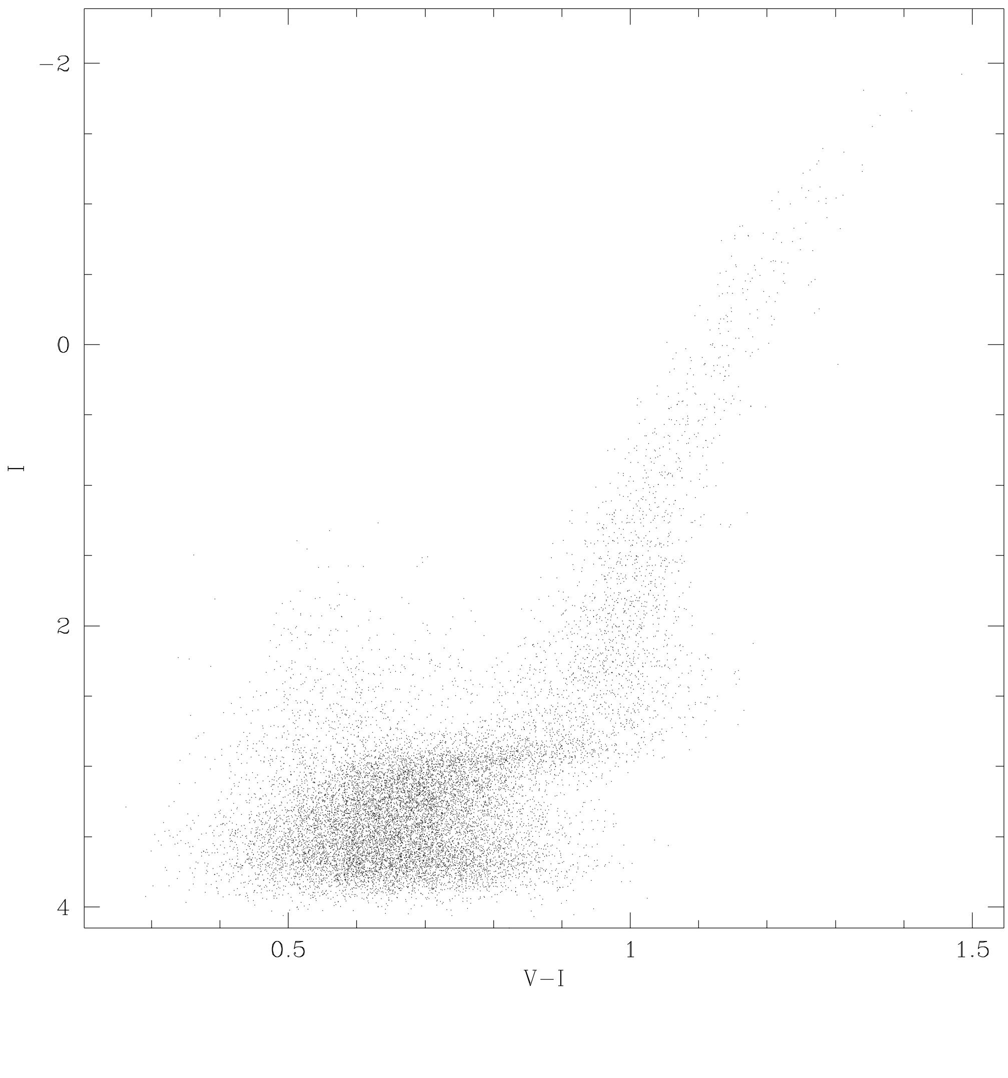

Figure 2.3: $(I, V-I)$ synthetic CMD

The input IMF will be a power law with slope -1.5, lower mass limit $0.8 M_{\odot}$, and upper mass limit $120 M_{\odot}$.

2.4.2 Parameters for Solution

It will be assumed that whatever the IMF, it does not change with time. However, different runs with different IMF values will be made in an attempt to determine the correct value. The upper and lower IMF mass limits are set to the same as the input, but this is actually not important. The given upper mass limit is unimportant, as the most massive star currently shining in this galaxy is roughly 1.5 $M_{\odot}$ as determined by the youngest star formation activity. The lower mass limit is also not something that will cause problems, as stars less massive than $0.8 M_{\odot}$ will never become bright enough to be visible to the simulated telescope.

As there is no recent star formation, then presumably this test galaxy has little in the way of gas or dust to cause internal extinction. Estimates of external extinction, and upper and lower abundances should be determined spectroscopically before making the SFH solution. The specific values of these obviously will also require analysis of the photometry, but can be determined while making the SFH solution, by varying the input values to achieve a better fit to the CMD.

For the case of this data set, it will be known that the range of abundances is -0.7 to -0.4, and that the foreground extinction is close to zero.

Finally, due to the lack of an upper main sequence, one can determine that there are no young stars before running the solution. By determining the youngest isochrone that passes through the data, the age of the youngest stars is seen to be approximately two billion years. Figure 2.4 shows the $(V,\, B-V)$ CMD with 1 Gyr, 2 Gyr, and 3 Gyr isochrones plotted over it. Clearly there has been no star formation as recent as 1 Gyr, but a more precise time of most recent star formation must be solved for.

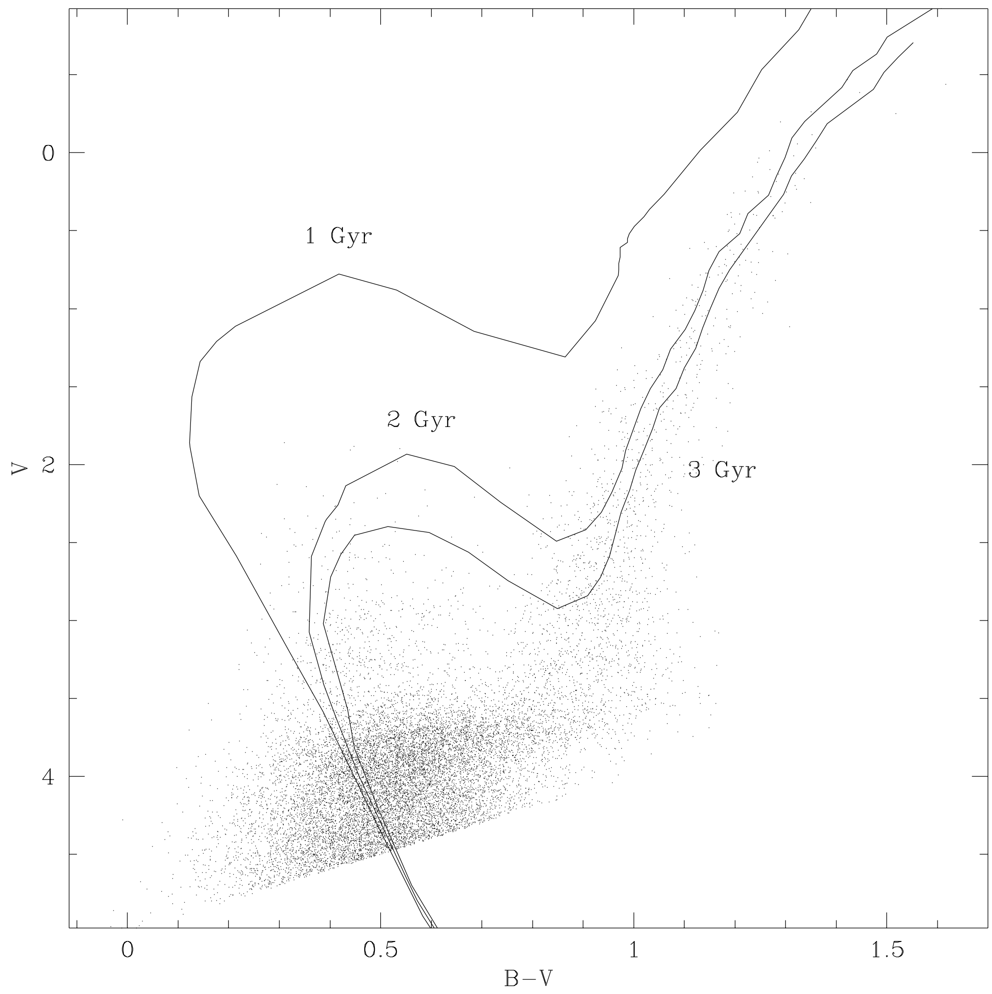

Figure 2.4: (V, $B - V$) synthetic CMD with 1 Gyr, 2 Gyr, and 3 Gyr isochrones

2.4.3 Enrichment and IMF

The process of deducing the star formation history is a process of starting with many free parameters and reducing the number to achieve the best fit with the fewest free parameters. For an initial run through the code, bins one billion years wide were used from 2 to 15 Gyr.

The metallicity at the beginning and end of star formation, as mentioned above, should be known beforehand from spectroscopic observations. But the time when it increased would not be known, so a series of runs were made with different enrichment histories to determine the enrichment history that best fits the data. This correctly gives an enrichment age of 8 Gyr. Likewise, a series of runs with various IMFs was done to determine the best IMF.

When dealing with systems of old stars, such as this simulated galaxy, it is often better to assume an IMF rather than attempting to determine one, because little of the main sequence is seen. On the red giant branch, stars evolve sufficiently rapidly that the numbers of stars at different locations on an isochrone is determined by the lifetime of the particular stage of evolution rather than the IMF. With this in mind, it should not be surprising that nearly identical star formation histories were obtained using vastly different IMF slopes.

2.4.4 Solution

The determined star formation history using the enrichment history and IMF determined in the previous section is shown in Figure 2.5. Comparing this information with what was hoped to be determined, the following results are found:

- The determined number of bursts is two, which is correct.

- The mass formed into stars between 4 and 5 Gyr ago is determined to be $1.3 \times 10^4 M_\odot$, 11% low compared with the correct value of $1.5 \times 10^4 M_\odot$. The second

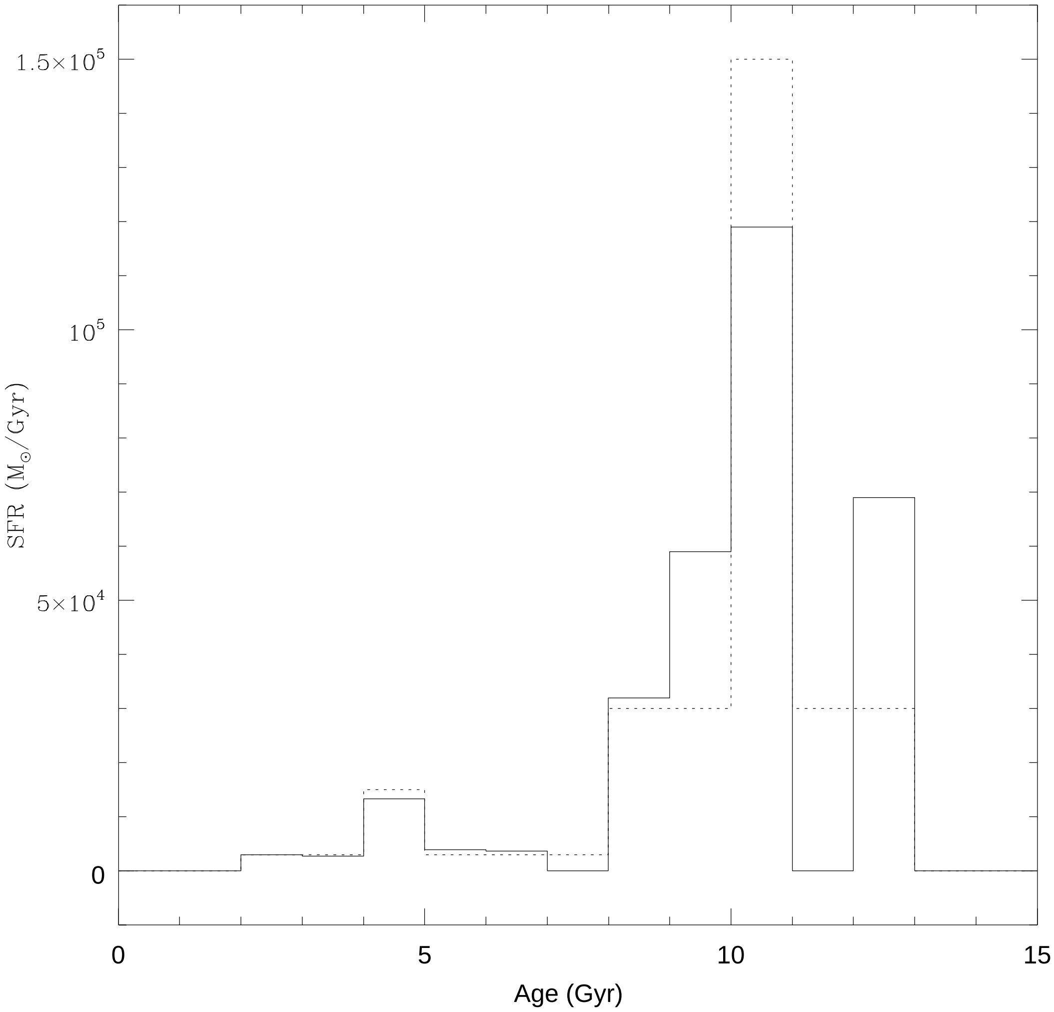

Figure 2.5: Determined star formation history. Dotted line is input star formation rates, solid line is solution.

burst could either be interpreted as $1.2 \times 10^5 M_\odot$ between 10 and 11 Gyr or $1.8 \times 10^5 M_\odot$ between 9 and 11 Gyr. This compares favorably with the input numbers of $1.5 \times 10^5 M_\odot$ between 10 and 11 Gyr and $1.8 \times 10^5 M_\odot$ between 9 and 11 Gyr.

- The ages of the bursts were determined correctly.
- The metal enrichment time and age of the youngest and oldest stars were all correctly determined in the solution process.
- The IMF was unable to be determined as mentioned above in section 4.3.
- Given the uncertainties in the solution, low-level star formation may be seen as clumped in the final solution. An example is the bins from 7 to 8 Gyr and 11 to 12 Gyr, when the input star formation was nonzero but the determined star formation was zero. In the latter case, the 12 to 13 Gyr bin clearly was the recipient of the clumping. This implies that this solution does not have 1 Gyr resolution of uniform star formation rates, although an average star formation rate for the 11-13 Gyr time period does succeed in returning the input value.

2.4.5 Metallicity and Distance

As it is often difficult to easily determine metallicity and distance, and it is often difficult to tell a nearby metal-rich RGB from a more distant metal-poor RGB, an identical solution to the one above was made, but with metallicities of 0.0 current and -0.4 older instead of the input -0.4 current and -0.7 older. Even with changing the distance modulus to the optimal value of -0.30, the goodness of fit parameter showed an extremely poor fit. Thus, if the metallicities are unknown or have high uncertainties, use of this method will be able to pin down the correct values.

Table 2.6: Analysis Results

Value	Input	Output
Enrichment time	8 Gyr	7.9±0.5 Gyr
Young burst age	4.5 Gyr	4.4±0.7 Gyr
Old burst age	10.5 Gyr	10.4±0.4 Gyr
Young burst SFR	$1.5 \times 10^4 M_\odot$	$1.2 \pm 0.4 \times 10^4 M_\odot$
Old burst SFR	$1.5 \times 10^5 M_\odot$	$1.4 \pm 0.2 \times 10^5 M_\odot$
SFR, t<8 Gyr	$3.0 \times 10^4 M_\odot$	$2.6 \pm 0.3 \times 10^4 M_\odot$
SFR, t>8 Gyr	$2.7 \times 10^5 M_\odot$	$2.8 \pm 0.1 \times 10^5 M_\odot$
Youngest star age	2 Gyr	2.0±0.3 Gyr
Oldest star age	13 Gyr	13.5±0.9 Gyr

In addition, if there is a wide spread of metallicities at a given age (which was not the case here), the input grids could use that range of metallicities instead of a single value, as was used here.

2.4.6 Solution Statistics

In order to be certain the successful determination was not a result of good fortune, additional trial runs were made, each completed identically to the one described above, and the results of the runs compared.

Table 2.6 lists the average results of the trial runs, with standard deviations. All values except for overall recent star formation rate were determined to within 1 σ, and the recent star formation rate was off by only 1.3σ. The larger scatter in the results regarding the younger stars is due to the fact that the input star formation rates were ten times higher at early times.

2.5 *Final Test: The WLM Globular Cluster*

In addition to testing how well a synthetic population of known star formation history can be disentangled, it is important to test how well the history an observed simple population, such as that of a globular cluster, can be determined. WLM is a Local Group dwarf, whose global star formation history will be examined in detail in Chapter 3. It contains just one globular cluster, which is very luminous with a V magnitude of roughly 16.1 (Sandage & Carlson 1985). Lee et al (1993) recalibrated the Cepheid distance modulus to 24.87 $\pm$ 0.08, thus giving the cluster an absolute magnitude of M_V = -8.8.

2.5.1 Observations

Four images of the WLM globular cluster were taken as part of a Cycle 6 HST GO program. Two exposures were taken with the F555W filter of exposure times 2600 and 2700 seconds; two were taken with the F814W filter for 2700 seconds each. The PC was centered on the globular cluster to minimize crowding and PSF undersampling.

2.5.2 Reductions

With two images of equal time per filter, cosmic rays were cleaned with an algorithm nearly identical to that used by the IRAF task CRREJ. The two images were compared at each pixel, with the higher value thrown out if it exceeded 2.5 sigma above the average of the two. The cleaned, combined F555W image is shown in Figure 2.6.

Photometry was then carried out using the HSTPhot package described in Appendix A. For the CMD and luminosity function analyses below, roughly the central 20% of the PC image was analyzed so that background contamination would be minimized. The CMD from this method, showing all stars observed, is shown in Figure 2.7a, with the same data reduced with DAOPHOT shown in Figure 2.7b. Error bars are shown corresponding to the artificial star results, rather than the standard errors

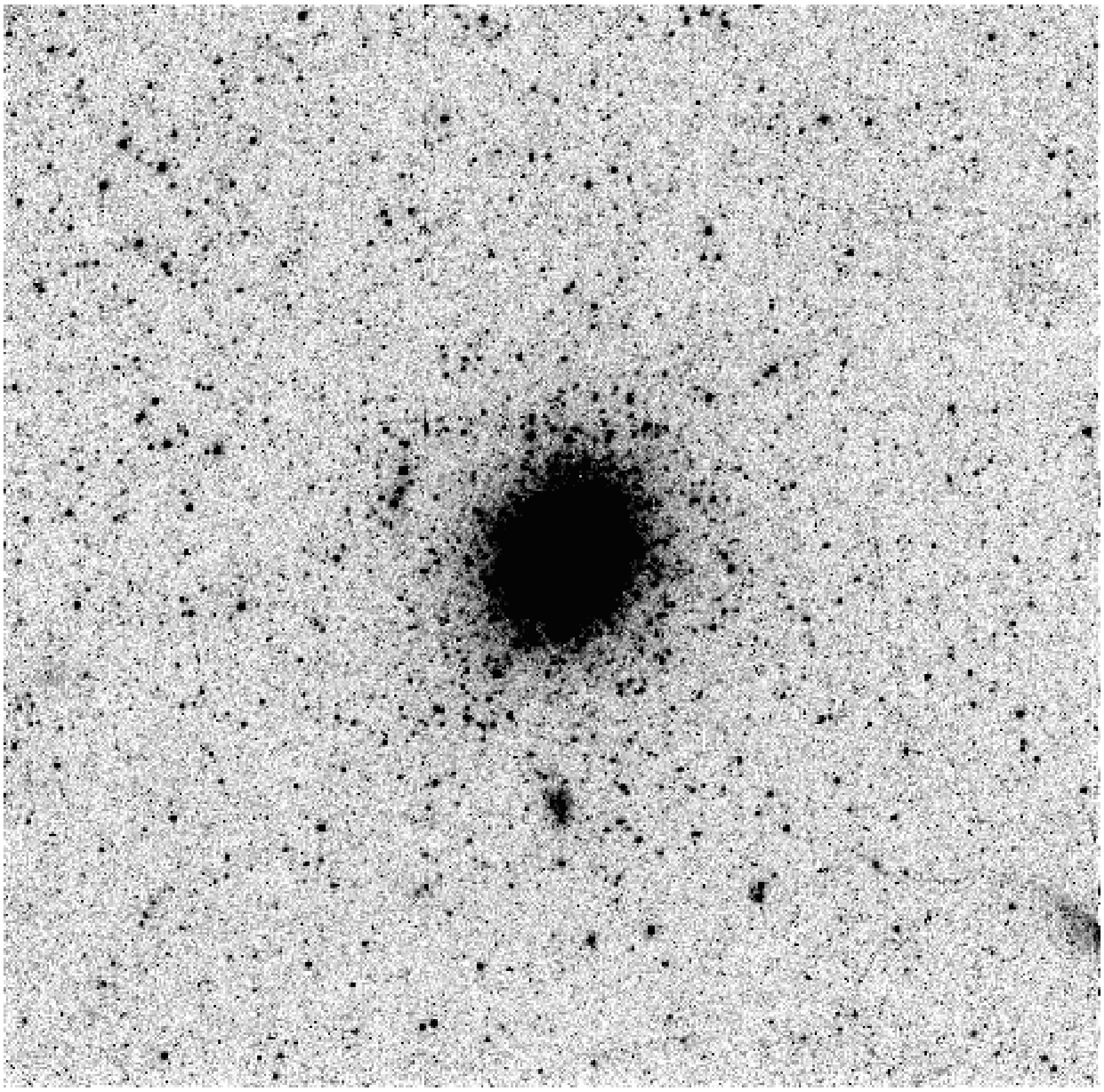

Figure 2.6: Combined V image after cosmic ray cleaning.

from the PSF fits and transformations.

The improvement over traditional PSF fitting algorithms is remarkable, as the features in the CMD are sharper and, more importantly, the areas away from the populated regions are far cleaner. In the CMD analysis below, an additional constraint was made, removing any stars that were fit worse than 2σ from consideration, and thus producing an even cleaner CMD.

Artificial star tests were also made with the HSTPhot package, in order to build up a large library of completeness data and artificial star results for use in generating synthetic data for the CMD analysis.

2.5.3 Luminosity Function

The luminosity functions (LFs) of the globular cluster in V and I are shown in Figure 2.8a and 2.8b, respectively, along with theoretical values taken from interpolated Padova isochrones (Girardi et al 1996, Fagotto et al 1994).

The observed and theoretical LFs are in excellent agreement. The bump in the observed V LF between magnitudes 25 and 26, and the bump in the observed I LF starting at magnitude 24.5 are due to the horizontal branch stars, which cannot be separated from the rest of the CMD cleanly. The only other significant deviation, the bump in the V LF between magnitudes 22.5 and 23, is the clump of stars at the tip of the RGB also observed in the CMD. This seems to be a statistical fluke, a result of the relatively small number of stars in that part of the RGB, and is similar to statistical flukes seen in Monte Carlo simulations. Ignoring the bins contaminated by the horizontal branch, the two fits combine for a χ^2 value of 1.3.

2.5.4 Color-Magnitude Diagram

For the CMD analysis, a cleaner CMD was achieved by throwing out all stars with PSF fits worse than a χ^2 value of 4.0. The observed V, $V-I$ CMD is shown in Figure 2.9a, and was analyzed as described above, with the Padova isochrones again

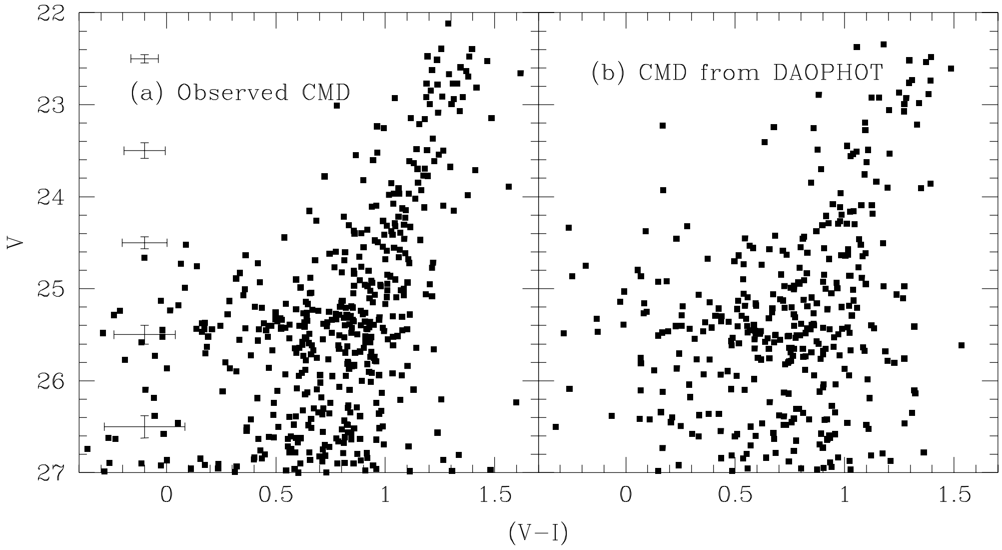

Figure 2.7: The V, $V - I$ color-magnitude diagram is shown in Figure (a). Figure (b) shows the same data, reduced with the IRAF task DAOPHOT.

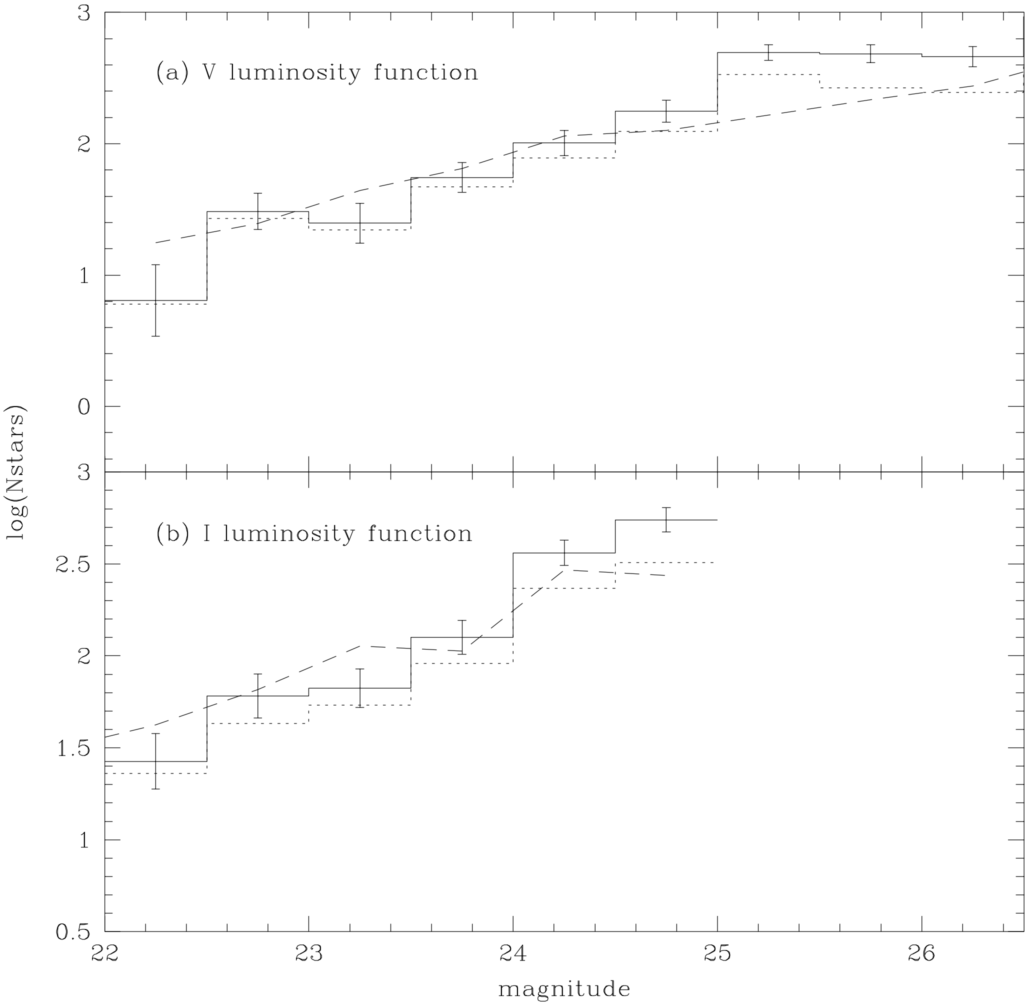

Figure 2.8: Luminosity functions in V and I. The dotted lines show the luminosity function before making completeness corrections; the solid lines and error bars are for the completed luminosity functions. The dashed lines show the theoretical luminosity function, with horizontal branch stars omitted.

used (Girardi et al 1996, Fagotto et al 1994). No assumptions were made regarding the star formation history, metallicity, distance, or extinction to the cluster, and a fit was attempted with all of these parameters free. The χ^2 CMD fit produced the more strongly-defined results, so its values were used.

As expected and hoped, the generic solution for the cluster's star formation history gave one that had a single sharp peak in star formation activity, with a low background star formation level. This background is the result of three causes. First, as the cluster is part of the WLM galaxy, there were some WLM field stars within the area studied, which contributed slightly to the total star count. Secondly, as is apparent from a comparison of the observed and modeled CMDs, the model horizontal branches do not extend as far to the blue, which will cause the fitting procedure to compensate with main sequence stars. (Of course, this is mitigated by the lack of supergiant and AGB stars that would be present if an intermediate-age or young population were present.) Finally, the effect of uncertainties must be taken into account, as a single population will always appear to be spread out. This was seen in the composite population test above, and is seen here as well.

Building on the result that the globular cluster appears to be a single population, the method was then altered to return fits from only a single population of stars. To account for the models' inability to reproduce the blue horizontal branch stars, the fitting procedure was made to ignore that region of the CMD. Model uncertainties for blue loops or AGB stars are unimportant here, as those phases do not appear in the globular cluster population.

Values and uncertainties of the cluster's parameters are calculated by taking the average and standard deviations of the parameters from all fits with a χ^2 within one of the best fit. Because all good fits were used, the fitting errors and uncertainties resulting from an age-metallicity-distance "degeneracy" are accounted for. The following parameters were obtained:

- Age: 14.8 $\pm$ 0.7 Gyr
- [Fe/H]: -1.51 $\pm$ 0.09
- Distance modulus: 24.72 $\pm$ 0.09
- Extinction: $A_V = 0.07 \pm 0.06$

A more conventional distance measurement using the horizontal branch relation M_V (RR) = 0.20[Fe/H] + 0.98 (Chaboyer et al 1996) yields a distance modulus of 24.62 $\pm$ 0.14, which is within uncertainties of the values measured here. The extinction measurement is consistent with a value of 0.08 $\pm$ 0.03 estimated from the Schlegel et al (1998) maps.

A synthetic CMD constructed from these parameters is shown in Figure 2.9b, using the artificial star data to mimic photometric errors, completeness, and blending in the data. The poorly reproduced blue horizontal branch is a result of the isochrones used, but the giant branch was reproduced well, with the proper shape and position.

2.5.5 Correlations of the Parameters

Tables 2.7 through 2.12 show variations of χ^2 with variations each possible pair of input parameters. In the rightmost column of each table are shown the value of the varied parameter corresponding the the minimum of a parabolic fit and the range of the parameter producing fits within one χ^2 of the minimum. The same is shown in the bottom row of each table for the vertical axis. For example, the best distance modulus in the top row if Table 2.7 is 24.75 $\pm$ 0.20. This means that the parabolic fit to chi^2 vs. distance modulus had its minimum value at 24.75, and values between 24.55 and 24.95 would be within 1 of the minimum value. A "-" was put if the best fit fell well outside of the sampled range or if the fit did not produce a minimum.

The extinction values were often poorly fit because the region of negative extinction, which is mathematically useful for the fit but not useful physically, was not

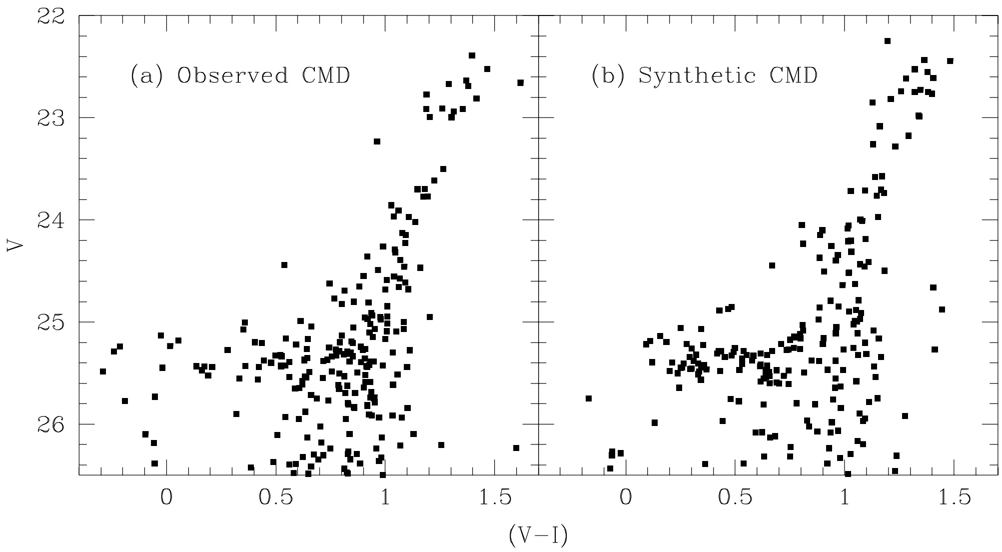

Figure 2.9: The observed V, $V-I$ color-magnitude diagram is shown in Figure (a). Figure (b) shows a synthetic CMD created using the solved star formation parameters. The χ^2 of the fit is 1.4

Table 2.7: χ^2 Values, Varying Distance and Extinction. [Fe/H] of -1.5 and Age of 15.3 Gyr were used. See text for explanation.

A_V / $(m-M)_0$	24.60	24.65	24.70	24.75	24.80	24.85	Best $(m-M)_0$
0.00	2.1	1.9	1.7	2.1	1.4	2.1	24.75 ± 0.20
0.05	1.8	1.8	1.9	1.9	2.1	2.3	24.62 ± 0.23
0.10	2.1	2.0	1.4	2.4	2.4	2.6	24.68 ± 0.14
0.15	2.2	1.8	2.5	2.5	2.6	2.8	24.63 ± 0.17
Best	0.06	-	0.05	0.00	-	-	
A_V	±0.15		±0.11	±0.22			

Table 2.8: χ^2 Values, Varying Distance and Age. [Fe/H] of -1.5 and A_V of 0.1 were used. See text for explanation.

Age(Gyr) / $(m-M)_0$	24.60	24.65	24.70	24.75	24.80	Best $(m-M)_0$
13.3	5.7	5.0	3.5	2.9	3.8	24.75 ± 0.09
13.8	4.1	4.7	2.3	2.3	2.6	24.82 ± 0.15
14.3	3.9	3.2	1.9	2.2	2.4	24.74 ± 0.10
14.8	4.3	3.3	1.8	2.0	2.3	24.74 ± 0.09
15.3	2.1	2.0	1.4	2.4	2.4	24.68 ± 0.14
15.8	2.4	2.1	2.0	2.0	2.7	24.69 ± 0.13
16.3	3.0	2.9	2.9	2.9	3.3	24.68 ± 0.20
Best	16.0	15.6	14.9	14.8	14.8	
Age	±1.6	±1.4	±1.2	±1.7	±1.4	

Table 2.9: χ^2 Values, Varying Distance and Metallicity. Age of 15.3 Gyr and A_V of 0.1 were used. See text for explanation.

[Fe/H] / $(m-M)_0$	24.60	24.65	24.70	24.75	24.80	24.85	Best $(m-M)_0$
-1.7	4.1	3.8	3.0	3.4	2.9	3.5	24.76 $\pm$ 0.14
-1.6	2.2	2.3	1.5	2.2	2.4	2.7	24.69 $\pm$ 0.14
-1.5	2.1	2.0	1.4	2.4	2.4	2.6	24.69 $\pm$ 0.13
-1.4	2.5	2.4	2.4	3.1	3.2	3.3	24.64 $\pm$ 0.16
-1.3	3.2	2.6	3.4	3.8	3.7	3.8	24.60 $\pm$ 0.16
-1.2	4.2	3.8	4.3	4.1	4.0	4.4	24.61 $\pm$ 0.17
Best	-1.47	-1.46	-1.51	-1.52	-1.56	-	
[Fe/H]	$\pm$0.18	$\pm$0.19	$\pm$0.18	$\pm$0.18	$\pm$0.18		

Table 2.10: χ^2 Values, Varying Extinction and Age. [Fe/H] of -1.5 and $(m-M)_0$ of 24.70 were used. See text for explanation.

Age(Gyr) / A_V	0.00	0.05	0.10	0.15	Best A_V
13.3	3.0	4.3	3.5	3.6	-
13.8	2.3	3.0	2.3	2.7	-
14.3	3.0	3.9	1.9	2.2	-
14.8	1.8	2.2	1.8	2.2	-
15.3	1.7	1.9	1.4	2.5	0.05 $\pm$ 0.11
15.8	2.2	2.0	2.0	2.4	0.06 $\pm$ 0.14
16.3	3.2	3.2	2.9	3.1	0.11 $\pm$ 0.24
Best	14.8	15.3	14.9	14.9	
Age	$\pm$1.5	$\pm$1.4	$\pm$1.2	$\pm$1.4	

Table 2.11: χ^2 Values, Varying Extinction and Metallicity. Age of 15.3 Gyr and $(m-M)_0$ of 24.70 were used. See text for explanation.

[Fe/H] / A_V	0.00	0.05	0.10	0.15	Best A_V
-1.7	4.2	4.0	3.0	2.7	0.15 ± 0.08
-1.6	2.5	2.3	1.5	2.2	0.09 ± 0.10
-1.5	1.7	1.9	1.4	2.5	0.05 ± 0.11
-1.4	2.1	2.1	2.4	3.0	0.03 ± 0.12
-1.3	2.7	2.3	3.4	4.4	0.03 ± 0.09
-1.2	3.4	3.4	4.3	5.0	0.02 ± 0.08
Best	-1.44	-1.44	-1.51	-1.57	
[Fe/H]	±0.18	±0.18	±0.18	±0.19	

Table 2.12: χ^2 Values, Varying Age and Metallicity. A_V of 0.1 and $(m-M)_0$ of 24.70 were used. See text for explanation.

[Fe/H] / Age (Gyr)	13.3	13.8	14.3	14.8	15.3	15.8	16.3	Best Age
-1.7	5.1	5.3	5.3	5.6	3.0	3.1	3.4	-
-1.6	3.5	2.6	2.2	2.3	1.5	1.8	2.8	15.0 ± 1.4
-1.5	3.5	2.3	1.9	1.8	1.4	2.0	2.9	14.9 ± 1.2
-1.4	4.4	3.1	2.5	2.2	2.4	2.8	4.3	14.8 ± 1.0
-1.3	5.4	4.1	3.6	3.4	3.4	3.8	5.0	14.8 ± 1.1
-1.2	7.1	6.1	5.0	4.4	4.3	4.7	5.0	15.2 ± 1.2
Best	-1.52	-1.47	-1.46	-1.44	-1.51	-1.53	-1.59	
[Fe/H]	±0.17	±0.14	±0.14	±0.14	±0.18	±0.20	±0.19	

sampled. Table 2.7 is a good example of this. No fits were possible for distance moduli of 24.80 and 24.85, as the best-fit parabola was actually upside-down, with a maximum value at $A_V > 0.15$. The available best extinctions and the best distances do show a weak correlation, with larger extinction values (not surprisingly) producing smaller distance moduli. This would naturally be expected, as a higher extinctions and distance moduli both increase the magnitudes of the observed stars. Extinction is also very highly correlated with metallicity (Table 2.11), the strongest of the six correlations. This should also be no surprise, as an isochrone of higher metal abundance has a fainter and redder RGB, and thus could be combined with a lower extinction to produce a very similar CMD. Finally, Table 2.10 demonstrates that extinction and age show very little correlation.

The age seems largely uncorrelated with extinction and metallicity (Tables 2.10 and 2.12) over the range of values sampled. Since sampling a wider spread of those parameters would result in χ^2 values that would exceed 2.4 (1 above the best value of 1.4), we can be confident that errors in extinction and metallicity will have little effect on the determined age. The distance (Table 2.8) is a significant factor, however, with a distance of 24.65 or closer increasing the age from the preferred 14.8 Gyr to 15.6 Gyr or older.

As noted above, metallicity is strongly correlated with extinction (Table 2.11) but not with age (Table 2.12, while distance is weakly correlated with both (Tables 2.7 and 2.8). Table 2.9 demonstrates that the two parameters are moderately correlated, which again is understandable since increases in either will cause one to expect fainter observed stars.

Since all correlations between the four parameters are accounted for by the calculation of uncertainties in the previous section, detailed knowledge of the relationships is not essential to the end result. However, being able to reproduce the expected correlations is an important test to give confidence in the fitting procedure and the validity of χ^2 as a fit parameter.

2.5.6 Uncertainties in CMD Analysis

The question of what exactly the uncertainties quoted above mean needs some serious attention. The uncertainties from the CMD analysis quoted above and elsewhere in this thesis are calculated as follows. First, all solutions for the star formation history that have χ^2 greater than that of the best fit plus one are eliminated from consideration. Each value is then averaged for the remaining solutions, with the standard deviation providing the uncertainty. The uncertainty is added in quadrature to half of a resolution element size to produce an initial uncertainty. For example, the best χ^2 for the globular cluster solution in the previous section had a value of 1.40. All fits with a χ^2 less than 2.40 were then kept for the determination of the distance, extinction, age, and metallicity. The average extinction-corrected distance modulus for those fits was 24.716 ± 0.082. Because solutions were only made every 0.05 magnitudes of distance modulus (ie, 24.60, 24.65, 24.70, 24.75, etc), an additional 0.025 magnitude uncertainty must be added to the uncertainty of 0.082, giving an uncertainty of 0.086, or a final value of 24.72 ± 0.09. The other four values were calculated identically.

For systems with composite stellar populations (those analyzed in the following chapters), an additional source of uncertainty in the star formation rates is the near-degeneracy of adjacent theoretical isochrones. This can be estimated by generating artificial stellar populations with the solved star formation history, and running star formation history solutions of those. The near-degeneracy will be apparent through random transferring of stars from one age bin into an adjacent age bin, and thus an average and standard deviation of the determined star formation rates will constrain the uniqueness of the solution. The uncertainty from this test should be added in quadrature to that determined from the best fits of the solutions on the observed data, with the final uncertainty accounting for variations in the input parameters, small-number statistics that may be crucial, and the near-degeneracy of isochrones.

Although this is a significant list of sources of error that have been accounted for, it is important to reiterate the three assumptions that are used to generate the fit. These cannot be quantitatively determined by the star formation history solutions, so the uncertainties quoted here do not account for them. For example the 0.7 Gyr globular cluster age uncertainty above is assuming that the models used, fit parameter, and observational effect simulations are all 100% correct. In this case, the model uncertainties would provide the largest source of uncertainty, with Charlot et al (1996) providing an excellent discussion of the effect of model parameters on globular cluster ages and concluding that age determinations based on theoretical isochrones are probably better than ±35% accurate (<5 Gyr uncertainty in this case).

- The chosen fit parameter (χ^2, for example) will always choose a better fit over a worse fit. Thus the synthetic CMD returning the best fit parameter is the CMD most closely resembling the observed data. A χ^2, for example, is not sensitive to large-scale structure in an image, which is why two resolutions of binning are used here and why the smoothing is used. With those additions, χ^2 should produce a very good fit, but whether it *always* chooses a better fit is not known.

- All observational effects are accounted for. This will never be the case. There will always be some effects of poor PSF fitting, foreground contamination, cosmic rays, bad pixels and columns, CCD image reduction errors, binary stars, and imperfect artificial star tests that affect the data. There are certainly ways to minimize each of the above problems, but accounting for all (either eliminated or reproduced in the synthetic CMD) would be impossible (or nearly so).

- The evolutionary models are correct and complete. As mentioned elsewhere in this dissertation, this is not the case, and there are some very notable parts of the CMD with high uncertainties in the evolutionary models. Unfortunately, the theoretical isochrones are not published with uncertainties, so the user can only estimate what effects might be caused by such uncertainties.

2.5.7 Structure

Mean radial profiles were calculated in bins of 10 pixels (0.45 arcsec) in both the V and I images, and are shown in Figure 2.10. The cutoff magnitudes of 27 in V and 26 in I were chosen to minimize the corrections required due to crowding. Additionally, the central bin (0-10 pixels) was thrown out due to extreme crowding problems, but the remaining bins were fit to King models with a least-squares fit. The best parameters for the King models are based on a distance modulus of 24.72, and are shown by the solid lines in Figure 2.10. For a distance of 24.87 (Lee et al. 1993), the corresponding sizes would be 7% larger.

- core radius: 1.09 $\pm$ .14 arcsec (4.6 $\pm$ .6 pc)
- tidal radius: 31 $\pm$ 15 arcsec (130 $\pm$ 60 pc)
- core density: 59 $\pm$ 8 stars/arcsec^2 (3.2 $\pm$ 0.4 stars/pc^2) V, 44 $\pm$ 6 stars/arcsec^2 (2.4 $\pm$ 0.3 stars/pc^2) I
- background density: 0.77 $\pm$ 0.12 stars/arcsec^2 (0.042 $\pm$ 0.007 stars/pc^2) V, 0.77 $\pm$ 0.12 stars/arcsec^2 (0.042 $\pm$ 0.007 stars/pc^2) I

For comparison, Trager et al. (1993) find that 2/3 of Milky Way clusters have core radii between approximately 5 and 60 pc.

2.5.8 Conclusions

The analysis above shows that the WLM globular cluster is similar to halo globulars in the Galaxy. Its luminosity, age, and metallicity all fall within the range of those values seen in the Galaxy, while its distance is within uncertainties of the value obtained from Cepheids and the RGB tip (Lee et al. 1993). Its mean radial profile fits a King (1962)

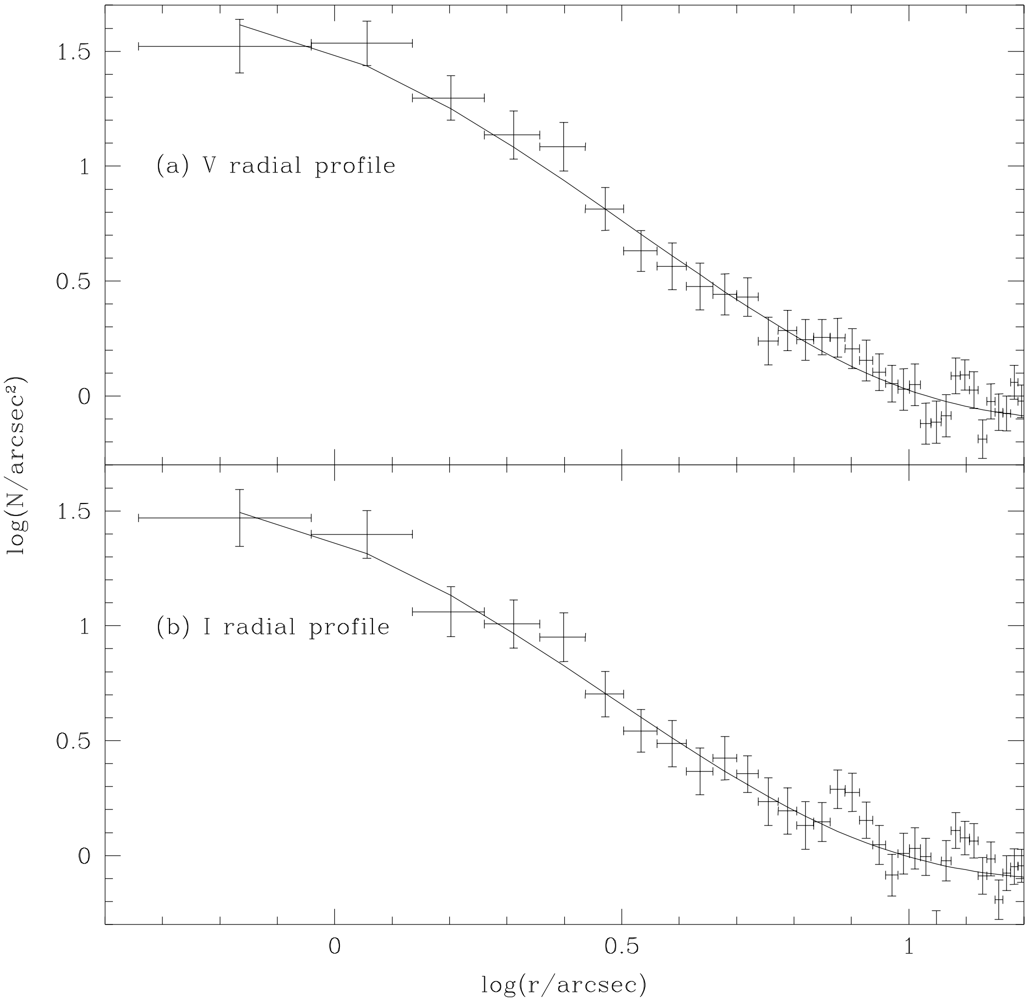

Figure 2.10: Radial profile in (a) V for stars brighter than $V = 27$ and (b) I for stars brighter than $I = 26$, with King models with r_c=1.14 arcsec and r_t=25 arcsec.

model to within the observational uncertainties. The core radius is similar to that observed in massive galactic globulars, while the tidal radius is large by comparison (although very uncertain).

More pertinent to the overall topic of this thesis, the star formation history study of this cluster determined that the cluster is comprised of a single population of stars that have the same age and metallicity. The study also determined an age and metallicity that are very typical for globular clusters. These results are not surprising, of course, but provide some confidence that the method used to determine the star formation history is working as it should.

2.6 Summary

A method for determining the star formation histories of nearby galaxies has been presented, along with some tests to determine how well it can solve for star formation histories and react to problems in the input data. This is quite useful, as the details of the star formation history calculation for a given set of input parameters can be done extremely quickly, allowing for photometric determinations of the distance, extinction, IMF, and/or metallicity in addition to the star formation rates.

Although stellar evolutionary models are heavily relied upon for this analysis, it is possible to make the star formation history solutions less sensitive to the less certain phases of stellar evolution. It is also possible to reproduce errors in stellar photometry by the use of artificial star tests, so that synthetic photometry will be of the same quality and have the same magnitude limits as the real photometry.

The tests against simulated data show a number of things. First and most importantly, a single fit parameter such as χ^2 is adequate for star formation history studies, as long as the color-magnitude grids are smoothed to increase the signal to noise in each bin and make the statistic more sensitive to larger-sized features. Second, this parameter is sensitive enough to distance, metallicity, and reddening that the solution for the star formation history can also determine these quantities to high precision. Finally, an important test of whether or not an artificial population of known history could be reconstructed was successfully made, with the primary difference from an actual analysis being that the models perfectly matched the data. Interestingly, no previous authors have attempted such a test on their methods. In this test, the correct answer was in fact determined successfully, which is encouraging and proves that this is a useful method for star formation history studies.

The questions remaining from the previous tests are whether or not the models are good enough to work on real data, and whether or not the numerical solution would be able to work despite the additional problems always inherent in observations. This test was made on the WLM globular cluster, and it was successfully carried out. As hoped, the solution told of a single old and relatively metal-poor population, exactly what would be expected for a globular cluster. Despite the fact that the models were imperfect for the cluster, the solution still worked properly, and distance and extinction were also correctly determined.

As a result of the comprehensive testing, we can set out to analyze composite populations with confidence that the results we are getting are accurate. These studies are shown in the next chapter.

Chapter 3

THE STAR FORMATION HISTORY OF WLM

3.1 Introduction

WLM is a dwarf irregular, located approximately 900 kpc from the Milky Way. It is separated from other Local Group galaxies, which makes it an interesting case for the study of formation and evolution of galaxies. Its dominant structure is a bar, with a fainter halo of stars surrounding it.

Previous work has been done on this galaxy (CCD studies by Ferraro et al 1989 and Minniti & Zijlstra 1997, as well as a photoelectric study by Sandage & Carlson 1985), but at the distance of WLM, these studies reach an absolute magnitude $M_V = \sim -1$. Despite this limitation, Minniti & Zijlstra (1997) were able to discern that the color gradient observed by Ables & Ables (1977) is caused by a population gradient. Further studies of the nature of this population difference have not been made, nor have studies of the star formation history of the older stars been made.

With HST observations of WLM, we are now able to peer much deeper into the stellar content of this galaxy, with quality V photometry to magnitude 27 ($M_V = \sim +2$). These data provide the opportunity to study the star formation history in a quantitative manner, using the method detailed in the previous chapter.

The metallicity enrichment history has not been studied extensively for this galaxy either, with only two solid estimates of the metallicity. Hodge & Miller (1995) used spectra of two HII regions in WLM to deduce a current metallicity of approximately -1.15 $\pm$ 0.2, while Minniti & Zijlstra (1997) estimated that the old stars have a metallicity of -1.45 $\pm$ 0.2 through photometry. These two figures provide rough endpoints of the enrichment history, but are very uncertain (to the point that both are consistent with -1.3). A better understanding of this galaxy's enrichment history is possible through the HST data presented here.

Goals for this study will be:

- Checking the globular cluster distance obtained in Chapter 2 with that obtained through an RGB tip calculation.

- Dating the oldest stars in the galaxy, and determination of star formation rates since that time.

- Determining the chemical enrichment history and comparing with estimates of the old star metallicity and measurements of the HII region metallicities.

- Determining the nature of the stellar population differences. Has the star formation rate in the bar increased recently, that in the halo decreased, or a combination of the two?

- Quantifying the recent star formation history differences: how much different are the recent star formation rates in different regions, and how long have they been different?

3.2 Data

3.2.1 Observations

The images used here were the WF chip images taken with the WLM globular cluster data described above. Two exposures were taken with the F555W filter of exposure times 2600 and 2700 seconds; two were taken with the F814W filter for 2700 seconds each. The alignment of the chips put WF2 the closest to the bar of the galaxy, WF3 further out, and WF4 well outside the bar. Cosmic ray cleaning was made with a routine similar to that of the IRAF task CRREJ. Cleaned V images of the three fields are shown in Figure 3.1.

3.2.2 Reduction

Photometry was carried out with the HSTPhot package discussed in Appendix A. The photometry was determined separately for the three chips for the study of recent star formation as a function of position, as well as combined for the study of the long-term star formation history of WLM. The CMDs are shown in Figure 3.2.

3.3 Analysis

3.3.1 Distance to WLM

Although a distance to WLM was obtained in the study of the cluster, it is useful to check this calculation through a more conventional TRGB calculation (Lee et al 1993). The TRGB in this data set is at $I = 20.80 \pm 0.03$, determined by looking for the most significant drop in the RGB LF, and is identical to that determined by Minniti & Zijlstra (1997). Correcting for the extinction $A_V = 0.07 \pm 0.06$ determined for the globular cluster in Chapter 2, this value changes to $I_0 = 20.73 \pm 0.04$. (There is no evidence for a significant amount of internal or differential reddening in this data, so the cluster value was adopted here.) Following the Lee et al (1993) formula, we calculate a distance modulus $(m - M)_0 = 24.76 \pm 0.1$, which is within agreement of the $(m - M)_0 = 24.72 \pm 0.09$ calculated for the globular cluster in Chapter 2. The cluster distance will be used for the calculations below, given its lower uncertainty. The cluster extinction will also be adopted, as there is no evidence for differential reddening in the WLM field stars. (Were there differential reddening, the red edge of the RGB would be much more diffuse than is observed.)

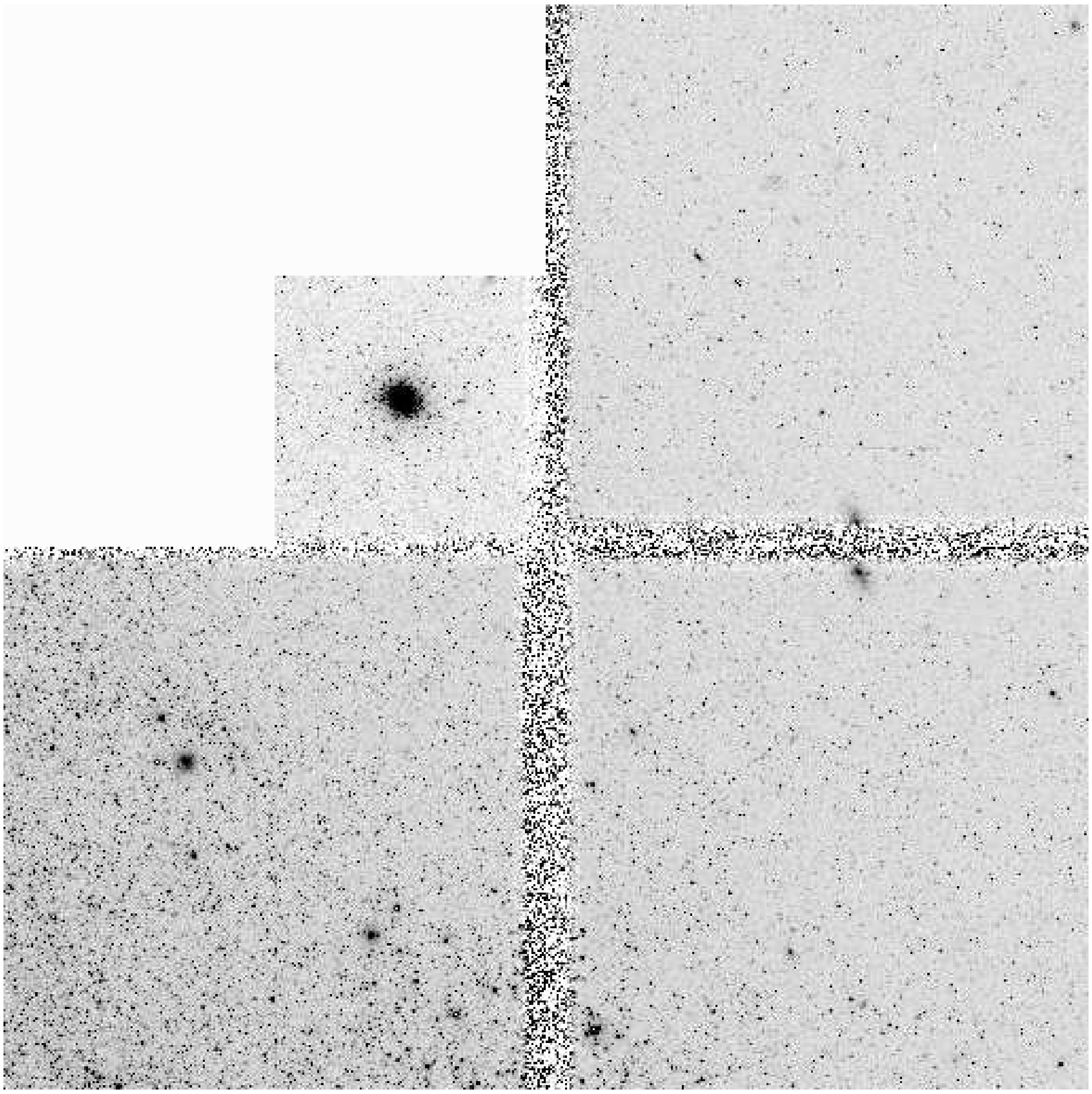

Figure 3.1: Combined V image of WLM after cosmic ray cleaning. WF2 is in lower left, WF3 in lower right, and WF4 in upper right.

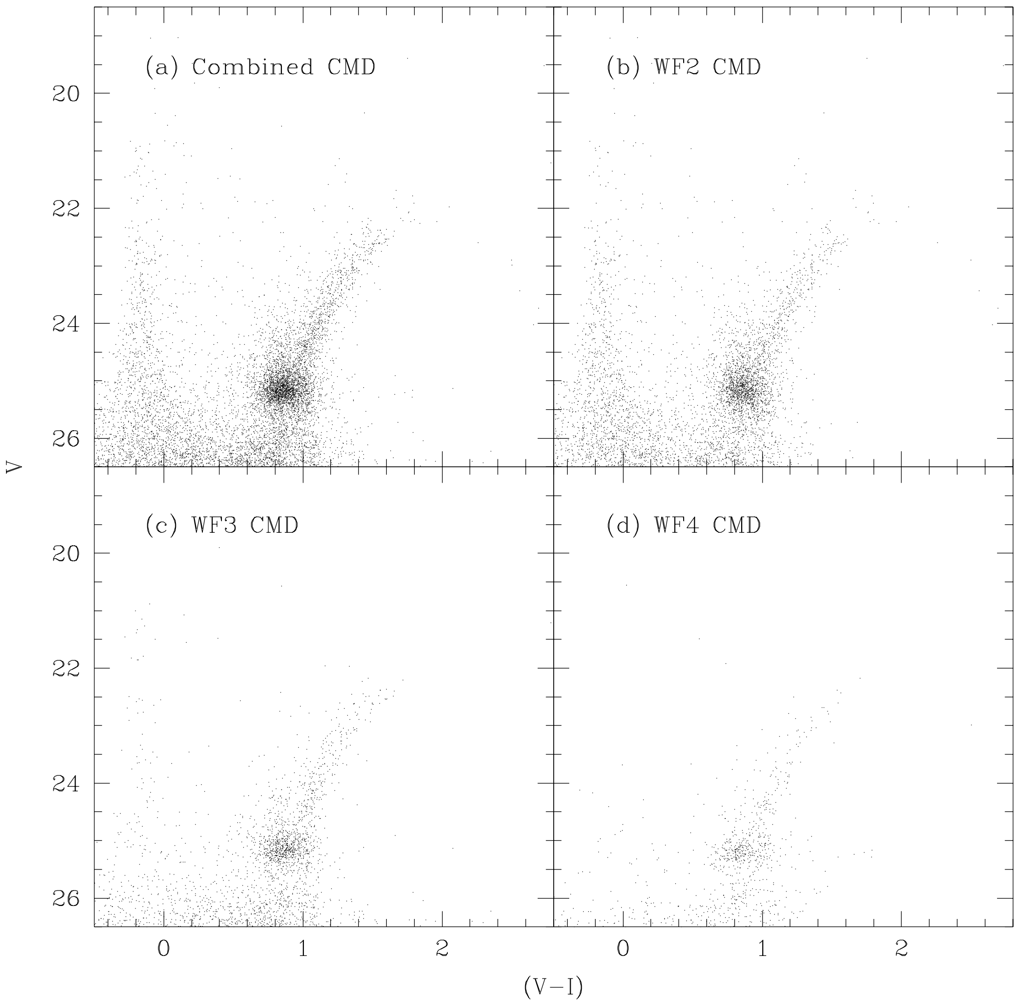

Figure 3.2: Color-Magnitude Diagrams of WLM

3.3.2 Star Formation History Solutions

For all CMD analyses in this Chapter, the Padova isochrones (Girardi et al 1996, Fagotto et al 1994) were used. These models include later (post-helium flash) phases of stellar evolution, providing completeness at the cost of accuracy. For the purpose of matching the entire observed CMD with synthetic data, however, it is far better to use models with slightly incorrect AGB tracks than ones with no AGB tracks.

The χ^2 fitting parameter was modified slightly to make it less sensitive to common fitting problems. First, the weight given to bins in the AGB, horizontal branch, and red clump regions of the CMD was decreased, and the χ^2 value for any bin not allowed to exceed 10. The decreased weights were for the most noticeable theoretical isochrone problems, while the cap on the χ^2 from any one bin was introduced to prevent the fit from being driven by other unfittable (or nearly unfittable) CMD regions. Finally, to combat contamination of the image, a small constant value was added to the σ^2 denominator. Thus the modified χ^2 fit parameter has the functional form

$$\chi_i^2 = \frac{(O_i - \sum_j c_j M_{i,j})^2}{\sum_j c_j \sigma_{i,j}^2 + N}, \tag{3.1}$$

following the definitions from Chapter 2, with N being equal to 10% of the average number of stars per bin. This will prevent the problem in which a bin with a small number of observed stars and no synthetic stars from getting a high χ_i^2 (because $\sigma_{i,j}$ is related to the number of synthetic stars in the bin), while a bin with no observed stars and a small number of synthetic stars gets a moderate or low χ_i^2. As is shown in Figures 3.5 and 3.6, the modified χ^2 parameter gives poor fits only in places where the observed and synthetic CMDs are, in fact, significantly different.

3.3.3 Era of Initial Star Formation

In addition to the distance and extinction, the time of initial star formation in WLM is an essential parameter to calculate before determining the galaxy's star formation history. This is because the evolutionary models reproduce neither the horizontal branch nor the red clump structures well, and thus a blind solution using the models can easily be thrown off in dealing with these old populations. In the case of WLM, doing so would cause the models to attempt recreating the tight red clump as a red horizontal branch. But clearly the field has little or no horizontal branch, which sets the upper limit on large amounts of star formation to $\sim$12 Gyr ago.

To determine the age of initial star formation, a set of history calculations was made that were sensitive to the age of initial star formation, with the distance and extinction adopted from above and the enrichment history allowed to vary. Of the possible starting points, the oldest (12 Gyr) gave the best fits and is used below. The question of whether the galaxy actually had *no* star formation from the formation of the globular (14.8 $\pm$ 0.7 Gyr ago) to 12 Gyr ago, or whether the galaxy had a non-zero but very small star formation rate cannot be solved from this data, as there are stars where the horizontal branch would be expected, but no horizontal feature is seen in the CMD. Regardless of whether or not the galaxy waited until 12 Gyr to form any stars, it clearly waited until that point to form a measurable number of stars.

3.3.4 Global Star Formation History and Enrichment

The star formation history study was broken into two parts. First was the study of the global star formation history and enrichment, which used the combined CMD from all three WF chips. For the size of the region studied ($\sim$500 pc), any stars formed more than a Gyr ago should be well-mixed by now (with a random velocity of 1 km/sec, a 500 pc region would be mixed in 500 Myr), and thus the combination of the CMDs will simply improve the signal-to-noise of the results. Additionally, the best star formation history information is only available to 1.5 Gyr, which is where the main sequence drops below the limit of good photometry.

Using the distance, extinction, and age of initial star formation determined above, a set of star formation history calculations was made in which the enrichment his-

Table 3.1: Star Formation History of WLM

Age (Gyr)	SFR ($10^{-5} M_{\odot}$/yr)	[Fe/H]
0–1	14 ± 4	-1.16 ± 0.13
1–2.5	9 ± 5	-1.23 ± 0.12
2.5–5	7 ± 3	-1.25 ± 0.11
5–7	4 ± 8	-1.29 ± 0.09
7–9	14 ± 21	-1.40 ± 0.09
9–11	12 ± 23	-1.44 ± 0.09
11–12	144 ± 63	-1.49 ± 0.12

tory (initial metallicity, current metallicity, and function of metallicity increase) was allowed to vary, with the best-fitting solutions averaged with a weighted average to determine the best results. Uncertainties were calculated by adding the standard deviations from the fitting procedure to the standard deviations of monte carlo simulations in quadrature, so that both uncertainties resulting from the parameters and those from the fit itself are included in the final results. The solution was made using 6623 stars with V between 20.5 and 26.5 and I between 20 and 26. Star formation rates are given assuming a Salpeter IMF with cutoffs at 120 and 0.1 $M_{\odot}$, which was used out of necessity because this data does not extend beyond the old main sequence turnoff and therefore an IMF cannot be measured. An IMF error for the old stars would introduce a gradient into the data. For example, using too shallow of an IMF would generate fewer stars in the older synthetic CMDs, and thus return too large of a star formation rate in the very old times. Results are shown in Table 3.1 and Figure 3.3.

A synthetic CMD for the region reconstructed from the models, artificial star results, and determined star formation history is shown in Figure 3.4a. A glance shows that the fit appears to be good, with the primary differences between the two

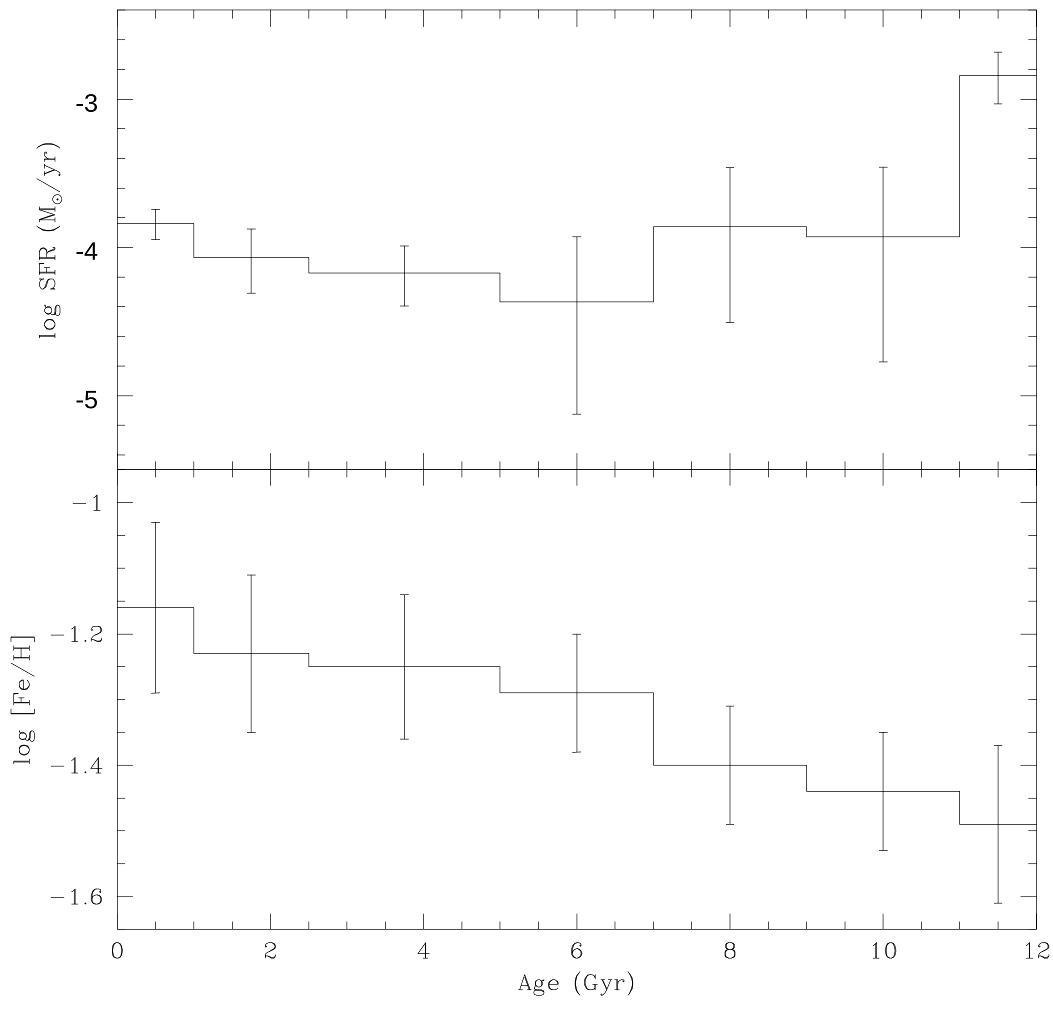

Figure 3.3: Star Formation History of WLM

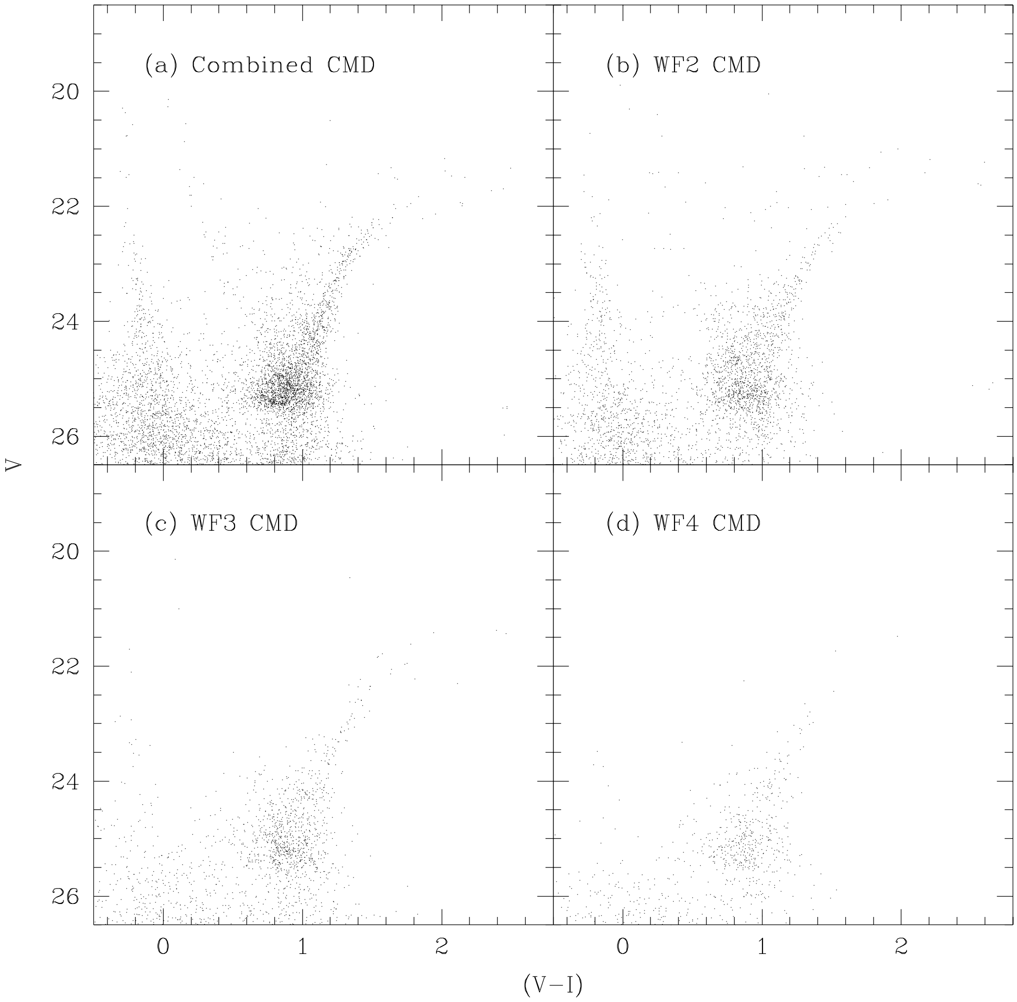

Figure 3.4: Reconstructed Color-Magnitude Diagrams of WLM

diagrams (more diffuse red clump, sharp blue loop edge, and brighter AGB) resulting from inaccuracies of the theoretical isochrones. The upper main sequence is less populated reconstructed CMD, which most is a result of the assumption of constant star formation rate over the past 200 Myr. More likely, the recent star formation rate is higher than the 200 Myr average, thus producing a higher fraction of upper main sequence stars than if the star formation rate have been constant over the entire period. At any rate, the recent star formation rates are studied in the next section, and will not be dealt with here. The region near the base of the blue loop branch is much more heavily populated in the reconstructed CMD than in the observed, something again a result of the models. Other minor difficulties in reconstructing the CMD include the RGB width above the red clump and the difficulties in modeling the AGB, both of which can be attributed to the state of the evolutionary models. What is encouraging is that the CMD features that are expected to be correct, namely the position of the main sequence, red giant branch, and red clump, are indeed correct. The sharpness of the red giant branch is approximated closely, as well as its luminosity function.

A more detailed comparison is shown in Figures 3.5 and 3.6, which show the binned CMDs that were used for the solution (0.1 magnitude resolution in $V-I$ and 0.3 magnitude resolution in V for Figure 3.5; 0.05 $V-I$ and 0.15 V for Figure 3.6), as well as the residuals and the fit parameter values. Magnitude limits in the plots are $20.5 < V < 25.9$ and $-0.55 < V-I < 2.85$. The subtracted CMD is shown at three times the contrast level of the two CMDs (darker being undersubtracted and lighter oversubtracted), while the modified χ is shown on a scale from 0 to 3.2. As the residuals show, the only large difference between observed and reconstructed CMDs occurs at the red clump, where the more diffuse reconstructed clump causes undersubtraction in the clump and oversubtraction around it. This region provides the largest contribution to the fit parameter, which is at its maximum value of 3.2 over most of the red clump region. The erroneous AGB modeling provides very little to

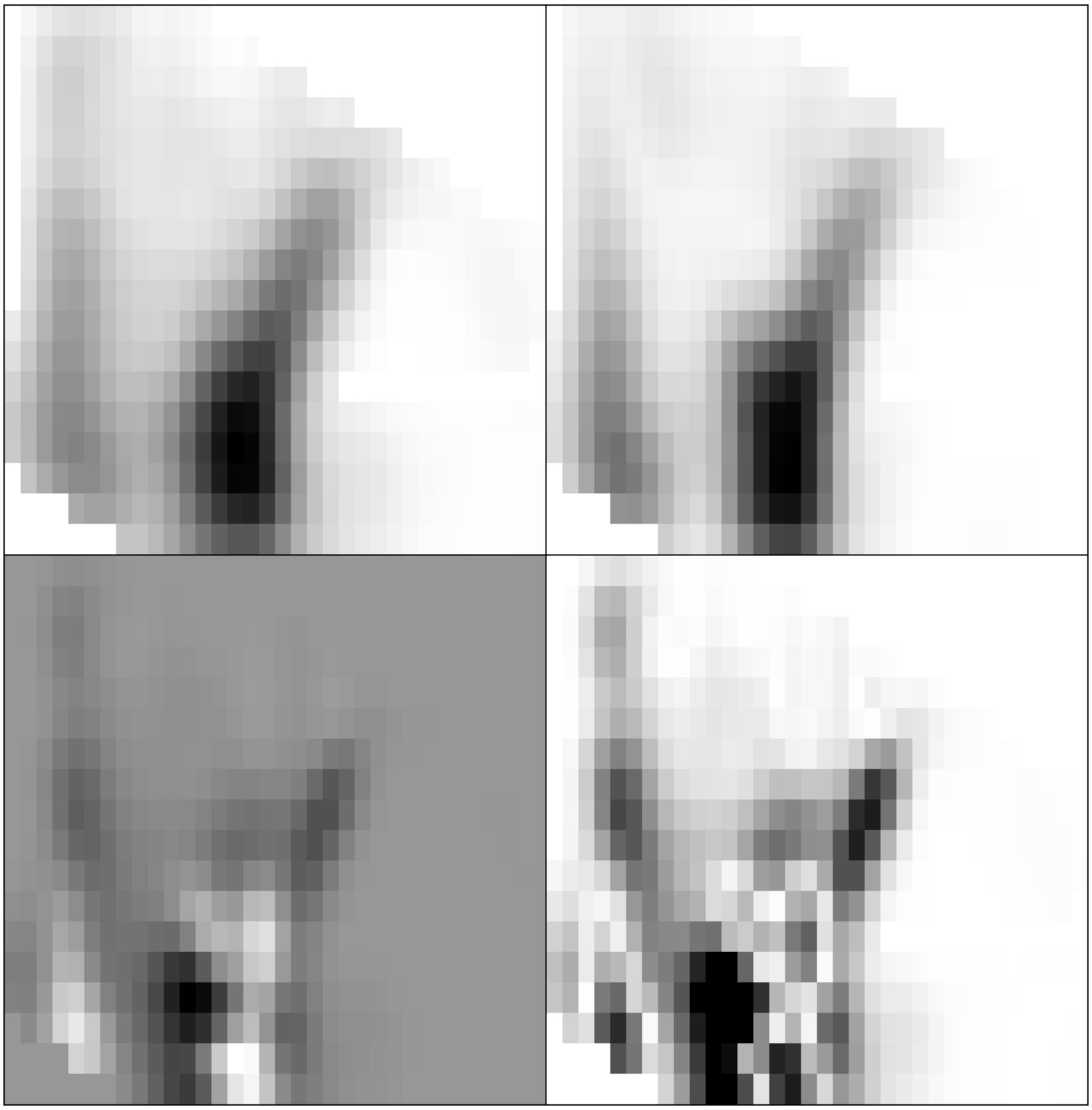

Figure 3.5: Comparison of Observed and Reconstructed CMDs. Upper left is the binned observed CMD; upper right is the binned reconstructed CMD. The lower left shows the subtracted diagram, while the lower right shows the modified χ values at each location. See text for explanation.

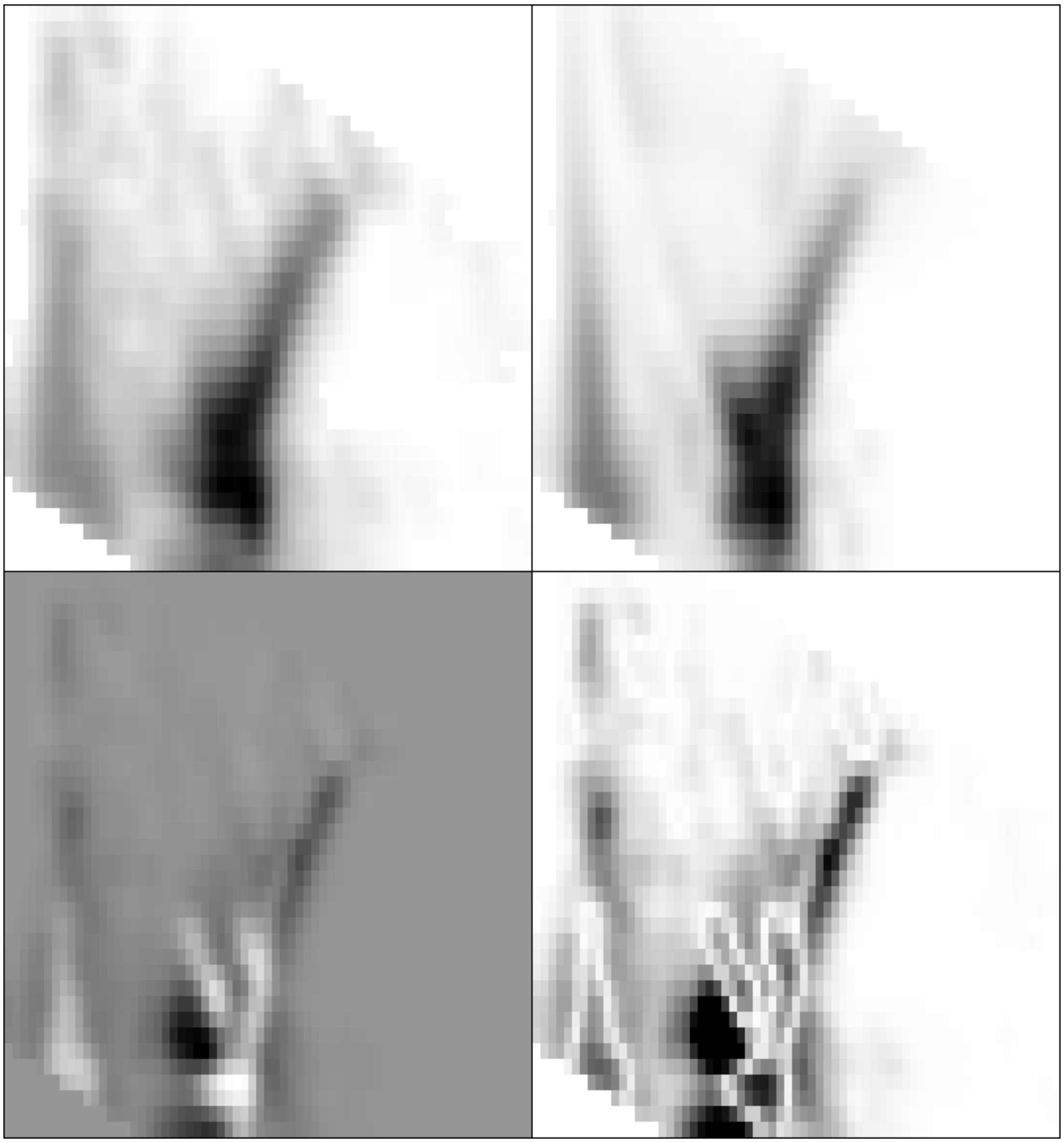

Figure 3.6: Comparison of Observed and Reconstructed CMDs. Same as Figure 3.5, but at twice the resolution.

the fit, as it contains few stars. As noted above, the main sequence is undersubtracted at the bright end (V between 20.8 and 21.7) and further down, most notably between V of 22.6 and 23.5. The lower of the two is a significant deviation, likely indicating that much of the star formation during the past 200 Myr came in a burst ~25 Myr ago.

The most significant cause for concern is the 2.9σ errors along the red edge of the RGB. This is created by the models' inability to perfectly model the RGB. A compromise was made between finding the correct RGB position, shape, and luminosity function, with some error being unavoidable. In this case, the synthetic RGB is slightly narrower, matching the observed RGB well on the blue side but not on the red side. Increasing the metallicity to manually push the synthetic RGB to the red will alter the RGB LF, the net effect being to increase the fit parameter. Increasing the age of the oldest stars to match the CMDs would cause a horizontal branch in the synthetic CMD, again making the problem worse. Thus, while an imperfect fit, the program appears to have chosen one which minimizes the residuals as well as possible.

Looking at the calculated star formation history, it seems that the star formation of WLM began with a strong initial burst, beginning approximately 12 Gyr ago. This burst contained ~58% by mass of the total star formation that WLM has seen. After that initial burst, the star formation rate fell to approximately 7% of the average rate for the first Gyr, where it has remained since then. There may or may not have been a decreased star formation rate during the 2.5 to 7 Gyr period, the large uncertainties caused by the difficulty of observing stars of that age (especially when the models cannot reproduce the AGB).

The metallicity enrichment of WLM shows an early abundance of -1.49 $\pm$ 0.12 (agreeing with the -1.45 $\pm$ 0.2 of Minniti & Zijlstra 1997), which is similar to that of the globular cluster (determined in the previous chapter to be -1.51 $\pm$ 0.09). The similarity of the abundances of the globular cluster and old stars strengthens the notion that very little was happening during the few Gyr between the cluster formation

Table 3.2: Recent Star Formation History of WLM Fields

Age (Gyr)	WF2 SFR ($10^{-5}M_\odot$/yr)	WF3 SFR ($10^{-5}M_\odot$/yr)	WF4 SFR ($10^{-5}M_\odot$/yr)
0.0−0.2	16.1 ± 1.4	2.3 ± 0.5	0.2 ± 0.1
0.2−0.6	1.4 ± 1.3	0.1 ± 0.4	0.3 ± 0.3
0.6−1.0	16.7 ± 5.9	6.8 ± 2.7	1.5 ± 1.0
1.0−1.5	14.8 ± 10.8	7.0 ± 5.5	3.1 ± 2.4
intermediate	5.3 ± 2.4	2.6 ± 1.7	1.3 ± 1.0

and the onset of significant star formation. The metallicity has continually climbed since that time, reaching a current value of -1.16 ± 0.13. This value for the current metallicity agrees well with the -1.15±0.2 found by Hodge & Miller (1995) for two HII regions in WLM.

3.3.5 Recent Star Formation History

In contrast to the well-mixed old stars, Minniti & Zijlstra (1997) and Ferraro et al (1989) found a stellar population gradient in WLM, with the bar region contributing more recent star formation. As their data extended to $V = \sim 24$, it was impossible to quantify this result, but with the HST data here a quantitative analysis can be done separately on different parts of the galaxy. For the study of recent star formation, the three fields were kept separate, with 3946 stars in WF2, 1939 in WF3, and 738 in WF4. The analysis was carried out using the distance, extinction, and enrichment calculated above, with results in Table 3.2 and Figure 3.7.

Reconstructed CMDs of the three fields are shown in Figures 3.4b-d. As with the combined CMD, the chief differences between observed and reconstructed CMDs are in the red edge of the RGB, the red clump sharpness, and the AGB position, resulting from the models' uncertainties in late phases of evolution. The reconstructed WF2 field, in particular, shows a very wide red clump, apparently due to overestimated

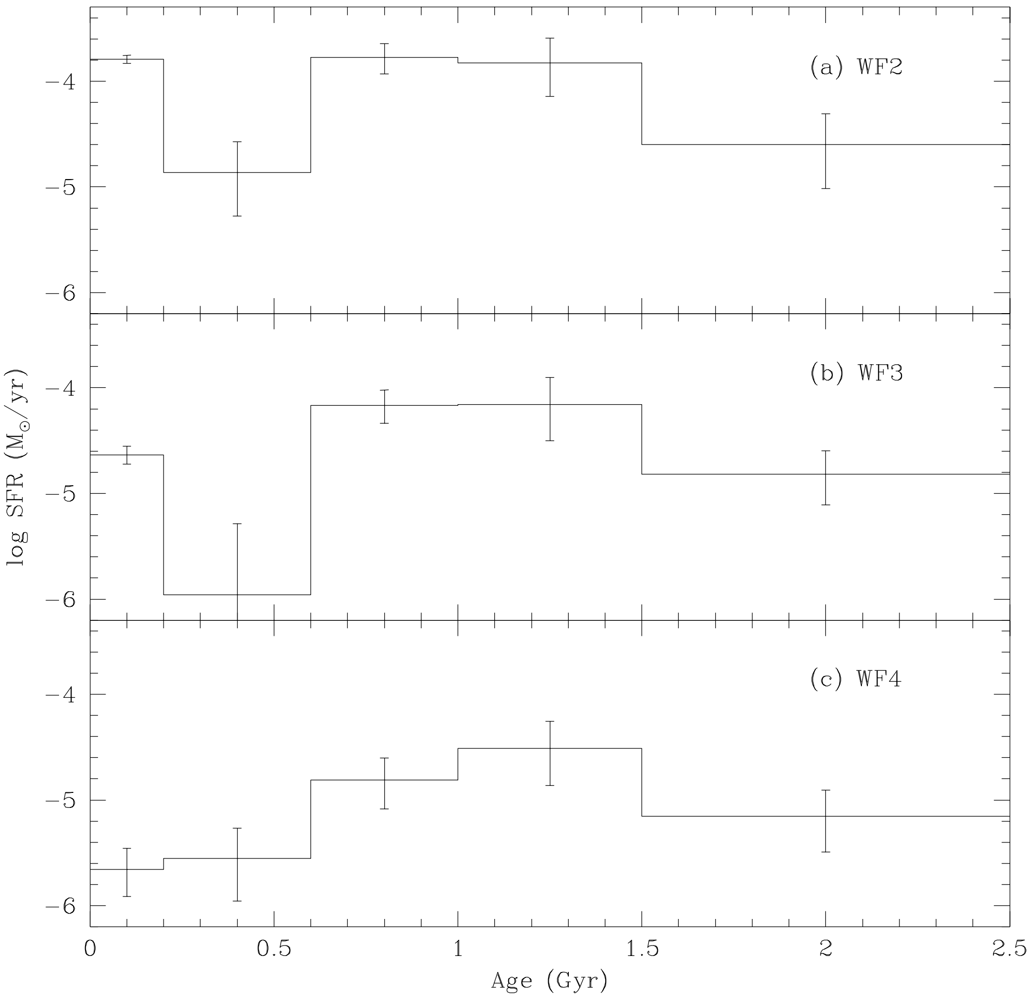

Figure 3.7: Recent Star Formation History of WLM Fields

incompleteness and crowding errors in that field. Otherwise, the fits are excellent, as with the combined CMD.

As hinted by the global star formation history, WLM has had a burst of star formation activity during the past 1.5 Gyr and possibly longer. Determining star formation rates beyond 1.5 Gyr is much more difficult, as the main sequence is below the limit of the good photometry, so only an average star formation rate from 1.5 to 11 Gyr is given for each field. The WF2 field, which is the closest to the galaxy's center (and includes the outer regions of HII complexes C1 and C2 as well as including all of HII region 1 (Hodge & Miller 1995), contains most of the recent star formation (87% of the star formation in the past 200 Myr), while the 600 to 1500 Myr star formation burst is more evenly distributed between the regions, which can be explained through mixing. As noted in the previous section, residuals in the CMD subtraction indicate that most of the star formation in the 0-200 Myr period is the result of a burst $\sim$25 Myr ago, rather than a constant star formation rate over the entire 200 Myr. The lack of HII regions (aside from the small region 1 noted above) in the frame supports the conclusion that the region studied does not currently have much star formation.

To test this hypothesis, the star formation history simulation from the previous section was modified to include a burst from 25 to 40 Myr. The results indicate that the burst is responsible for 45% of the star formation during the past 600 Myr and that the non-bursting star formation rate for the past 600 Myr appears to have been a constant $4.0 \times 10^{-5} M_{\odot}/\mathrm{yr}$. (This also confirms the notion that the extremely low star formation rate from 200 to 600 Myr in Table 3.2 was a result of oversubtraction caused by the burst.)

The Hodge & Miller (1995) data on WLM provide an additional constraint on the current star formation, as they find a formation timescale of 150 Gyr for the galaxy, longer than the value of 62 Gyr that would be calculated from the current star formation rate above. Two possible causes of this factor of 2.5 difference can be pinpointed. First, our sample consists of only a small fraction of WLM (one including a small HII region and bordering two large HII complexes!), and the global star formation timescale could be significantly different from that found in this region. Second, it is possible that the estimate of the lifetime-averaged star formation rate presented here is more accurate, as this is the first star-formation history work for WLM that uses HST data. However, without data of HST quality elsewhere in the galaxy, it is likely not possible to determine which (or perhaps a combination of the two) is the source of the difference.

The results confirm the previous findings of Minniti & Zijlstra (1997) and Ferraro et al (1989). The WF2 field, which is mostly in the WLM bar, has seen the most star formation activity in the recent 2 Gyr star formation burst, accounting for ~87% of the total recent star formation. (For comparison, the WF2 field contains ~55% of the old stars.) The WF3 field, which is located on the edge between the bar and the halo, is intermediate, with a small amount of star formation during the past 200 Myr. Finally, the WF4 field, located entirely in the halo, appears to have had essential no recent star formation, as the enhancement in the 1.0−1.5 Gyr bin of the WF4 field could be accounted for by mixing that has occurred since those stars formed. In fact, the WF4 star formation rate is currently significantly below its average rate for the past 11 Gyr.

3.4 Summary

HST F555W and F814W photometry of a portion of the WLM galaxy has been presented. A distance modulus of 24.72 ± 0.09, previously calculated for this galaxy through photometric fitting of the globular cluster in Chapter 2, has been shown to be consistent with a distance determination from the RGB tip. The galaxy's oldest stars appear to be 12 Gyr old, with an abundance [Fe/H] of -1.49 ± 0.12 for the initial star-forming burst. It is calculated that roughly 58% of the galaxy's star formation occurred during this time. Since this initial star-forming event, the overall star formation rate has been approximately 7% of the average star formation rate during the first Gyr, and has been relatively constant, with the metallicity slowly rising to its current value of [Fe/H] = -1.16 $\pm$ 0.12.

Increased activity has taken place recently, for at least 1500 Myr, the limit of main sequence photometry. The activity for stars older than a Gyr cannot be pinpointed because of mixing within the galaxy, but the current star formation is limited to the bar of the galaxy. This activity seems to have largely ended about 600 Myr ago, giving way to a period with an average star formation rate significantly below the galaxy's average rate of $1.0 \times 10^{-4} M_{\odot}$/yr.

A significant burst seems to have taken place recently (ending 15 Myr ago), accounting for about half of the star formation during the past 600 Myr, with a low-intensity but steady star formation accounting for the other half. This even was concentrated in the bar of the galaxy, with almost no detectable star formation in the halo during this period.

In summary:

- The globular cluster distance modulus of 24.72 $\pm$ 0.09 is consistent with that obtained from the TRGB of the field stars.

- An initial burst of star formation began approximately 12 Gyr ago, with a metallicity of -1.49 $\pm$ 0.12, lasted for about one Gyr, and accounted for $\sim$58% of WLM's total star formation.

- The initial metallicity of -1.49 $\pm$ 0.12 is consistent with the photometric measurement given by Minniti & Zijlstra (1997). The metallicity gradually rose after the initial burst to a value of -1.16 $\pm$ 0.13 since that initial burst. This value is consistent with the Hodge & Miller (1995) measurements of HII regions.

- The star formation rate seems to have dropped off significantly during the past 600 Myr, with a formation timescale of 62 Gyr calculated for this data set. A significant burst, accounting for nearly half of the star formation during the last 600 Myr, ended about 15 Myr ago, and was confined to the WLM bar.

Chapter 4

THE STAR FORMATION HISTORY OF THE LMC

4.1 Introduction

The question of the star formation history of the LMC is a complex one. Nearly all previous work has focused on the northern part of the disk, beginning with Butcher (1977). Butcher found a break in the luminosity function, which he interpreted as resulting from most of the stars having been formed during the past 3-5 Gyr. These results were confirmed by Bertelli et al (1992), who made the first CMD reconstruction attempt on LMC field stars. Bertelli et al (1992) added the result that the star formation rate over the past 3-5 Gyr has been as much as ten times the earlier rate. This picture agrees with that determined by studies of bright LMC clusters, as summarized by Olszewski et al (1996). There is only one known LMC cluster with an age between 4 and 12 Gyr; all other clusters are either older or younger (most are younger).

More recent results (Holtzman et al 1997, Stappers et al 1997, Geha et al 1998, and Olsen 1998) relying largely on HST data contradict this, however. Holtzman et al (1997) find that the burst has been more recent (2-3 Gyr ago) and is only a factor of 3 greater than the previous star formation rate. Thus they conclude that fully half of the stars are older than 4 Gyr. Olsen (1998) used the method presented in Chapter 2 to study one HST field in the northern part of the disk (as well as four in the bar which are not described here), and confirmed these results, adding that the star formation rate appears to have been sporadic rather than constant. The bursting star formation rate is supported by the chemical evolution models of Pagel and Tautvaisiene (1998). He also confirmed previous hints that the star formation in this part of the disk has decreased over the past 0.5 Gyr.

For the upper main sequence, Holtzman et al (1997) find a metallicity of between [Fe/H]=-0.7 and -0.4, while Geha et al (1998) find the [Fe/H]=-0.4 isochrone to fit the best. The abundances of the old stars are less constrained, with both groups finding that the red giant branch appears to have an old population with [Fe/H]=-1.7 but could have the upper RGB dominated by younger (less than 2 Gyr) stars with [Fe/H]=-1.3.

This chapter will present data for two fields near the Constellation III region, in the northern part of the LMC disk, as well as a star formation history analysis.

Goals for this study will be:

- Determining a photometric distance to the LMC, and comparing with other measurements.

- Dating the oldest stars in the galaxy, and determining of star formation rates since that time. Special importance will be attached to the 3-5 Gyr range, and the ratio of recent to intermediate age star formation rates, as all previous ground-based work has supported one interpretation, while all HST-based work has supported another.

- Determining the chemical enrichment history, and whether the red giant branch contains a significant number of young stars.

- Comparing the two fields for differences in recent star formation rates.

Table 4.1: Positions of the LMC Fields, epoch 2000

Field	RA	Dec
NW	$5^h\ 10^m\ 02.1^s$	$-66^\circ\ 36'\ 24''$
SE	$5^h\ 40^m\ 12.7^s$	$-67^\circ\ 11'\ 46''$

4.2 Data

4.2.1 Observations

UBV images of five fields in Constellation III and two fields outside the region were obtained by Deidre Hunter at the Cerro Tololo Inter-American Observatory (CTIO) 26, 27, 30, and 31 January 1993 with a 2048×2048 Tektronix CCD on the 0.9 m telescope. Conditions were photometric (except as mentioned below), with seeing typically 1-2$''$. The fields outside the Constellation will be the ones studied here, referred to as the SE and NW fields, with positions given in Table 4.1. Images in each filter were obtained with at least two integration times to give greater dynamic range, as well as for cosmic ray cleaning. Standard stars were also observed, chosen from the lists of Graham (1982) and Landolt (1973, 1983).

Image reduction was done normally, although there were some problems with the images. The CCD was non-linear, with an error of 0.015 magnitudes per magnitude, which was corrected with a correction determined by Alistair Walker (private communication). Some standard star images showed a step-function in the bias, for which only the part of the images with the normal bias was used so that no additional uncertainty was added to the photometry. This bias problem was not observed in the data frames. Additionally, all images with integration times of $\leq$5 seconds were corrected for the finite time required for the shutter to open and close. Bright but unsaturated stars also had additional structures in their PSFs that could not be accounted for by PSF fitting, so those stars were not included in the photometry.

An iterative fit for the transformations to standard filters was made, with a zero point, airmass term, and color term for each filter. We required that the color term and zero point were constant for the four nights, allowing only the extinction to vary. In the data for the second night, there were two U images and one B image for which the standard star photometry was 0.15 magnitudes fainter than the rest. Because the images were interleaved and because the offset was exactly the same in each case, the offset is unlikely to be due to clouds, although no other problems were obvious. All other images agreed with the brighter level, so those three images were removed from the solution. The rms's of the final solutions were 0.05 in U and 0.02 for B and V.

4.2.2 Reduction

To obtain photometry, DAOPHOT (Stetson 1987) in IRAF was used with a procedure based on that described in Massey & Davis (1992). The main differences between our reduction method and that in Massey & Davis (1992) are due to the fact that our PSFs were allowed vary widely over the field, with sharper stellar profiles in the center and increasingly broad profiles with increasing distance from the center.

Each field was reduced separately, rather than combining fields of equal exposure time and filter before running the photometry. Although this took more time, the photometry and artificial star tests obtained were more accurate. For this work, a highly automated method was used, so that the photometry reduction sequence used in the artificial star testing could be identical to that used to reduce the fields. This is critical for getting an accurate estimate on the true uncertainties of the photometry in crowded fields. Especially with the variable PSF across the image, our automated procedure caused a number of faint stars to be missed. However, since the limiting magnitude was determined more by crowding than by photometric uncertainties, the loss of some faint stars caused no effect on the final results.

Since we chose to make two passes through the algorithm to find stars, it was decided to use a different FWHM for each. The first pass used the FWHM near the center of the image, while the second pass used a larger FWHM, roughly that 2/3 of the way to the edge of the image. While this sacrificed some of DAOFIND's ability to locate faint stars in the wings of bright stars, it allowed us to find stars in the center of the image (where the PSFs are sharper) as well as on the edges (where the PSFs are wider) without lowering thresholds to the point of getting many false detections.

The PSF solution itself used a second order fit for PSF variations with position on the chip. A large number of PSF stars were used for this, between 30 and 40 stars evenly distributed across the image that were reasonably bright and separated from neighbors.

The final photometry output was processed to reduce the contamination due to bad pixels, cosmic rays, and field edges. This was done by making three cuts. First was masking out all stars within three pixels of a bad column, taking into consideration the y extent of the bad columns as well as the x positions. The second cut eliminated all stars returned with a χ^2 value from DAOPHOT greater than 2. Finally, a sharpness criteria was made, so that a star with an absolute value of sharpness either less than 0.5 or within 2σ of the distribution at that magnitude would be kept.

Once this was done, stars were matched between exposures of the same length in the same filter for those cases in which we had three or more exposures. A star was considered real if it was in at least half of the images, with the matching criteria considering both the magnitude of the star and the position. Then the lists were merged into one photometry list per filter by combining the photometry of stars found in different length exposures, weighted inversely by the DAOPHOT uncertainties. Finally, a UBV photometry list and BV photometry list were created by comparing the lists for each filter for stars at the same location in each.

To check the accuracy of our photometry, we compared our results with the Balona & Jerzykiewicz (1993) UBV CCD photometry near the NGC 2004 field and the Lucke (1972) BV photoelectric photometry of LH 77 (two of the Constellation III fields). Our values were consistent with the Balona & Jerzykiewicz (1993) results.

However, calibration problems on the first night (in which the LH 77 and SE fields were observed) were discovered because the reddening value obtained from the CMD was different from that obtained from the color-color diagram. Systematic offsets of $\Delta V = 0.010 \pm 0.009$ and $\Delta B = 0.031 \pm 0.011$ were seen between our photometry and the Lucke (1972) photometry, which we used to correct our photometry.

$V, B-V$ CMDs for both fields are shown in Figure 4.1. Unfortunately no data was available for foreground star subtraction (the fields studied here were taken as the background fields of a different study), meaning that foreground contamination cannot be corrected for. However, although Galactic foreground stars fall in the LMC's red giant branch and blue loop region, they will not follow the shape of any LMC isochrones. Thus their effect on the solutions should be mostly to increase the χ^2 of the fits, while not significantly affecting the results.

4.2.3 Artificial Stars

Normally, artificial star testing is used simply to determine the completeness levels as a function of color and magnitude. However, Gallart et al (1996) show that crowding can be an important or even dominant effect in the quality of the photometry, especially in crowded fields, such as those studied here. Using a procedure similar to that described in Gallart et al (1996), a database of artificial star data covering the magnitude and color ranges of interest was built that gives not just the completeness but also the difference in magnitude recovered from magnitude input. These tests were run on one long exposure per filter per field. (Testing the short exposures was unnecessary, as incompleteness is not an issue for the brightest stars.)

The reduction sequence for the fields with artificial stars was set to be identical to that for the original photometry, so that the artificial star results would have all sources of error in them. The only aspect that could not be reproduced was uncertainty in the PSF solution, as even the second-order PSF fit did not do a perfect job of modeling the deviations in the PSF over the image. The artificial stars had the

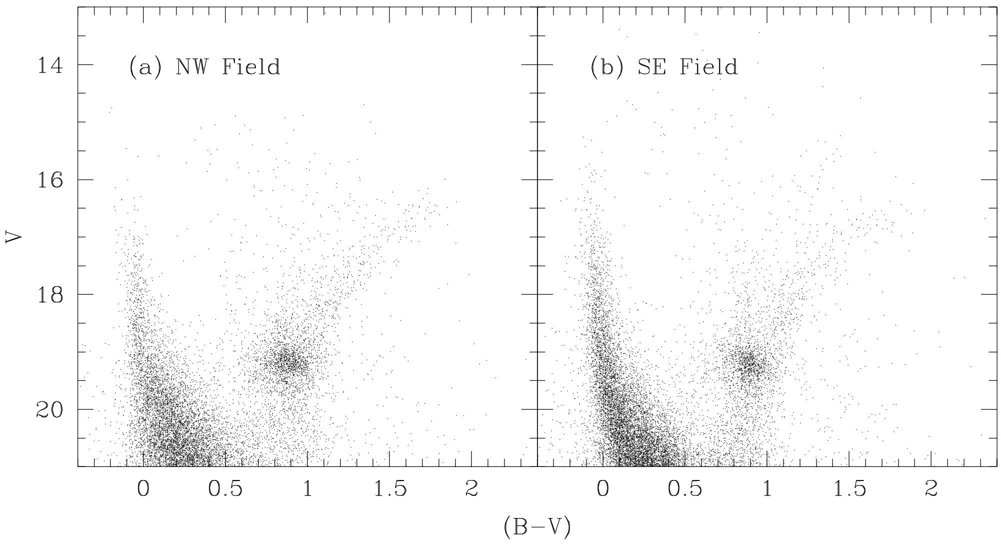

Figure 4.1: Field $B-V,V$ Color-Magnitude Diagrams for NW and SE fields

PSFs from the fit rather than the real PSFs.

Figures 4.2 and 4.3 show the completeness levels in the three filters, while Figures 4.4 and 4.5 show the photometric error as determined by the artificial star tests. The measured errors from the artificial star tests were significantly higher than the DAOPHOT uncertainties, which is expected for crowded field work. Using the completeness criterion, the SE field is complete to B=22.3 and V=21.8; using the photometry and crowding criteria, the cutoff of good photometry is lowered to B=19.5 and V=19.3. Values for the NW field are approximately 0.5 magnitudes shallower.

4.3 Analysis

4.3.1 Era of Initial Star Formation of the LMC

As with the WLM data presented in the previous chapter, the lack of a horizontal branch will be used to constrain the age of initial star formation to less than 12 Gyr. The same caveat holds for the LMC: we are not stating that no stars in these fields formed before 12 Gyr ago, only that there is no measurable amount of stars older than 12 Gyr here. A set of star formation history runs were made, with variable starting age of star formation (all possible ages 12 Gyr or less), and the star formation history beginning at 12 Gyr best reproduced the observed CMD. The modified χ^2 parameter devised for the WLM analysis was used for this and all other analyses in this chapter.

4.3.2 Global Star Formation History and Enrichment

For WLM, determining a distance and extinction was done separately from the star formation history analysis, something made possible by the presence of the globular cluster. This is not the case here, so the distance and extinction to the LMC were allowed to vary along with the enrichment history and star formation rates. The best fits were then combined, with standard deviations of the parameters of the best fits taken as the uncertainties in the solutions. For all CMD analyses in this Chapter, the

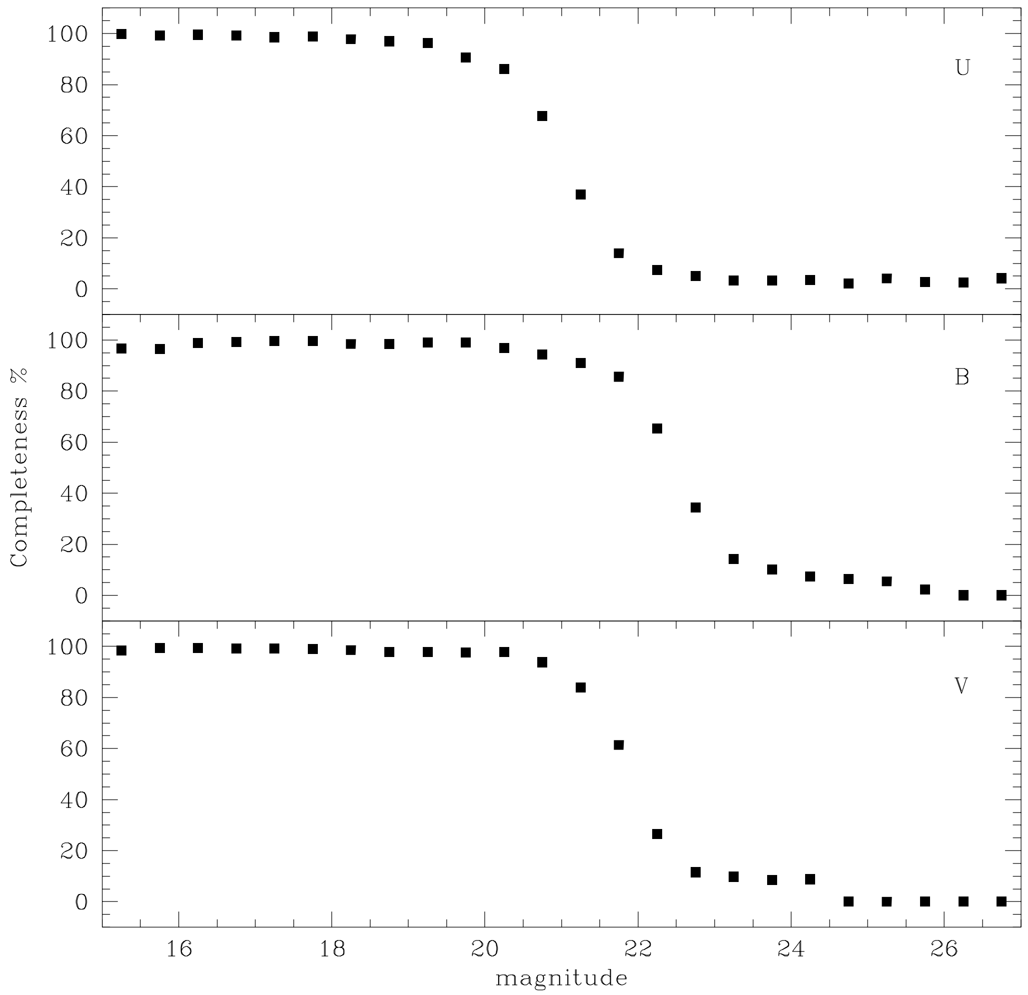

Figure 4.2: SE field completeness, as determined by the fraction of recovered artificial stars

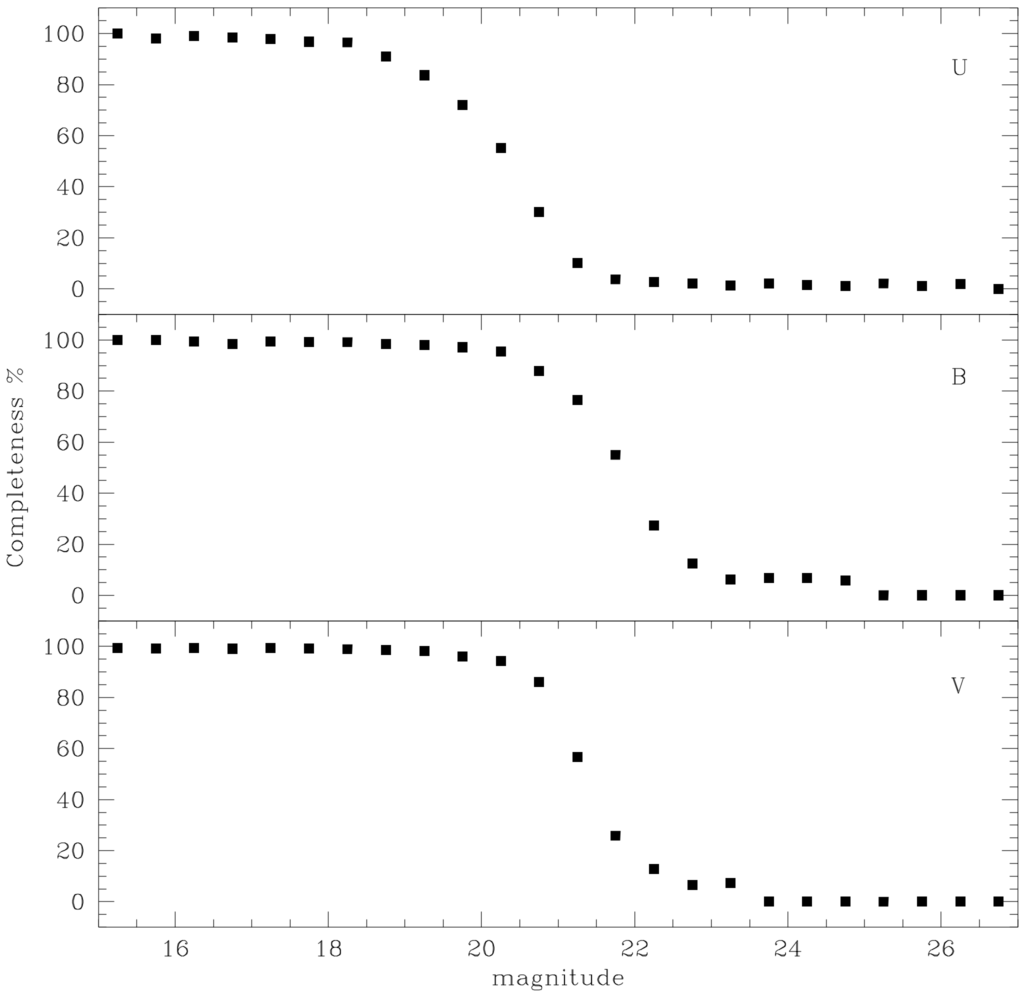

Figure 4.3: NW field completeness, as determined by the fraction of recovered artificial stars

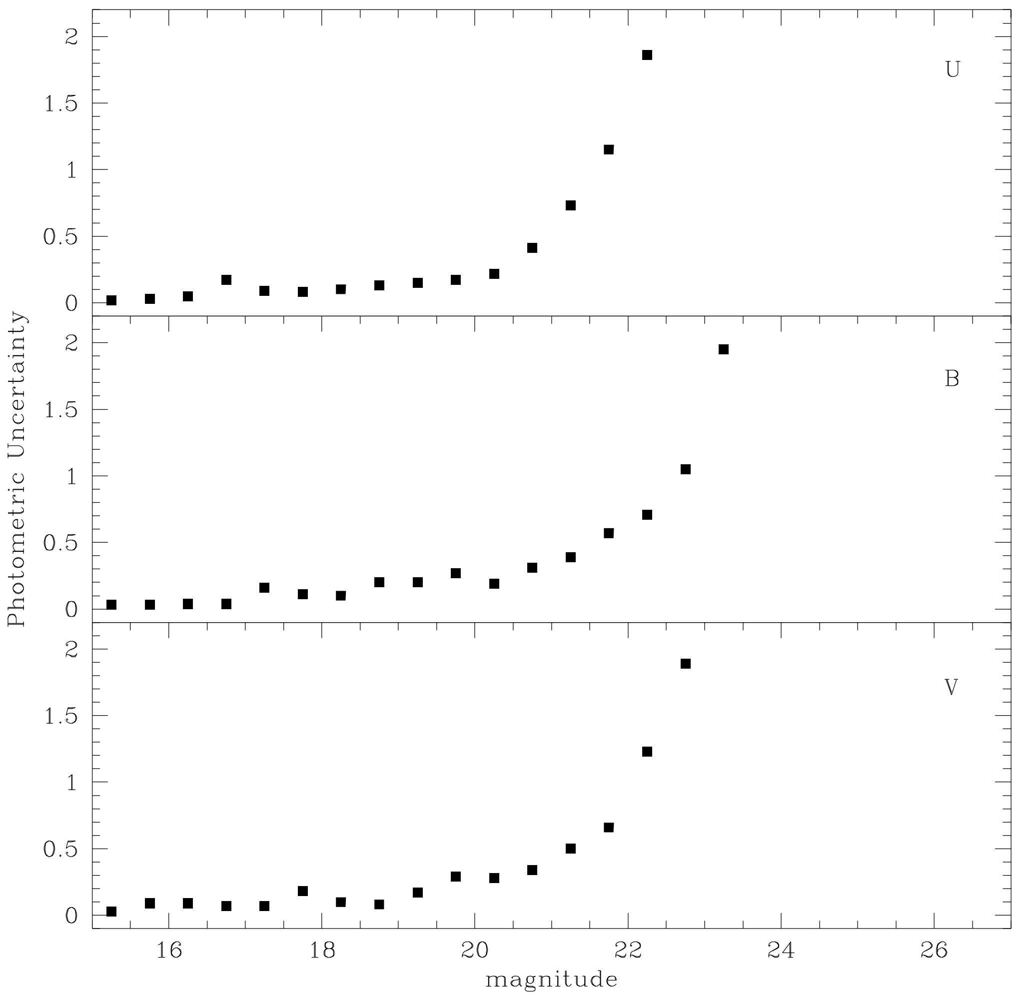

Figure 4.4: SE field photometry uncertainties, as determined by the differences in recovered and input magnitudes of artificial stars

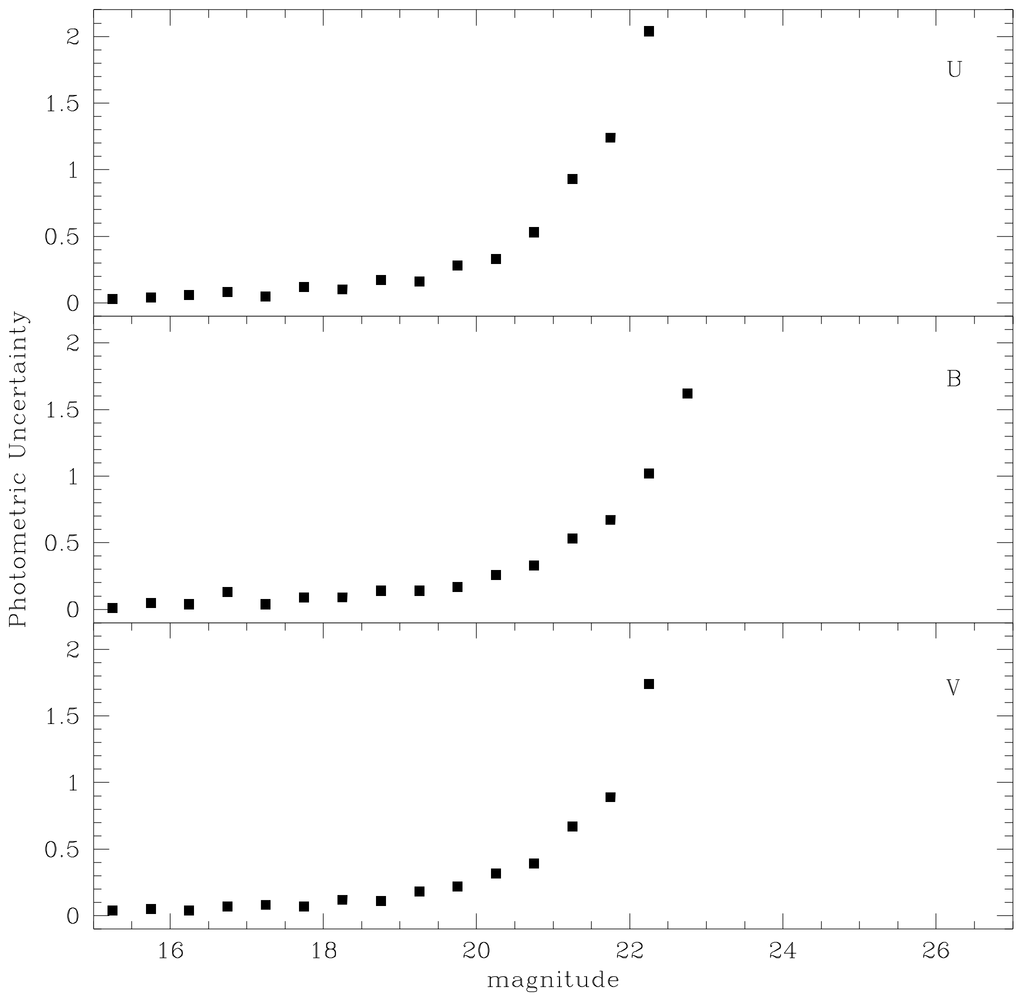

Figure 4.5: NW field photometry uncertainties, as determined by the differences in recovered and input magnitudes of artificial stars

Table 4.2: Star Formation History of the LMC

Age (Gyr)	SFR ($10^{-5} M_{\odot}$/yr)	[Fe/H]
0–1	40 ± 5	-0.71 ± 0.12
1–2.5	16 ± 14	-0.72 ± 0.10
2.5–5	3 ± 6	-0.88 ± 0.10
5–7	6 ± 9	-0.99 ± 0.10
7–9	10 ± 12	-1.10 ± 0.11
9–11	12 ± 9	-1.24 ± 0.13
11–12	111 ± 25	-1.45 ± 0.13

Padova isochrones (Girardi et al 1996, Fagotto et al 1994) were used. Monte Carlo simulations were also run to attempt to determine the uncertainties inherent in the fitting procedure itself, and the uncertainties from that were added in quadrature to determine the uncertainties. The solution was made using 22576 stars with B and V between 15.5 and 21.5. The determined extinction to the two fields was $A_V = 0.39 \pm 0.04$ and the distance modulus was $(m - M)_0 = 18.40 \pm 0.05$), which are discussed in the summary. As with WLM, there is no evidence for differential reddening in the fields studied. (The broad swath of stars running diagonally from the top of the CMD to the red edge is due to foreground stars.)

The star formation history is shown in Table 4.2 and Figure 4.6. Star formation rates are given assuming a Salpeter IMF with cutoffs at 120 and 0.1 $M_{\odot}$, which is consistent with the Holtzman et al (1997) results. An IMF error would simply have the result of changing the ratio of old to young stars, but would not qualitatively alter the two-burst structure observed.

A reconstructed CMD of the combined LMC fields is shown in Figure 4.7b, with the observed data shown in Figure 4.7a. The artificial star tests for this data set clearly do not account for all observational effects, as the main sequence sharpness

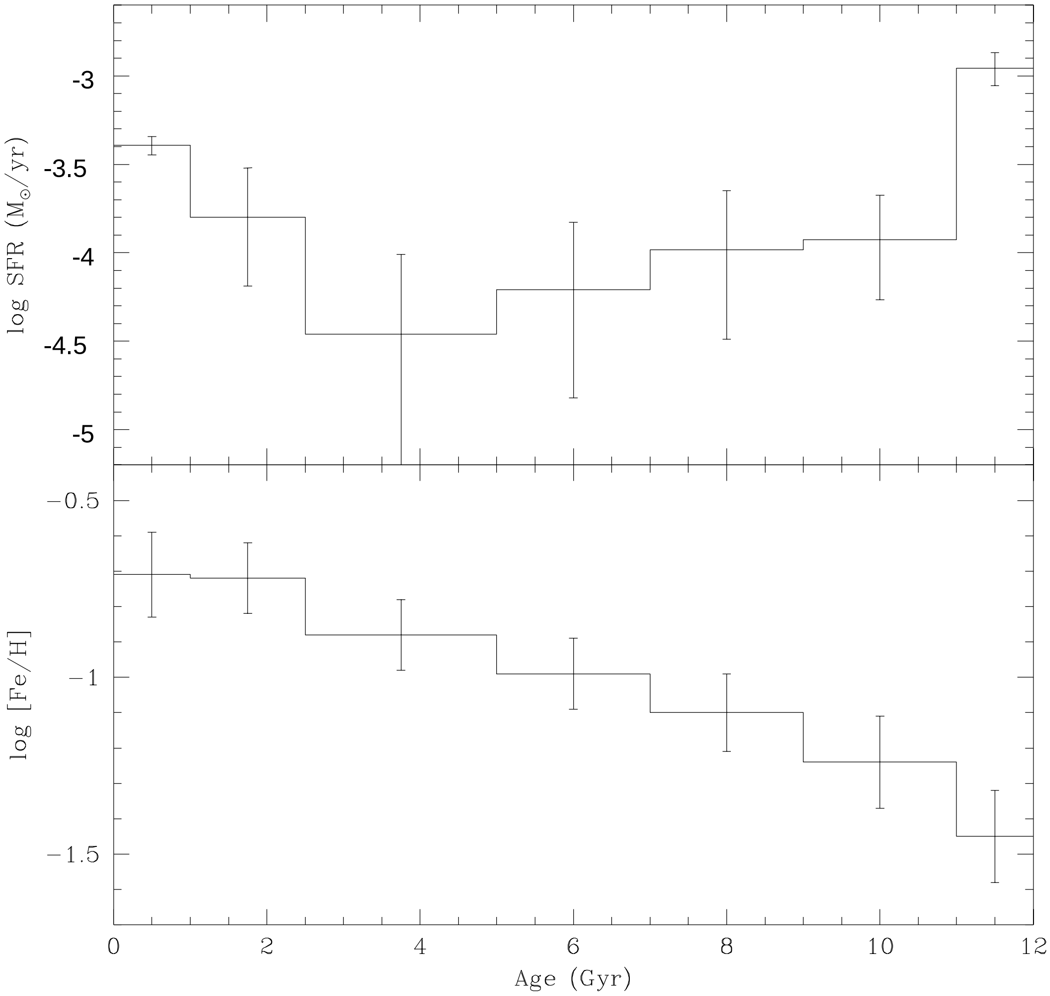

Figure 4.6: Star Formation History of the LMC

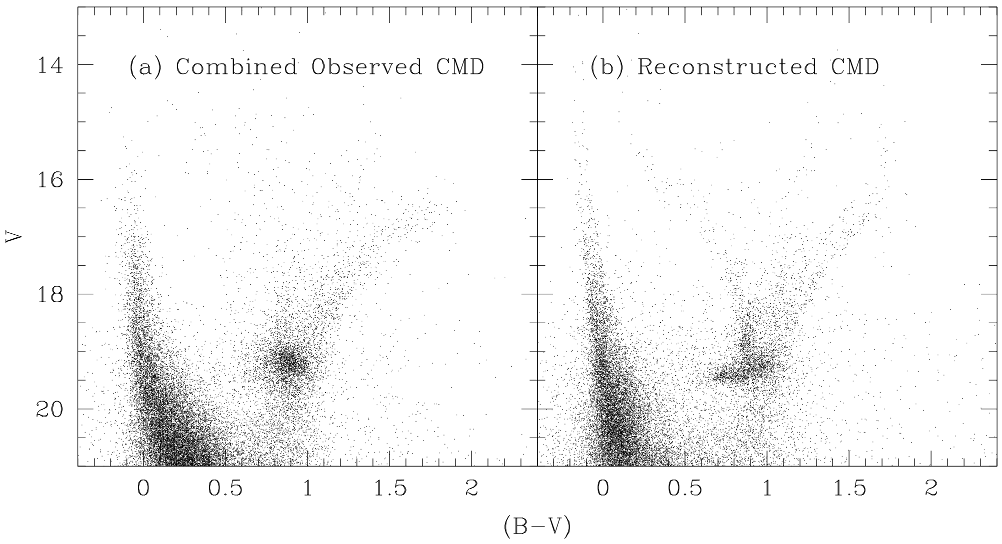

Figure 4.7: Reconstructed Color-Magnitude Diagram of the LMC

(the width is caused by an age spread), empty region between the main sequence and blue loops, and other effects occur in the reconstructed CMD. This could be a result of any combination of cosmic rays, PSF fitting errors (see above), bad pixels, etc.

A small red horizontal branch appears in the reconstructed data, indicating that either the time of initial star formation or the initial metallicity could be incorrect, or that the isochrones are incorrect. The RGB width and tip location is well-reproduced, although the RGB base is a little too far to the red in the reconstructed CMD.

On the main sequence, the observed data appears to cut off near V of 16, while the reconstructed main sequence extends well above that. This is a result of the chosen binning and assumption of constant star formation rate within each bin. In this case, the youngest bin was 0 to 200 Myr old, meaning that a main sequence turnoff between M_V of -2 and -3 is irreproducible with the chosen binning. The young stellar population will be dealt with more thoroughly (with higher resolution solutions) in the following section.

Because of the large amount of foreground contamination (for example the Sun, at 1 kpc, would fall squarely in the middle of the blue loop region), comparison between observed and reconstructed CMDs in the blue loop region will not be fruitful. Ideally, data would have been taken outside the LMC to sample foreground stars, but the data used for this chapter was taken as a background field for the Constellation III study (Dolphin & Hunter 1998).

A more detailed comparison is shown in Figures 4.8 and 4.9, which show the binned CMDs that were used for the solution (0.1 magnitude resolution in $B-V$ and 0.3 magnitude resolution in B for Figure 4.8; 0.05 $B-V$ and 0.15 B for Figure 4.9), as well as the residuals and the fit parameter values. Magnitude limits in the plots are $15.5 < B < 20.9$ and $-0.45 < V-I < 2.45$. The subtracted CMD is shown at twice the contrast level of the two CMDs (darker being undersubtracted and lighter oversubtracted), while the modified χ is shown on a scale from 0 to 3.2. As the diagrams show, the dominant feature in the CMD, by far, is the main sequence

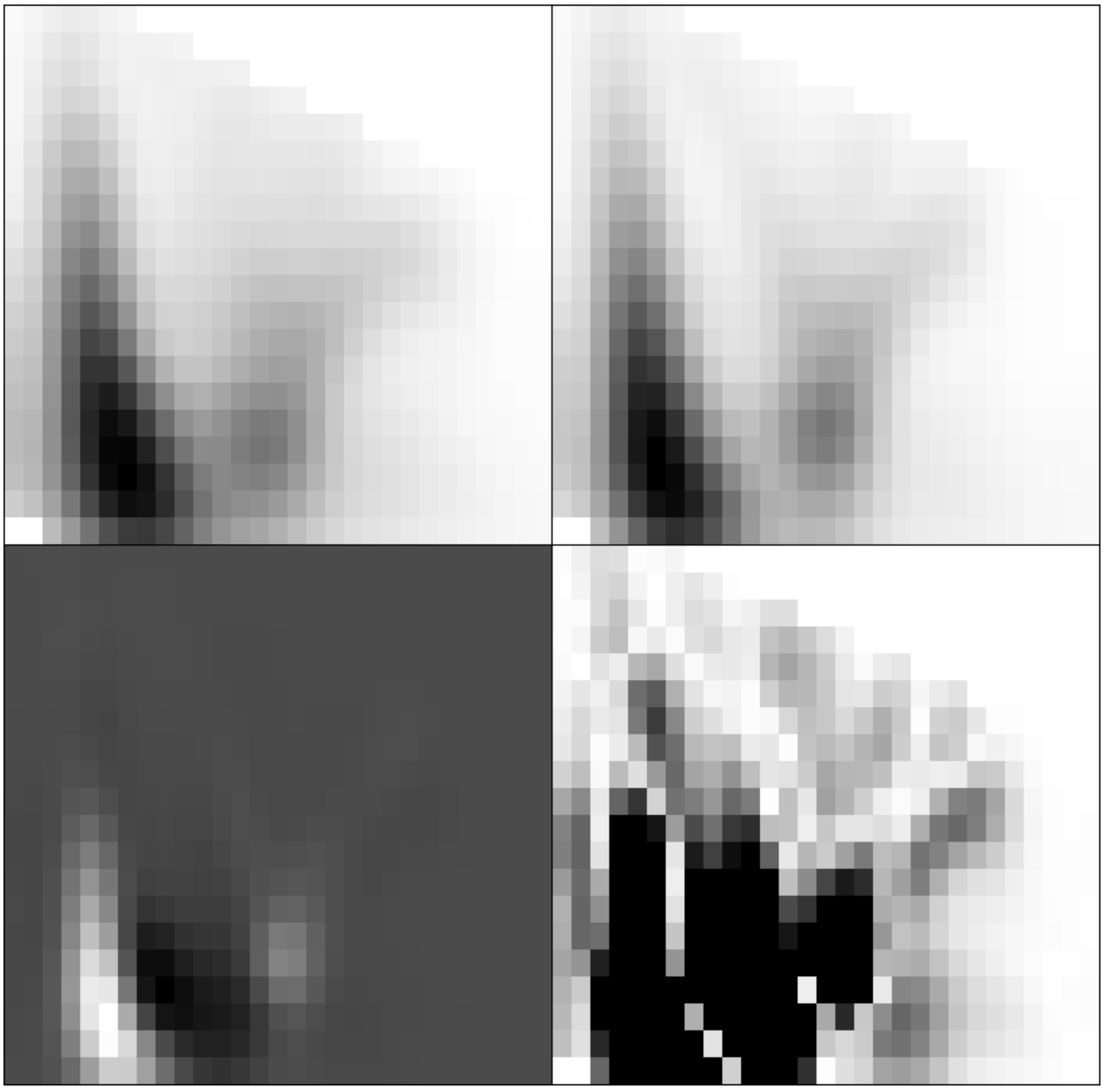

Figure 4.8: Comparison of Observed and Reconstructed CMDs. Upper left is the binned observed CMD; upper right is the binned reconstructed CMD. The lower left shows the subtracted diagram, while the lower right shows the modified χ values at each location. See text for explanation.

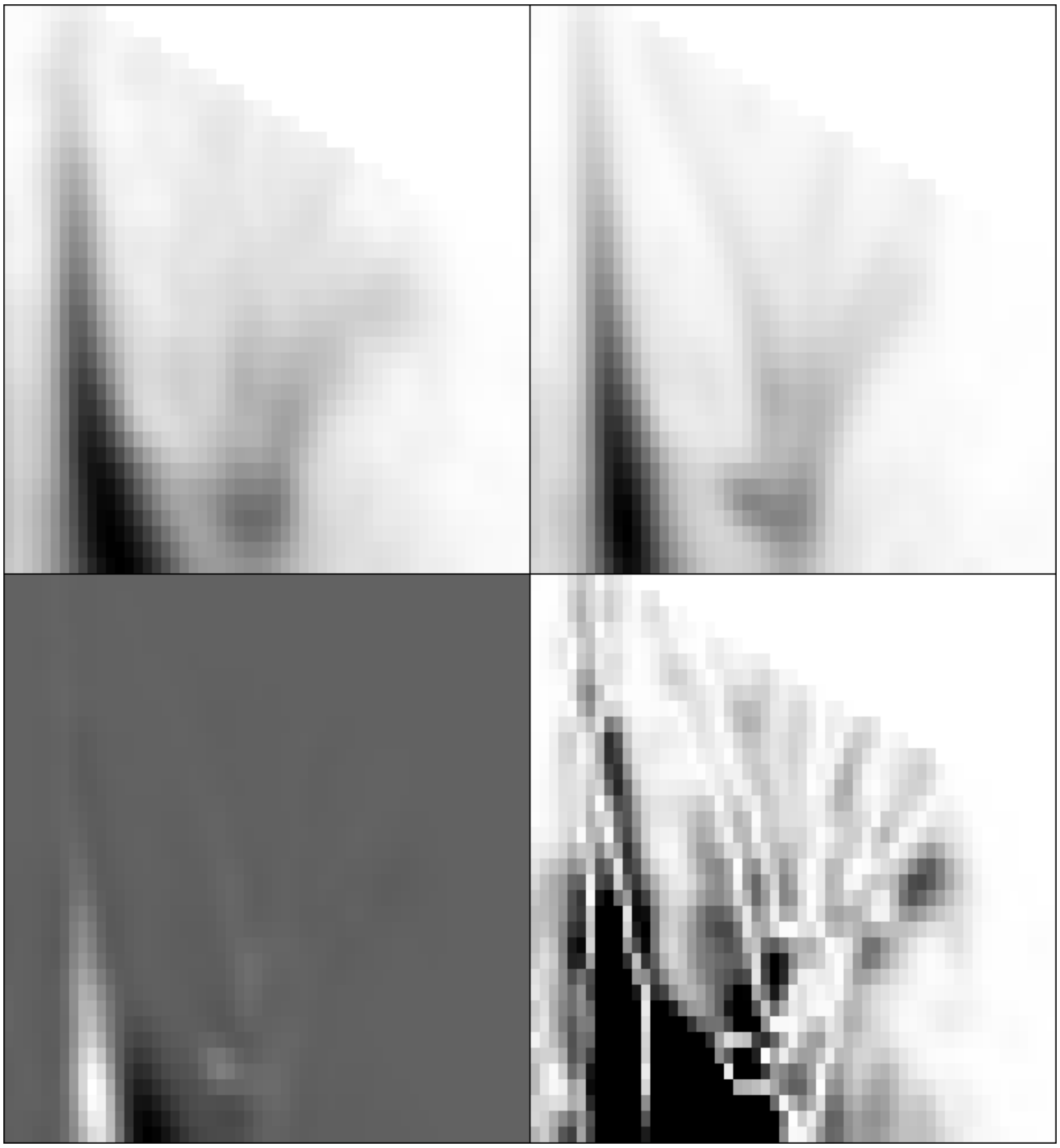

Figure 4.9: Comparison of Observed and Reconstructed CMDs. Same as Figure 4.8, but at twice the resolution.

(partly because, as with WLM, the red clump was given a lower weight).

The fitting program was able to handle the red giant branch extremely well in this case, with the main sequence causing the largest contribution to the fit parameter. This result is somewhat unsettling, as the main sequence should be the part of the diagram most easily fit properly (or at least the part where the models should be the most accurate). Figure 4.10 shows the original solution in the upper left, as well as three different attempts at a star formation history, all at the higher resolution. Since the problem appears to be the narrowness of the bottom of the observed main sequence, the first attempt, shown in the upper right, forced a higher star formation rate in the 1 to 2.5 Gyr time bins. This appears to have had little effect on fixing the main sequence, but caused the RGB base to be fit poorly. Another attempt is shown in the lower left, this time forcing the final metallicity to be the canonical LMC value of [Fe/H]=-0.4. This fit did improve the main sequence considerably, but did a very poor job in the red giant branch. The RGB itself was too red, and the reconstructed CMD had far too many stars near the base of the blue loops. To try to solve the red RGB problem, a third attempt, shown at lower right, was made with a lower reddening and higher distance, still using the higher current metallicity. This slightly lowered the fitting problems in the RGB base, but fit the upper main sequence very poorly and fit the lower main sequence nearly as poorly as the original solution.

Thus we are resigned to using the best fit from the star formation history procedure, despite its inability to model the lower main sequence. Perhaps part of this problem is that the artificial star tests did not fully account for all observational effects, which would cause reconstructed CMDs to show sharper features than the observed data. What is encouraging is that the red giant branch was fit very well, with only the few bins near the RGB tip having significant contributions to the fit parameter. The red clump region and blue loop base, not surprisingly, also were not fit terribly well, a result of the evolutionary models used.

The star formation in the LMC apparently began with a significant 1 Gyr burst,

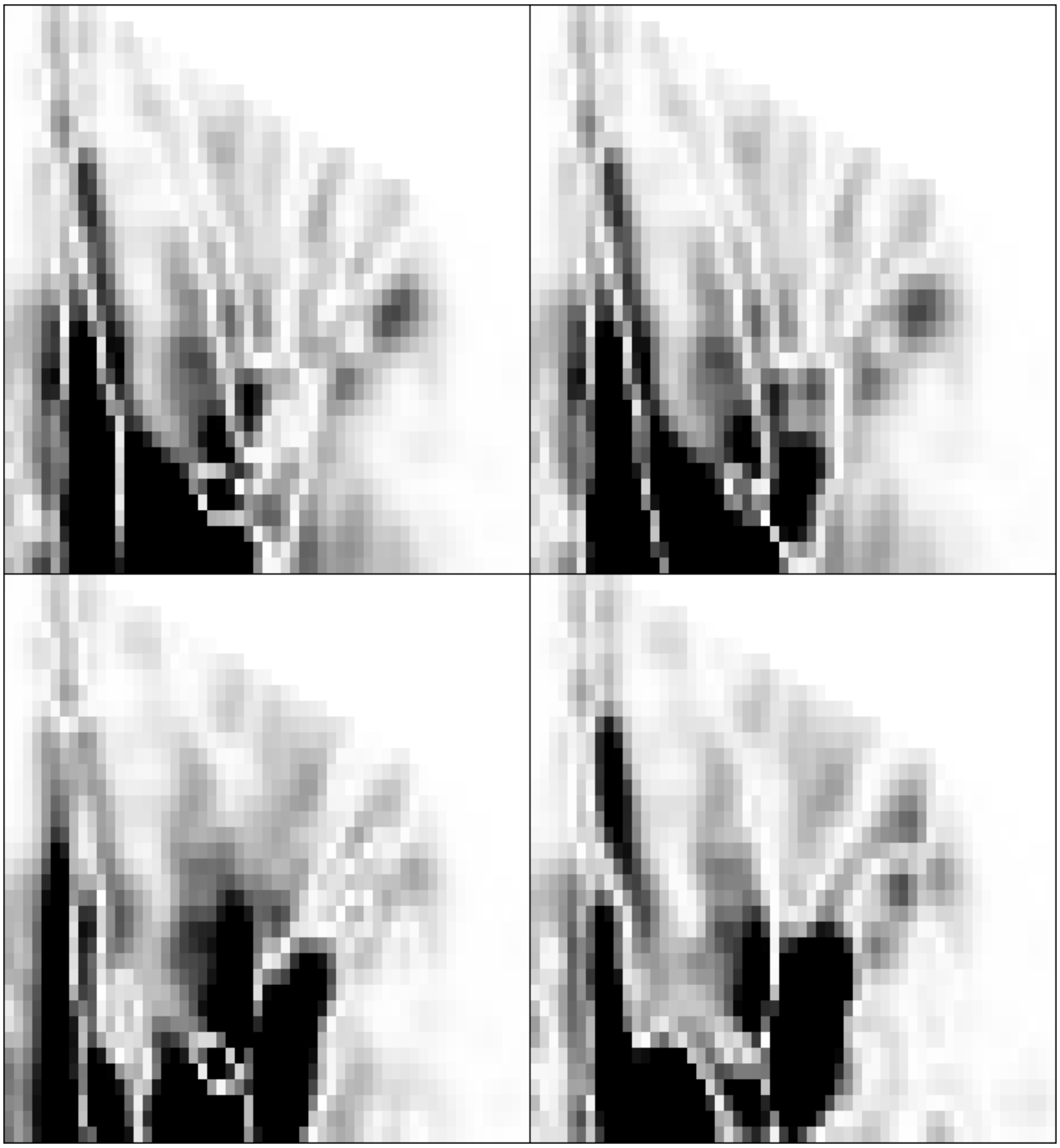

Figure 4.10: Fit parameter maps for four star formation history solutions. See text for explanations.

which accounted for about half of the LMC's total star formation (by mass of stars formed). After that, the star formation rate appears to have slowly declined from 11 Gyr ago until 1.5 or 2.5 Gyr ago, although the data is also consistent with a constant star formation rate of $10^{-4} M_{\odot}$/yr over that time. (The large error bars on the 1.5-2.5 Gyr bin mean that it could either be part of the low-level intermediate age population or the recent burst.) During more recent times, beginning between 1.5 and 2.5 Gyr ago, the LMC has undergone a second large burst of star formation (though at one-third the intensity of the initial burst), which is studied in greater detail in the following section. This history appears to support the recent HST-based results (Holtzman et al 1997, Stappers et al 1997, Geha et al 1998, and Olsen 1998), with the recent burst beginning no more than 2.5 Gyr ago.

The metallicity of the LMC's oldest stars is comparable to that of WLM, [Fe/H] = -1.45 $\pm$ 0.13. This is more metal-rich than Holtzman et al (1997)'s estimate of [Fe/H] = -1.7 for an old RGB, although they did not provide uncertainties, making it impossible to tell if the results are consistent or not. It has climbed very steadily since then, to its present value of -0.71 $\pm$ 0.12, consistent with the findings of Holtzman et al (1997). The difference between this metallicity and the -0.4 favored by Geha et al (1998) can be attributed to the higher extinction found here.

4.3.3 Recent Star Formation History

With more recent star formation, it is beneficial to study the two fields separately, as recent star formation in the two fields is likely to be quite different. Specifically, the fields are on either side of LMC Constellation III, a $\sim$1 kpc diameter superbubble where significant amounts of recent star formation have taken place (Dolphin & Hunter 1998). Although the Constellation III event happened very recently (in the past $\sim$20 Myr), it is possible that the recent star formation histories in these two fields have been quite different over a longer period.

Using the distance and extinction determined in the previous section, solutions for

Table 4.3: Recent Star Formation History of WLM Fields

Age (Gyr)	NW SFR ($10^{-5} M_\odot$/yr)	SE SFR ($10^{-5} M_\odot$/yr)
0.0−0.1	20 ± 5	38 ± 7
0.1−0.2	20 ± 5	47 ± 8
0.2−0.4	11 ± 3	17 ± 3
0.4−0.6	13 ± 4	14 ± 5
0.6−1.0	20 ± 5	20 ± 4
1.0−1.5	6 ± 12	6 ± 4
1.5−2.5	9 ± 6	5 ± 5
intermediate	4 ± 8	4 ± 6

the two fields were run that were much had higher resolution for recent star formation rates and events. The number of stars in each field was 10354 in NW and 12222 in SE. Resulting star formation rates are given in Table 4.3 and Figure 4.11.

Reconstructed CMDs of the two fields are shown in Figure 4.12, which can be compared with the observed data in Figure 4.1. Aside from the fitting problems mentioned above in relation to the combined CMD, the agreement is excellent. The split red giant branch is a result of the assumption that the metallicity is constant over each age bin. Thus there is a jump between [Fe/H] of -1.45 and -1.25 for the 11-12 and 9-11 Gyr old bins, when in reality the metallicity would have gradually increased. However, the total width of the red giant branch is well-reconstructed.

The star formation histories of the two fields are remarkably similar, and are consistent with each other at every point until 200 Myr ago, the 200 to 400 Myr bin beginning to show the divergence of the two. The NW field can have its star formation history characterized as increasing from the 2.5 to 11 Gyr average (the "intermediate" row of Table 4.3) to about $1.5 \times 10^{-4} M_\odot$/yr. The data is consistent with either a step function increase or a gradual increase, the large uncertainties between 1 and

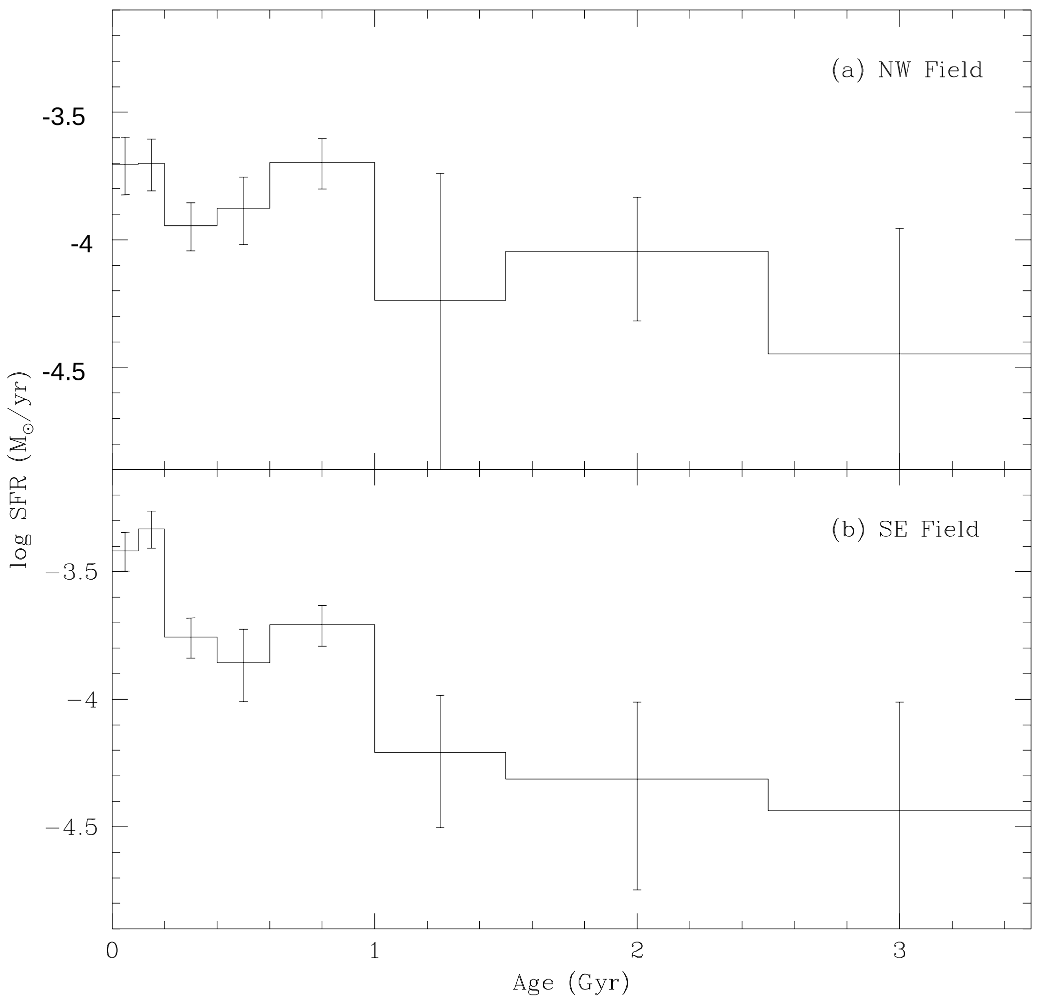

Figure 4.11: Recent Star Formation History of Two LMC Fields

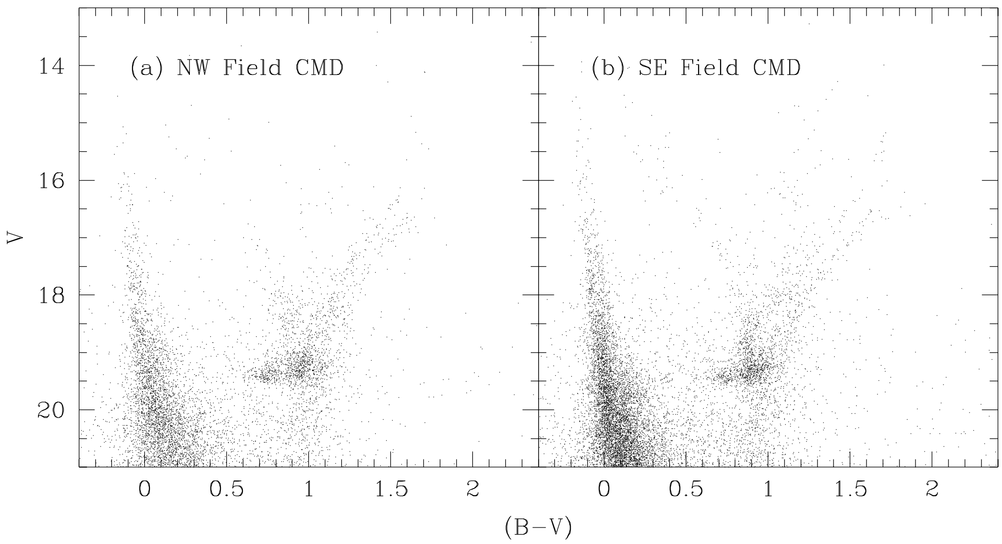

Figure 4.12: Separately Reconstructed Color-Magnitude Diagrams of Two LMC Fields

2.5 Gyr ago making it impossible to determine the age of the beginning of the recent burst. There is a possible dip in the star formation rate between 200 and 600 Myr ago, but the average for the last 200 Myr is back at the peak level. The SE field shows a similar star formation history, except for double the star formation rate over the past 200 Myr. (Of course, this difference is also apparent by a casual examination of the CMDs of the two fields, as the SE field has many more stars in the upper main sequence.)

With both fields having the same star formation rates for each bin until very recently, it follows that whatever conditions caused this recent outburst of star formation happened over a large scale. Given their physical separation of ~2 kpc, it seems unlikely that a single localized event could have triggered the large amount of star formation seen here. Also, with other studies of the LMC also finding a recent burst, there must have been some large change of environment that triggered an era of star formation throughout the galaxy.

4.4 Summary

Ground-based UBV photometry of two fields in the northern disk of the LMC has been presented. A distance modulus of 18.40 ± 0.05 and an extinction of 0.39 ± 0.04 have been calculated. The distance is smaller than the SN 1987A distance of 18.55 ± 0.05 (Panagia 1998), but consistent with the red clump distance of 18.36 ± 0.17 (Cole 1998). The extinction agrees well with the average extinction of $E(B-V) = 0.4$ found in the two fields by Dolphin & Hunter (1998). The LMC's oldest significant population appears to have a metallicity [Fe/H] of -1.45 ± 0.13, with an age of initial star formation of roughly 12 Gyr to account for the lack of a horizontal branch in the observed data. About half of the LMC's stars (by mass) formed within a Gyr of the beginning of the burst.

After this initial event, the star formation tapered off slowly, until a recent burst beginning between 1 and 2.5 Gyr ago. The metallicity has been constantly rising, and is currently at [Fe/H] = -0.71 $\pm$ 0.12, more metal-poor than the findings of Geha et al (1998) but consistent with the Holtzman et al (1997) findings. This recent burst seems to have increased in intensity in the SE field about 200 Myr ago, but the NW field is consistent with a constant star formation rate for the past 1 Gyr.

In summary:

- The distance modulus for this portion of the LMC was determined photometrically to be $(m - M)_0 = 18.40 \pm 0.05$. This is consistent with the SN 1987A distance of 18.55 $\pm$ 0.05 (Panagia 1998), and a red clump distance of 18.36 $\pm$ 0.17 (Cole 1998).

- The oldest significant star formation in the LMC occurred about 12 Gyr ago, with the initial burst lasting less than 1 Gyr. After low-level star formation until about 2 Gyr ago, a recent burst has rekindled the LMC. In agreement with the recent HST-based results, the burst appears to have begun in the 2-3 Gyr range (rather than the 3-5 Gyr range favored by previous ground-based studies).

- The metallicity of this part of the LMC has increased from an initial value of -1.45 $\pm$ 0.13 to a present value of -0.71 $\pm$ 0.12.

- The two fields studied show very similar star formation histories over the past 2.5 Gyr, but have deviated significantly from one another during the past 200 Myr. Given the separation of $\sim$2 kpc, the environmental change that caused this burst must have occurred over a very large, perhaps global scale in the LMC, with the recent ($<$200 Myr) star formation beginning to show regional differences.

Chapter 5

THE STAR FORMATION HISTORY OF LGS 3

5.1 Introduction

In contrast from the LMC, the dwarf spheroidal/irregular galaxy LGS 3 has had very little work done on it since its discovery in 1976 (Karachentseva 1976). As with WLM, its distance appears to be beyond M31, thus making ground-based work only sensitive to the tips of the main sequence and giant branches. The most complete work to date has been that of Lee (1995), Aparicio et al (1997), and Mould (1997), which have provided loose constraints on the distance, enrichment history, and star formation rates.

The distance modulus was determined by Lee (1995) to be $(m-M)_0 = 24.54 \pm 0.21$ using the RGB tip, while Aparicio et al (1997) found $(m-M)_0 = 24.43 \pm 0.04$ to be their best-fitting distance. The latter also found that an alternate distance modulus of $(m-M)_0 = 24.93 \pm 0.03$ was consistent with their data. The enrichment history is less understood, with two photometrically measured values being [Fe/H] $= -2.10 \pm 0.22$ (Lee 1995) for the average RGB star (whether young or old), and [Fe/H] between -1.0 and -1.45 (Aparicio et al 1997) for the youngest stars. Both of these values have very high uncertainty, however, and without spectroscopic data for HII regions (LGS 3 has none, Hodge & Miller 1995) or red giants, photometric abundances are all that is possible.

Finally is the issue of the star formation rates, which previous studies have not been sensitive enough to discern with much detail. Mould (1997) finds two most likely scenarios: either the stellar content arises from an initial burst in the distant past (over 10 Gyr ago) and a burst approximately 0.1 Gyr ago, or the star formation rate has been roughly constant for the past 10 Gyr at a level $\sim 10\%$ of that of the old stars. Either way, a large initial burst is expected from the Mould (1997) results. Aparicio et al (1997) find a very different result, namely that the star formation rate was constant from 15 Gyr ago until 1 Gyr ago, with only a very recent dropoff (by a factor of 3) in the star formation rates. (With their alternative larger distance, they find an exponentially decaying star formation rate instead). This discrepancy is something that should be addressable with the HST data presented here.

Goals for this study will be:

- Determining a distance and extinction for LGS 3, and comparing with previous photometric distance and extinction values.

- Dating the oldest stars in the galaxy and determining the star formation rates since that time, to compare with the recent results of Mould (1997) and Aparicio et al (1997).

- Determining the chemical enrichment history.

5.2 Data

5.2.1 Observations

Sixteen images of LGS 3, centered near the galaxy's edge, were taken on 9 January 1999 by the WFPC2 camera onboard Hubble Space Telescope. Images alternated 1100 and 1200 seconds, and were taken in the F555W and F814W filters in four dither positions. The total integration time was thus 9200 seconds in each filter. Cosmic ray cleaning and combining of the pairs of images in each dither position were done at STScI; a cleaned F555W image is shown in Figure 5.1.

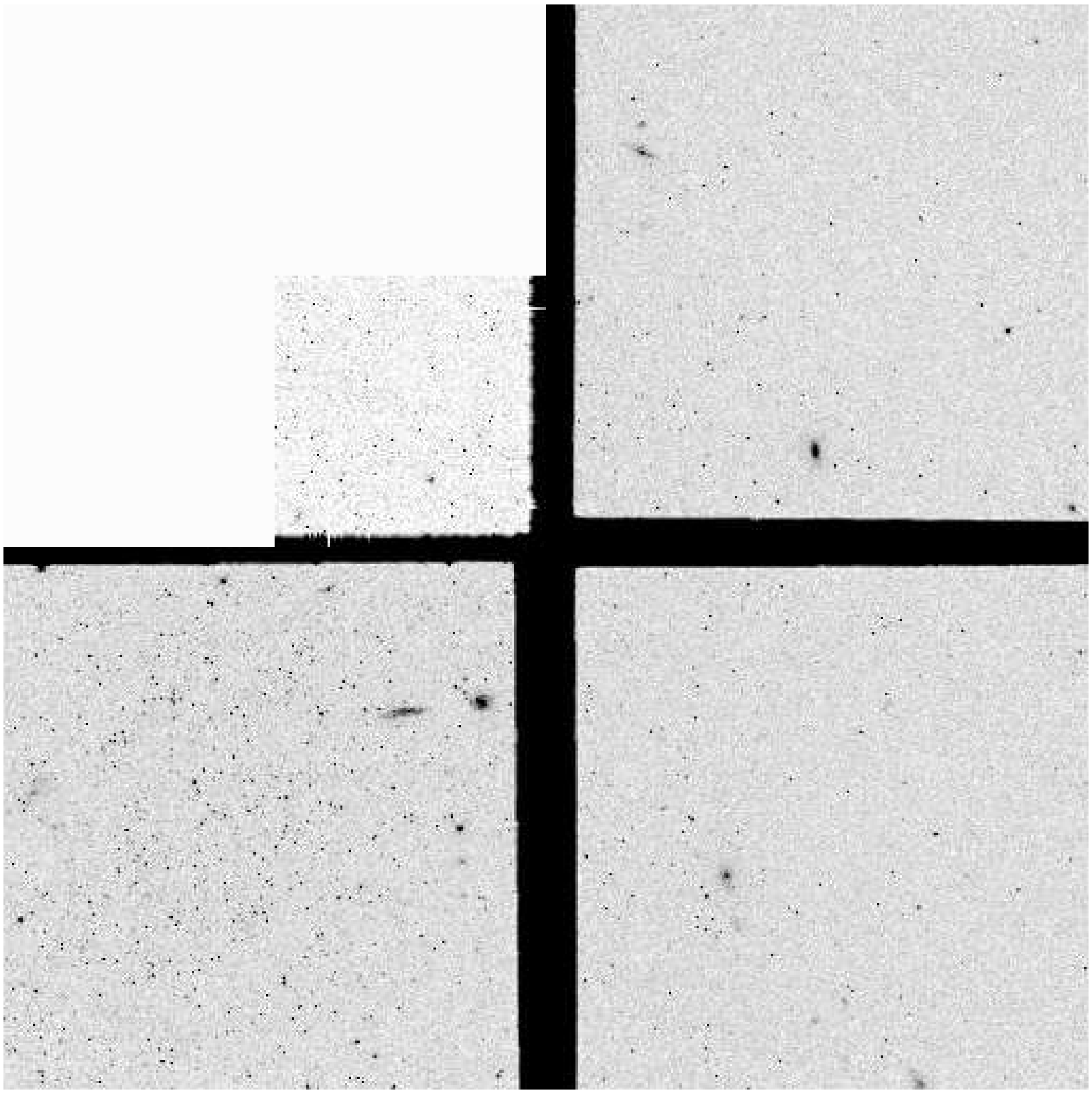

Figure 5.1: HST F555W Image of LGS 3

5.2.2 Reduction

Because the HSTPhot package accounts for the undersampled nature of the WFPC2 PSFs, it was unnecessary to use the dithering in the images. Instead, photometry was run on the four positions, with only stars that were found in at least two of the four images used in the final data set. The combined F555W and F814W data were then combined to make a single V, V-I CMD of LGS 3, which is shown in Figure 5.2a.

Artificial star tests were also run similarly to the WLM data in Chapter 3, but taking into account the requirement that a star had to be added four times and recovered at least two of the four times to be considered a recovered star. Again, the distribution of stars across the four chips and the color-magnitude diagram was selected so as to duplicate the observed stellar density and population.

5.3 Analysis

5.3.1 Era of Initial Star Formation

Due to the presence of the horizontal branch, we do not have the 12.5 Gyr upper limit on the era of initial star formation that was found in the previous chapters. Instead, a star formation history solution was made with various initial ages of star formation, using the modified χ^2 fit parameter described in Chapter 3. For all CMD analyses in this Chapter, the Padova isochrones (Girardi et al 1996, Fagotto et al 1994) were used. The solution was made using 1764 stars with V between 21 and 26 and I between 20.5 and 25.5.

A weighted average of the ages returning the best fits was selected, with this value of 14.5 ± 0.8 Gyr used for all star formation history work below. To determine the uncertainty caused by this assumption, solutions were also made with values of 14 and 15 Gyr, which produced qualitatively identical results to the results below.

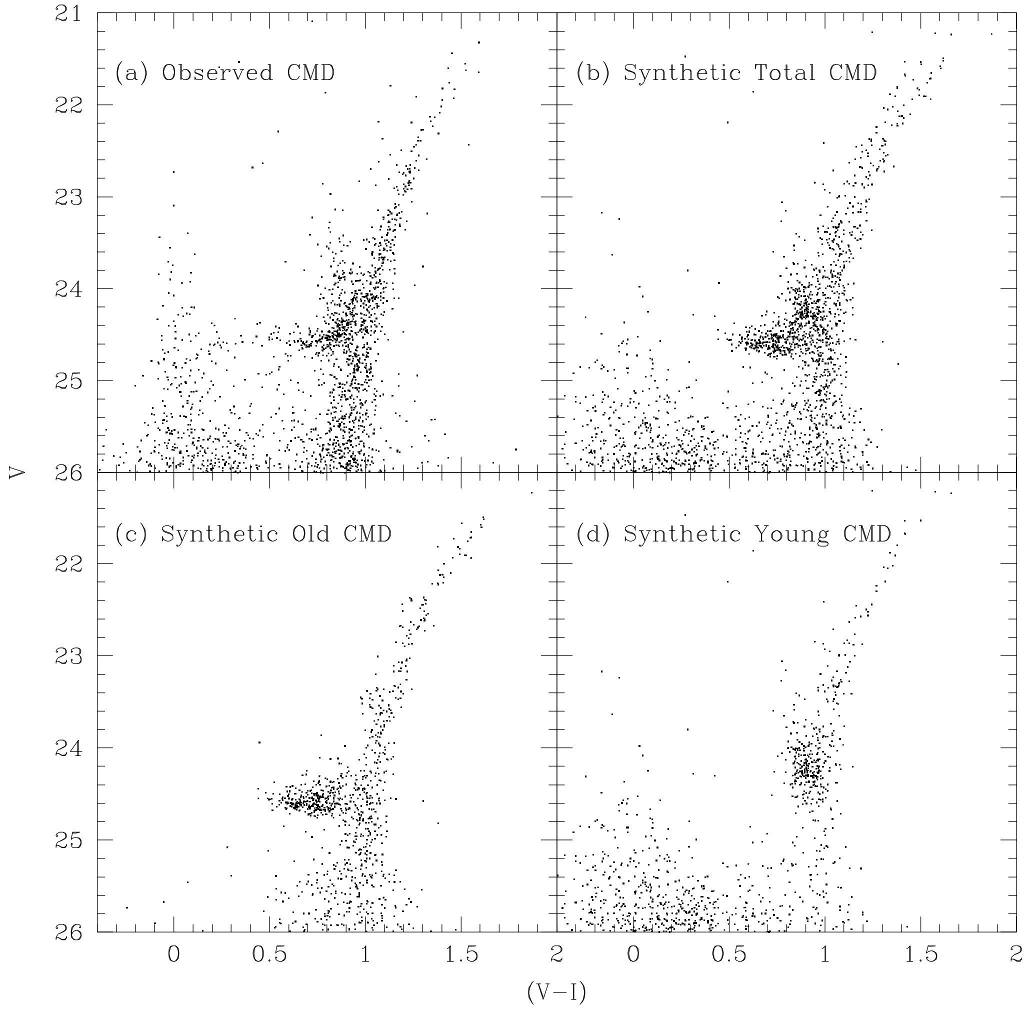

Figure 5.2: Color-Magnitude Diagrams of LGS 3. (a) shows the observed data; (b) shows the reconstructed CMD from the star formation history determined through analysis; (c) shows just the stars resulting from the old burst; (d) shows just the stars resulting from the young burst

5.3.2 Star Formation History and Enrichment

A large set of star formation history solutions was made, which allowed distance, extinction, enrichment history, and star formation rate to all vary. With all uncertainties except for those resulting from the choice of evolutionary models taken into account, the determined distance modulus to LGS 3 is $(m - M)_0 = 23.89 \pm 0.05$ and the extinction is $A_V = 0.05 \pm 0.05$ magnitudes. A horizontal branch distance, using the Chaboyer et al (1996) calibration, gives $(m - M)_0 = 23.82 \pm 0.14$, which is within uncertainties of the value calculated above. An RGB tip distance, using the Lee et al (1993) method, gives $(m - M)_0 = 24.01 \pm 0.14$, also consistent with the distance calculated using the CMD fitting procedure. These values all place LGS 3 much closer than previous distance estimates. The only explanation for this is that the photometry here is much better, and includes the horizontal branch, while the Lee (1995) and Aparicio et al (1997) results were based on only the upper RGB. The extinction is consistent with the estimates of 0.08 and 0.12 made be Lee (1995) and Aparicio et al (1997) based on the Burstein & Heiles (1984) maps. The global star formation history of LGS 3 is shown in Figure 5.3 and Table 5.1. Star formation rates are given assuming a Salpeter IMF with cutoffs at 120 and 0.1 $M_{\odot}$, which was used out of necessity because this data does not extend beyond the main sequence turnoff and therefore an IMF cannot be measured. An IMF error would simply have the result of changing the ratio of old to young stars, but would not qualitatively alter the two-burst structure observed.

A reconstructed CMD of the combined LGS 3 data is shown in Figure 5.2b, with Figures 5.2c and 5.2d showing the old and young stars, respectively. Aside from the expected errors in modeling the horizontal branch, the two significant differences between observed and reconstructed are in the height of the main sequence and the width of the red giant branch. Main sequence errors are generally caused by the choices of the time bins, and the assumption of constant star formation rate within a

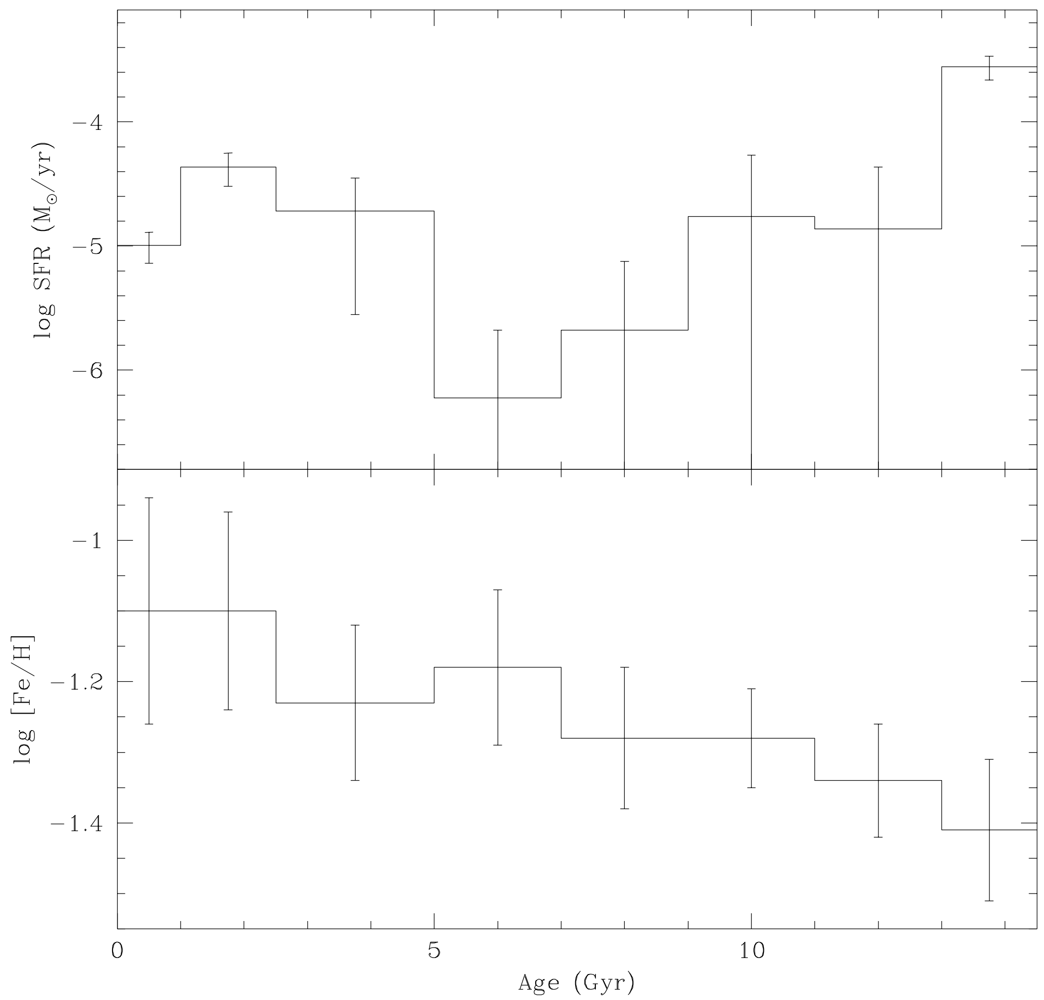

Figure 5.3: Star Formation History of LGS 3

Table 5.1: Star Formation History of LGS 3

Age (Gyr)	SFR ($\times 10^{-5} M_{\odot}$/yr)	[Fe/H]
0–1	1.0 ± 0.3	-1.10 ± 0.16
1–2.5	4.3 ± 1.3	-1.10 ± 0.14
2.5–5	1.9 ± 1.6	-1.23 ± 0.11
5–7	0.1 ± 0.2	-1.18 ± 0.11
7–9	0.2 ± 0.5	-1.28 ± 0.10
9–11	1.7 ± 3.7	-1.28 ± 0.07
11–13	1.4 ± 3.0	-1.34 ± 0.08
13–14.5	27.8 ± 6.0	-1.41 ± 0.10

time bin. There is also the issue of the blue horizontal branch, something not included in the models, which would add an extra population of "main sequence" stars at V of between 24.5 and 25, thus confusing the solution. The red giant branch width is mostly a result of the current metallicity being too large in the solution. The current metallicity, of course, is solved both from the RGB and the main sequence, so it is not surprising that minor inconsistencies would appear.

A more detailed comparison is shown in Figures 5.4 and 5.5, which show the binned CMDs that were used for the solution (0.1 magnitude resolution in $V-I$ and 0.3 magnitude resolution in V for Figure 5.4; 0.05 $V-I$ and 0.15 V for Figure 5.5), as well as the residuals and the fit parameter values. Magnitude limits in the plots are $22.0 < V < 26.5$ and $-0.45 < V-I < 2.5$. The subtracted CMD is shown at twice the contrast level of the two CMDs (darker being undersubtracted and lighter oversubtracted), while the modified χ is shown on a scale from 0 to 2.8. The dominant feature of the CMD is the RGB, with the main sequence and red clump also visible.

The first thing to note is that this CMD, overall, was fit extremely well. All bins were fit within 3 σ, while the WLM and LMC data sets in the previous chapters

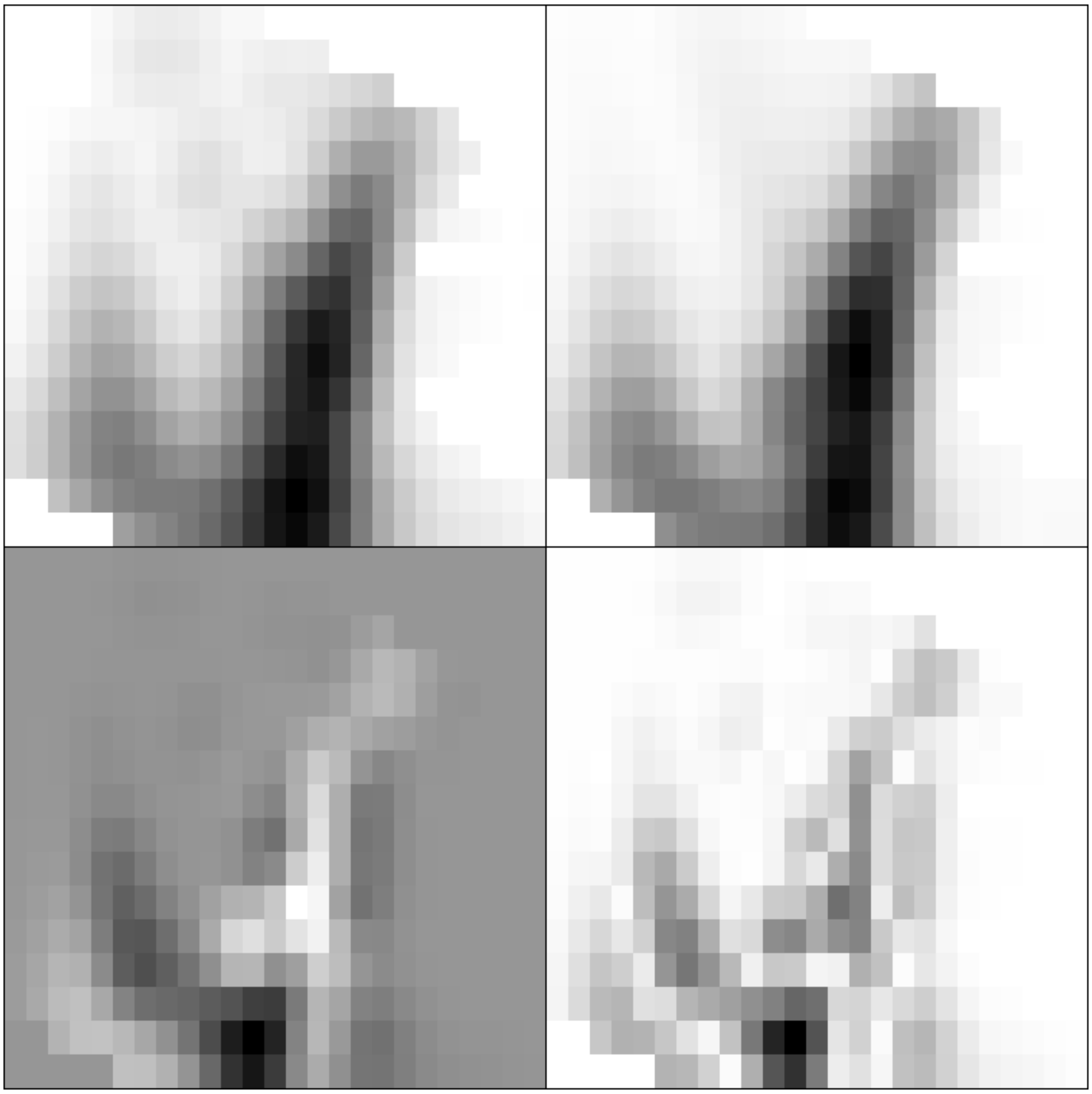

Figure 5.4: Comparison of Observed and Reconstructed CMDs. Upper left is the binned observed CMD; upper right is the binned reconstructed CMD. The lower left shows the subtracted diagram, while the lower right shows the modified χ values at each location. See text for explanation.

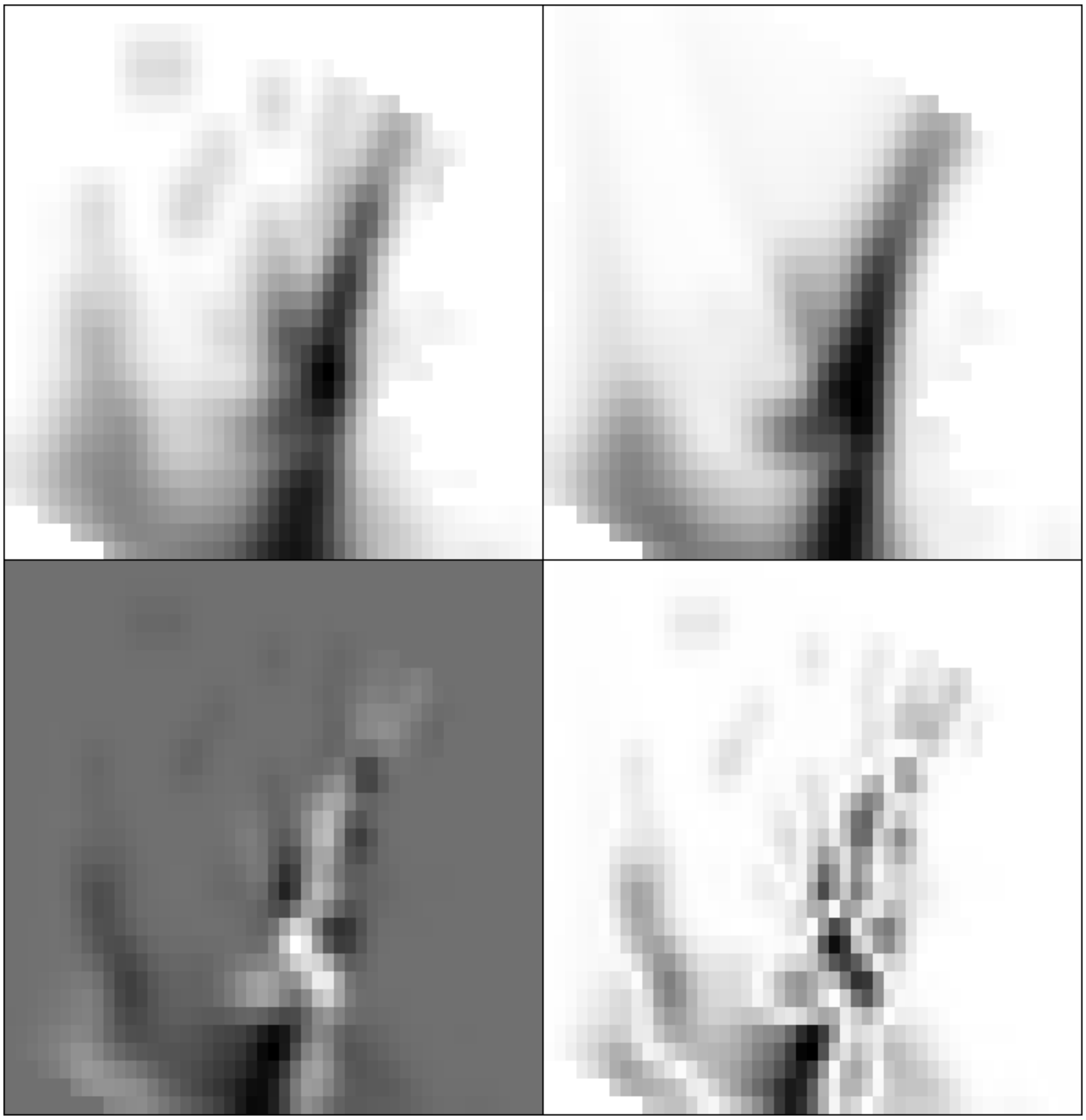

Figure 5.5: Comparison of Observed and Reconstructed CMDs. Same as Figure 5.4, but at twice the resolution.

each had many bins at the 3.2 σ maximum value. The worst-fit part of the CMD, in terms of fit parameter contributions, was the base of the red giant branch. The model CMDs were a little too red, causing an oversubtraction on the red side and a significant undersubtraction on the blue side. The only other significant fitting error came in the red horizontal branch region, where the poor reproduction of that phase in the synthetic CMDs caused oversubtraction.

The largest source of error in the main sequence fitting is from the synthetic CMD being bluer and shorter than the observed CMD, while the width of the synthetic RGB causes some oversubtraction on the blue side. Again, these fitting errors are all lower than those in the previous chapters, and this is by far the best-fit CMD.

LGS 3 appears to have had a rather different star formation history than WLM and the LMC. It began its star formation with a very strong burst, with 69% of the galaxy's total star formation (by mass) occurring during the first 1.5 Gyr and 79% during the first 5.5 Gyr. There was possibly star formation continuing as long as 5.5 Gyr after the beginning of star formation (the large uncertainties between 9 and 13 Gyr make a definitive statement impossibly), but there appears to have been no star formation in the galaxy between 5 and 9 Gyr ago. This is supported by the complete lack of AGB stars in the observed CMDs. Star formation has recently begun anew in the galaxy, and the recent activity will be studied in detail in the next section.

This star formation history is qualitatively similar to that given by Mould (1997), who suggested an old (>10 Gyr) burst and a very young ($\sim$ 100 Myr burst), while very different from that given by Aparicio et al (1997), who suggested a relatively constant star formation rate, with a significant decrease in the last 1 Gyr. A reconstructed CMD using the star formation history given by Aparicio et al (1997) is shown in Figure 5.6, where it is compared with the observations and the reconstructed CMD from Figure 5.2. There are a number of significant differences that should be pointed out. First is the distance error, mentioned above, which causes all features of Figure 5.6c to appear 0.75 magnitudes fainter than observed. Even putting that aside, the constant

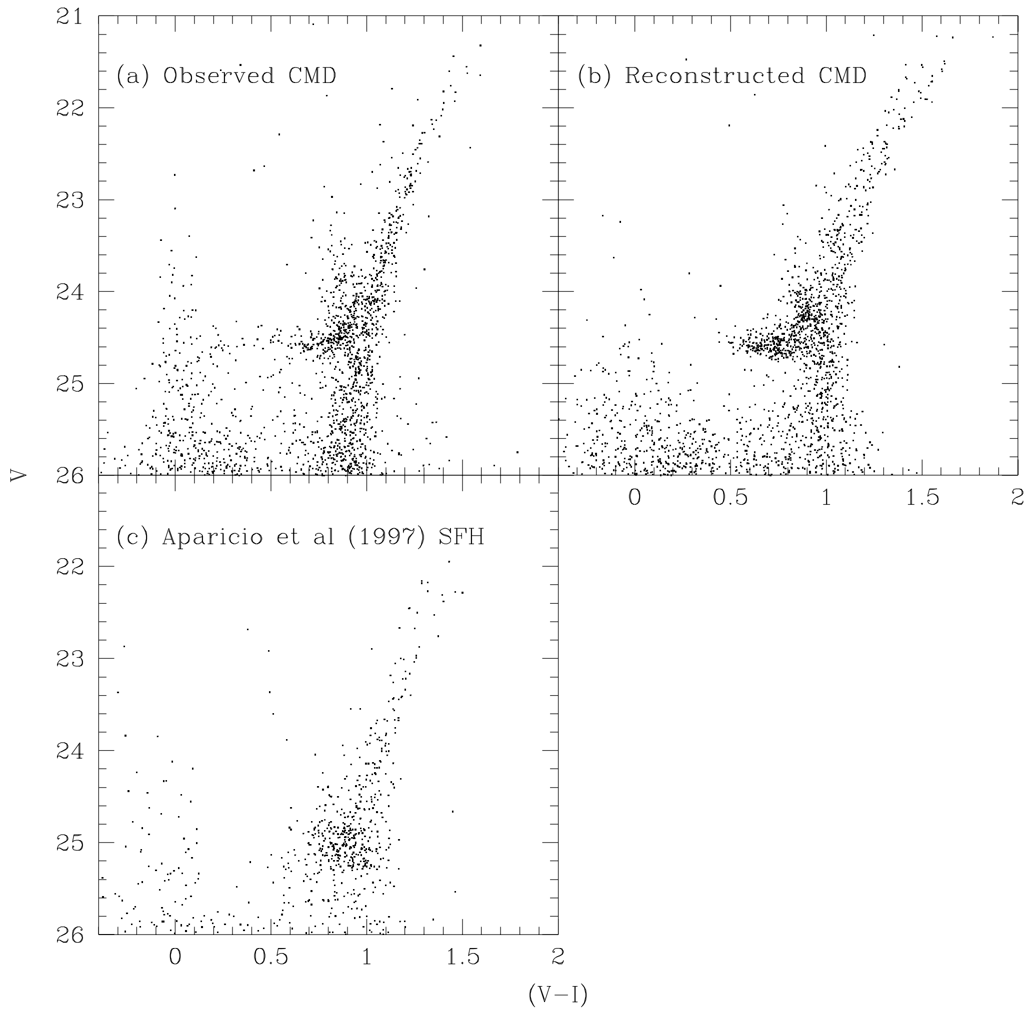

Figure 5.6: Observed CMD compared with reconstructed CMDs with two different star formation histories. (b) The reconstructed CMD from the star formation history determined here. (c) The reconstructed CMD based on the Aparicio et al (1997) star formation history.

star formation rate for the old stars produces a significant red clump population and a very weak horizontal branch, something not seen in the observed data. Thus the solution with more very old stars and fewer intermediate age stars appears to be better. Interestingly, the RGB is in roughly the right position, as the error in distance (which would make their RGB redder at a given magnitude) was offset by an assumption of very low metallicity. (Although to their credit, the similarities between the CMDs are remarkable considering that they had only the upper RGB to base their conclusions on!)

The metallicity of the stars formed in LGS 3's initial large star formation episode have an average metallicity of [Fe/H] = -1.41 ± 0.10, which is significantly higher than Lee's (1995) value of -2.10 ± 0.22. This finding is consistent with the horizontal branch morphology, as compared with Lee et al (1994). As noted above, the previous estimates of metallicity were made from an incorrect distance, which causes the very large discrepancy seen here. The recent burst is consistent with a constant metallicity of -1.16 ± 0.08, which is within the $-1.0 to -1.45$ range given by Aparicio et al (1997) for the metallicity of the young stars. This value should be expected to be closer to the previous measurements than the old star metallicity, as the upper main sequence is vertical and thus not as sensitive to errors in distance.

5.3.3 Recent Star Formation History

In order to study the recent star formation, it is useful to separate the main body of the galaxy, which is largely constrained to the PC and WF2 chips, from the halo, in order to search for star formation history differences similar to those found in WLM. CMDs of the two regions are shown in Figure 5.7. The number of stars in each region was 1298 in the galaxy and 466 in the halo.

Using the distance and extinction determined in the previous section, solutions that had much higher resolution for recent star formation rates and events were run for the two regions. Resulting star formation rates are given in Table 5.2 and Figure

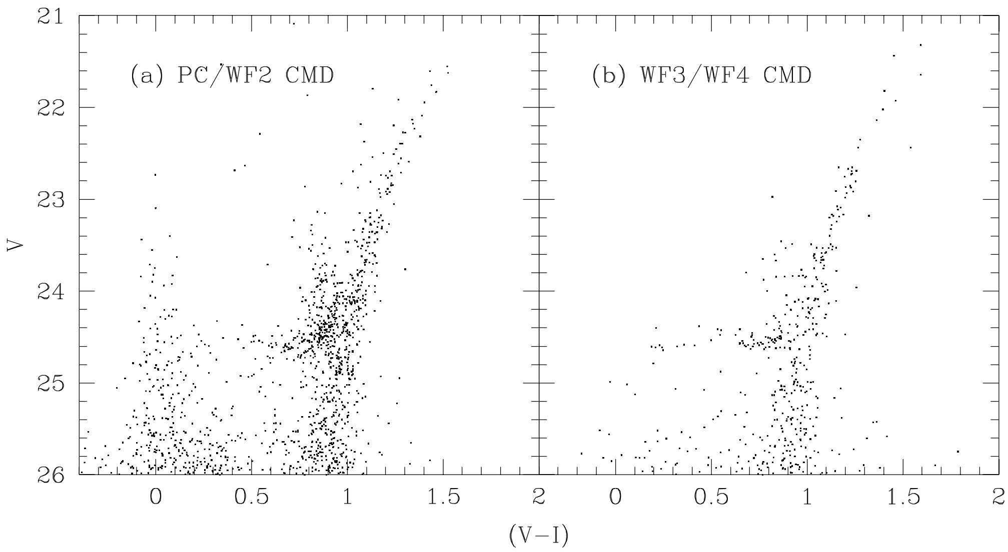

Figure 5.7: Color-Magnitude Diagrams of LGS 3. (a) shows the combined PC/WF2 data, corresponding to the galaxy's main body; (b) shows the combined WF3/WF4 data, corresponding to the galaxy's halo.

Table 5.2: Recent Star Formation History of the LGS 3 Regions

Age (Gyr)	Galaxy ($10^{-5}M_{\odot}$/yr)	Halo ($10^{-5}M_{\odot}$/yr)
0.0–0.2	0.0 ± 0.1	0.00 ± 0.03
0.2–0.6	0.6 ± 0.2	0.00 ± 0.04
0.6–1.0	1.8 ± 0.7	0.2 ± 0.2
1.0–1.5	0.0 ± 1.2	0.0 ± 0.3
1.5–2.5	5.2 ± 2.0	0.7 ± 0.9
2.5–3.5	2.9 ± 4.4	2.6 ± 2.4

5.8.

Reconstructed CMDs of the two fields are shown in Figure 5.9, which can be compared with the observed data in Figure 5.7. Aside from the fitting problems mentioned above in relation to the combined CMD, the agreement is excellent. The galaxy field is reproduced extremely well, although the tip of the main sequence still is too low; splitting the 200-600 Myr bin in half may have solved that problem. The red clump and HB are both well-reproduced.

The robustness of the modified χ^2 fit parameter is evident here, as the solution was not thrown off much by the blue horizontal branch stars in Figure 5.7b. A previous version of this solution, using a plain χ^2, found a star formation rate of $1.5 \pm 1.0 \times 10^{-5} M_{\odot}$/yr between 200 and 600 Myr ago in the halo. Here, the star formation rate is undetected, with a 1σ upper limit of $3 \times 10^{-7} M_{\odot}$/yr. The fit still was forced to find a small number of stars in the main sequence below the HB, (between V of 25.5 and 26.5), but the number is quite small and the error bars on the star formation rate are consistent with no star formation during that period.

The first thing to note is that the halo star formation rates are consistent or nearly consistent with no star formation during the last 3.5 Gyr. Figure 5.7b shows no strong evidence of any main sequence stars, so we will conclude that the region shows little

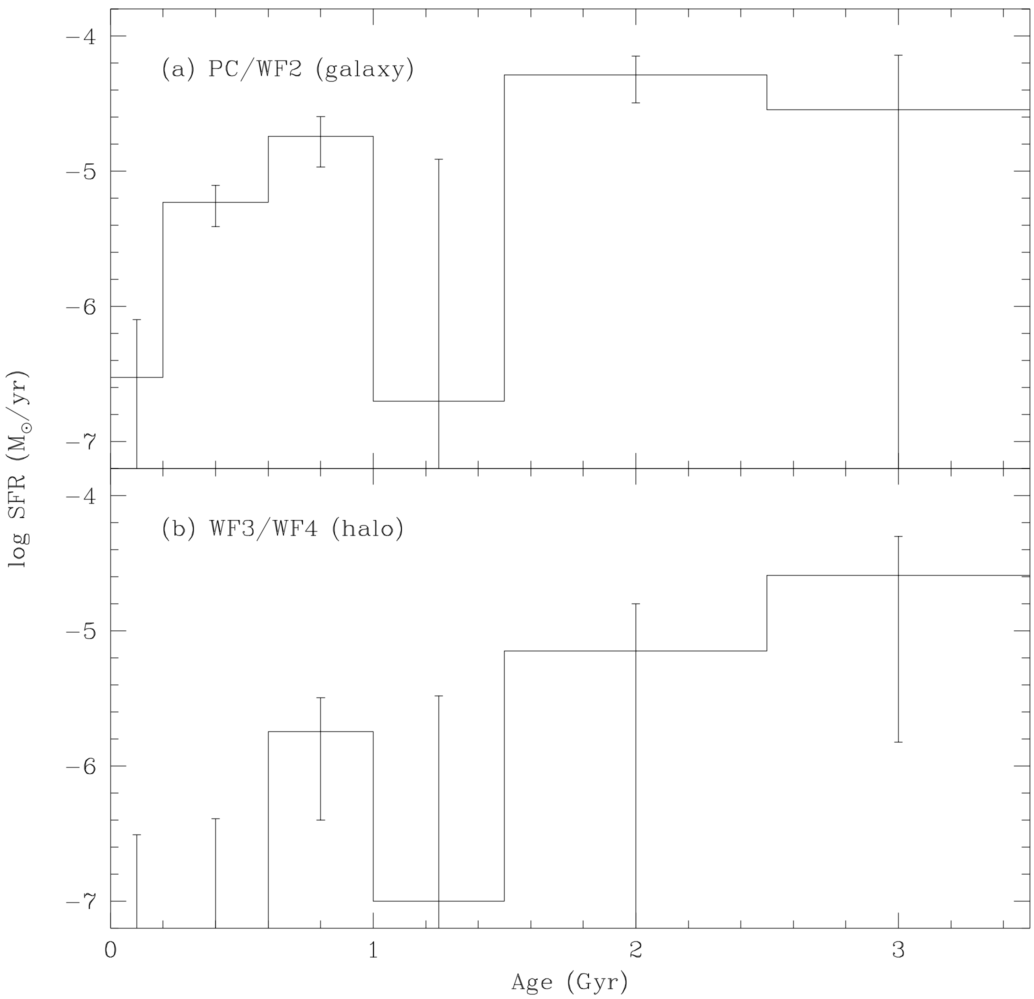

Figure 5.8: Recent Star Formation History of the LGS 3 Regions. (a) shows the combined PC/WF2 star formation history, corresponding to the galaxy's main body; (b) shows the combined WF3/WF4 star formation history, corresponding to the galaxy's halo.

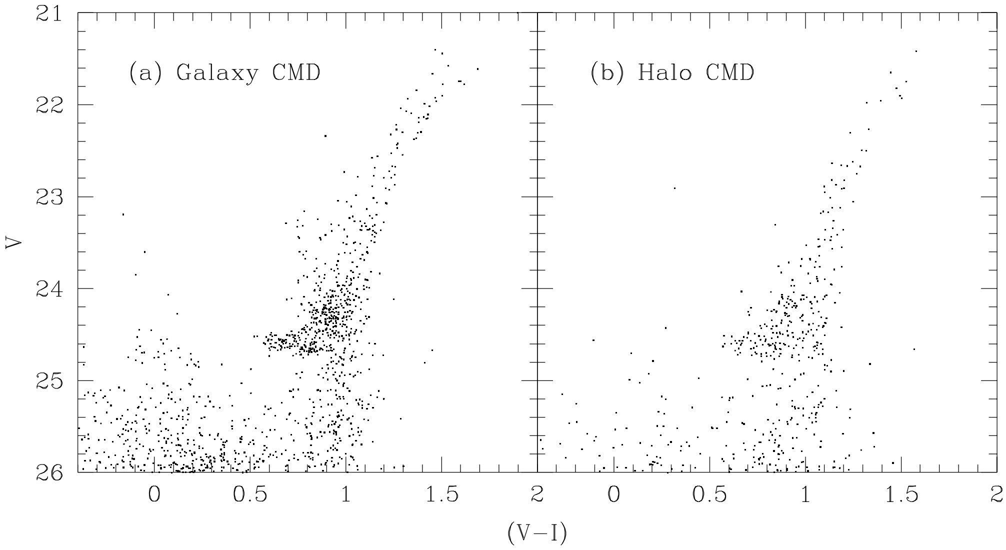

Figure 5.9: Separately Reconstructed Color-Magnitude Diagrams of Two LGS 3 Regions

or no star formation during the recent burst, and the remainder of this section will focus entirely on the galaxy body, the PC and WF2 frames.

The data is not able to determine the beginning of the recent burst. Since stars formed older than 3.5 Gyr ago would no longer be visible on the observed main sequence, we cannot put an upper limit on the age of the recent burst with this data. The small number of AGB and red clump stars indicate that there was little star formation during intermediate ages, but when exactly the recent burst began is in doubt. There is a significant star formation rate in the body from 1.5 to 2.5 Gyr ago, implying that the recent burst began at least 2.5 Gyr ago, but the large uncertainties in the 2.5 to 3.5 Gyr bin make it impossible to draw a strong conclusion.

The past 200 Myr have no detectable star formation, which is consistent with the Hodge & Miller (1995) non-detection of HII regions in the galaxy. Before that, the structure of the burst is impossible to determine with much detail. The drop between 1.0 and 1.5 Gyr ago is insignificant, as both the 0.6 to 1.0 and 1.0 to 1.5 Gyr bins are consistent with a constant star formation rate of $1.2 \times 10^{-5} M_{\odot}/\mathrm{yr}$, a value significantly higher than the 0.2 to 0.6 Gyr star formation rate and significantly lower than the 1.5 to 2.5 Gyr star formation rate. Thus the burst seems to have begun strong and weakened, ending between 200 and 600 Myr ago.

5.4 Summary

HST photometry of the LGS 3 galaxy was presented. An age of initial star formation of 14.5 ± 0.8 Gyr was calculated from CMD fitting, as well as a distance modulus of 23.89 ± 0.05 and extinction $A_V = 0.05 \pm 0.05$. This distance is much closer than RGB tip measurements by Lee (1995) and Aparicio et al (1997), a result of the deeper data provided by HST.

LGS 3's first significant star formation appears to have taken a relatively short amount of time (most stars forming in the first 1.5 Gyr), and was at a metallicity of [Fe/H] = -1.41 ± 0.10. The first event may have continued until as recently as 9 Gyr ago, but there is no detection of star formation between 5 and 9 Gyr ago. Star formation resumed between 2.5 and 5 Gyr ago, in a burst localized to the galaxy's main body. After starting strong and gradually weakening, this recent burst finished between 200 and 600 Myr ago and a metallicity of [Fe/H] = -1.10 ± 0.15. The result that the galaxy is back to its quiescent state is consistent with the lack of bright main sequence stars and the lack of HII regions (Hodge & Miller 1995).

In summary:

- The distance modulus for LGS 3 was calculated to be 23.89 ± 0.05, much closer than previous measurements, and the extinction was calculated to be $A_V = 0.05 \pm 0.05$.

- The oldest stars have an age of 14.5 ± 0.8 Gyr, with star formation occurring in two bursts, a recent burst that mostly died out between 200 and 600 Myr ago and an initial burst that began the galaxy's star formation. This is qualitatively similar to the results of Mould (1997), while very different from those of Aparicio et al (1997).

- The bulk of the star formation began with a fairly high metallicity of [Fe/H] = -1.41 ± 0.10, which was increased to its present value of [Fe/H] = -1.10 ± 0.15 by the initial burst. These values are consistent with the Aparicio et al (1997) estimate of the current metallicity, but not with the Lee (1995) estimate of -2.10 ± 0.22, because of an incorrect distance used in earlier work.

Chapter 6

SUMMARY

A method for the study of star formation histories has been outlined, tested with synthetic and "known" data sets, and finally applied to observations of three nearby dwarf galaxies: WLM, the LMC, and LGS 3.

6.1 Star Formation History Method

6.1.1 Method

The core of the method for studying star formation histories is based on two procedures - producing large numbers of synthetic color-magnitude diagrams, and determining the synthetic CMD that best fits the observed data. The first step is done by interpolating published theoretical isochrones to the desired metallicities and ages and applying artificial star results to the interpolated data. Since a CMD of a composite population of stars is simply a linear combination of the CMDs of each age and metallicity present, all that is needed to generate any star formation history is therefore a library of CMDs containing a CMD with each age and metallicity.

In order to make a comparison with the observations, both the observed data and synthetic CMDs are binned and smoothed. A fit using a goodness-of-fit parameter (such as χ^2) is then done in order to determine the combination of synthetic CMDs that best fits the data, and thus determine the past star formation rates. Since this fit can only be done for a single distance, reddening, and enrichment history, many fits may be necessary with different values of those parameters to determine the galaxy's star formation history. In addition, this allows a photometric fit to the galaxy's distance and reddening, something generally input rather than fit by other star formation history calculations.

6.1.2 A Recipe for SFH Work

The following recipe can be used to determine the star formation history and other parameters of a galaxy, cluster, or part of a galaxy. As this is intended to be a guide, it will be in a more conversational tone than other parts of this dissertation.

- Obtain photometry and artificial star data for the fields in question. The photometry should be done in as automatic a way as possible, so that the artificial star results provide an accurate assessment of the photometric errors. For example, manually matching stars in a crowded cluster, while desirable for getting the best photometry, would also require manually matching artificial stars during the artificial star tests and is thus actually detrimental to this calculation.

  The artificial stars must be added in such a way that their positions are related to the distribution of stars in the field. If your field has large variations in crowding (such as with one or more large clusters), you should probably base the star positions on the number of counts on the frame rather than the number of observed stars, as using the number of observed stars would put too few artificial stars in the denser regions. The CMD of the artificial stars must be such that there are significantly more recovered stars in each region of the CMD than observed stars, thus giving the artificial stars a minor effect on the overall statistics. A good rule of thumb would be that there should be four times as many recovered stars as observed stars in each part of the CMD, thus causing the artificial stars to contribute 33% of the uncertainty. With a fast enough computer, more artificial stars would be beneficial, but keep in mind that in addition to the speed of running the artificial star tests, the time required for model generation (which is the limiting factor in the speed of solutions) is proportional to the number of artificial stars.

- Predetermine as many of the input parameters as possible (distance, extinction, differential reddening, and metal enrichment history). The more of these that can be pinned down before running the solutions, the faster the solutions will run. If the values are not known sufficiently well, though, it is better to solve for them with the solution than to make guesses based on previous results. Whether to adopt literature values or make it part of the solution depends upon the uncertainties in the literature and how deep and complete your data are. For example, in all data presented in this dissertation, the horizontal branch or red clump was visible, which produced photometric distances with uncertainties less than 0.1 magnitudes, comparable or better than previous measurements. Aside from the WLM data, for which a distance and extinction was available from the globular cluster work, only the differential reddening was predetermined. Solving for differential reddening can increase the time required for model computation by a factor of 100 or more, so it should be generally determined beforehand, with other quantities that do not affect the time required for model generation determined during the fitting.

- Determine the age of the onset of star formation. While this might seem like it should be part of the general fit, it should be remembered that even a single-age burst will appear to be spread out when the star formation history is reconstructed. This is because due to errors in observations and the isochrones, many stars will appear to be of different ages than the correct age. The same is true with the onset of star formation, as the cutoff will be smoothed by the errors. Thus, in order to make a good fit, the onset of star formation must be determined first.

To do this, a set of solutions covering the possible ranges of distance, extinction, and enrichment history should be made, with high resolution at old ages (I recommend 1 Gyr resolution). If there are obvious limits as to the age (the lack of a horizontal branch, for example), you need not include bins older than that limit. The best fits should then be examined to determine the age at which the most significant drop in star formation rate takes place, and this should be assigned as the age of the onset of star formation. Note that you are not determining the time at which star formation truly began, only determining the time at which large amounts of star formation began. Low-level star formation earlier than that is certainly possible, but is generally impossible to distinguish from fitting errors and therefore is not worth solving for.

- Determine the global star formation history. To achieve maximum signal-to-noise, combine all data and run a set of star formation history solutions, covering the possible ranges of distance, extinction, and enrichment history. Analysis of the best-fitting solutions will not only return the star formation rates, but also the distance, extinction, and enrichment history and uncertainties in all values. You need to be careful of the time bins that are chosen. Bins too large will result in a lack of significant information about the star formation history because of too little resolution, but bins too small will have the same effect because of too much noise. Additionally, small bins will likely produce sharp features on the reconstructed CMDs, an error caused in an earlier version of Chapter 3 by the presence of a narrow 4-16 Myr bin.

  Monte Carlo simulations should also be run, in which you generate CMDs based on the determined parameters and star formation history, and then attempt to determine the star formation histories of those. This will help locate any systematic errors in the data, as well as constrain the uncertainties. As a sanity check (and error check), you should build a reconstructed CMD at the end of this to make sure that the star formation history solved for produces a CMD that is in agreement with the data. Any significant errors and their causes should be noted, and corrected if possible.

- Determine the local recent star formation histories. In general, a dwarf galaxy should have the same old star formation history in all fields, as stars older than a few Gyr should have mixed by now (not necessarily the case for larger spirals or ellipticals). For recent star formation, however, it is possible that different fields or regions may have quite different star formation histories. WLM (Chapter 3) and LGS 3 (Chapter 5) had spectacular differences between the inner and outer parts, while the LMC fields had significant but smaller differences. This solution should have higher resolution at the younger ages than the global solution above, with the resolution determined by number of stars and filters. VI data, while good for the old stars, does not lend itself to much less than 500 Myr resolution, as seen in the WLM and LGS data sets. BV data, on the other hand, allowed 100 Myr resolution in the LMC data, also because of the larger number of stars. Once again, a reconstructed CMD should be made for each region or field that was separately analyzed.

6.2 Star Formation Histories of Three Local Group Galaxies

Star formation history analyses of WLM, the LMC, and LGS 3 were made using the method and recipe described above. Photometric distances and extinction values for the three galaxies were determined, as well as star formation histories. The distances and extinctions were similar to and generally consistent with previous measurements for WLM and the LMC, but much different for LGS 3. They had smaller uncertainties due to the fact that it was the entire CMD being fit rather than just one part, such as the RGB tip or horizontal branch. The photometric measurements of metallicity were also generally consistent with earlier measurements (except for LGS 3), again with higher precision. The LGS 3 differences with previous findings are because of incorrect RGB tip distances of the previous studies.

The three star formation histories showed interesting similarities among the galaxies. WLM and the two LMC fields appear to contain no horizontal branch stars (or so few as to be undetectable), thus limiting large-scale star formation to no older than ~12 Gyr. LGS 3, on the other hand, does have horizontal branch, and an age of ~14.5 Gyr was determined for the beginning of its first large star formation episode. The initial large-scale star-forming episodes for all three appear to have been relatively short (no more than 2 Gyr), and with [Fe/H] between -1.4 and -1.5. LGS 3 seems to have ceased star formation shortly after this initial even ended, while both WLM and the LMC continued star formation with a star formation rate of between 5% and 10% of the average rate during the first Gyr of star formation. LGS 3 and the LMC show very definite increases in star formation recently (between 3.5 and 5 Gyr ago for LGS 3 and between 1 and 2.5 Gyr ago for the LMC). WLM is consistent with either a constant star formation rate since the initial burst ended about 11 Gyr ago, or a slight increase in the star formation rate during the last 1 Gyr. (Although given the large uncertainties in its star formation rates, WLM is also consistent with a picture like that for the LMC and LGS 3).

The star formation history observed for LGS 3 and the LMC are, in fact, very common in other studies of irregular galaxies. NGC 6822 (Gallart et al 1996), Leo A (Tolstoy et al 1998), and Sextans A (Dohm-Palmer et al 1997) all show histories where star formation appears to have followed the same pattern: an initial significant star-forming event, followed by a long (many Gyr) period of lower or no star formation, and finally a burst in the last few Gyr. The Pegasus dwarf irregular (Gallagher et al 1998) has a has a similar star formation history, but with a small but significant amount of star formation during the intermediate period. In fact, all but three of the irregular or intermediate dwarfs listed in a review by Grebel (1998) show a star formation history with a lower intermediate-age population, and higher recent and ancient star formation. One of the three others, interestingly, was LGS 3, which this HST-based study has shown to also share those characteristics. (WLM was another of the three in Grebel 1998, and the essentially constant star formation rate after an initial burst shown there is consistent with the results here.) Whether or not WLM conforms to this picture will be left for future HST-based studies that cover a larger fraction of the galaxy.

It also appears that many of the Local Group's spheroidals share this star formation history, with only a small number showing no evidence for star formation beyond the initial burst. The Carina dwarf spheroidal (Mighell 1997) shows the most dramatic evidence of this, as is seen with HST-based photometry extending well below the MS turnoff that shows two turnoffs. This picture of star formation in a dwarf galaxy is not universal, however. Other spheroidals, such as Ursa Minor (Mighell and Burke 1999), show a star formation history consisting of a single old burst.

The question of the cause of this star formation history is something that detailed galaxy evolution simulations will need to address. Either the galaxies ceased their initial star forming episodes before using up their gas which allowed star formation to begin at a later time after some event triggered it, or the galaxies used up their initial gas and accreted more at a later time.

6.3 Future Work

Future work in this field will involve two steps. One will be expanding the HST photometric data for Local Group dwarf galaxies, of which currently about 70% have HST broadband images. The second, an area with much work to be done, is the application of a uniform analysis technique, such as that described here, to the large amount of data already available, or at the very least ensuring that all data has been treated with fully objective methods (for example, the method outlined here and those in Tolstoy & Saha 1996 and Aparicio et al 1997).

This work could take two directions. First would be the expansion of the study of irregulars and intermediate-type galaxies. Very few have been studied with both HST-based data and fully objective methods, and developing a larger sample set from which to base generalizations would be extremely useful. For example, this work finds that all three galaxies show qualitatively similar star formation histories, with an initial significant star-forming event and a recent star-forming event. Is this common to all? Was there some significant event that occurred between 2 and 4 Gyr ago that triggered star formation throughout the Local Group?

In addition to expanding the work on irregulars and intermediate-type dwarfs, an expansion of the study of dwarf spheroidals would be interesting. A uniform study of their star formation histories could help to settle the question as to the distinction between dwarf irregular and spheroidal galaxies, and the role of the intermediate type galaxies as a bridge between the two classes. Specifically, do spheroidals show only an old population, or do they show an old population with one or more recent bursts? The former would put a distinction in the classification scheme between intermediate-type galaxies and dwarf spheroidals, while linking dwarf irregulars to intermediate-type galaxies an evolutionary chain. If, on the other hand, it was determined that many or most dwarf spheroidals had a recent star formation episode, the evolutionary chain would also include those galaxies.

It is noted that much of the proposed work has been done, but it is the combination of HST-based data and fully objective techniques, as well as the desire to have a uniform set of analyses, that well greatly aid in comparisons and generalizations.

BIBLIOGRAPHY

Ables, H. D. and Ables, P. G.: 1977, *Astrophys. J., Suppl. Ser.* **34**, 245

Aparicio, A., Gallart, C., and Bertelli, G.: 1997, *Astron. J.* **114**, 680

Balona, L. A. and Jerzykiewicz, M.: 1993, *Mon. Not. R. Astron. Soc.* **260**, 782

Bertelli, G., Mateo, M., Chiosi, C., and Bressan, A.: 1992, *Astrophys. J.* **388**, 400

Burstein, D. and Heiles, C.: 1984, *Astrophys. J., Suppl. Ser.* **54**, 33

Butcher, H.: 1977, *Astrophys. J.* **216**, 372

Chaboyer, B., Demarque, P., and Sarajedini, A.: 1996, *Astrophys. J.* **459**, 558

Charlot, S., Worthey, G., and Bressan, A.: 1996, *Astrophys. J.* **457**, 625

Christian, C. A. and Tully, R. B.: 1983, *Astron. J.* **88**, 934

Cole, A. A.: 1998, *Astrophys. J.* **500**, L137

Dohm-Palmer, R. C., Skillman, E. D., Saha, A., E.Tolstoy, Mateo, M., Gallagher, J., Hoessel, J., Chiosi, C., and Dufour, R. J.: 1997, *Astron. J.* **114**, 2527

Dolphin, A. E. and Hunter, D. A.: 1998, *Astron. J.* **116**, 1275

Fagotto, F., Bressan, A., Bertelli, G., and Chiosi, C.: 1994, *Astron. Astrophys. Suppl. Ser.* **105**, 29

Ferraro, F., Pecci, F. F., Tosi, M., and Buonanno, R.: 1989, *Mon. Not. R. Astron. Soc.* **241**, 433

Flower, P.: 1976, PhD dissertation, University of Washington

Gallagher, J. S., Tolstoy, E., Dohm-Palmer, R. C., Skillman, E. D., Cole, A. A., Hoessel, J. G., Saha, A., and M.Mateo: 1998, *Astron. J.* **115**, 1869

Gallart, C., Aparicio, A., Bertelli, G., and Chiosi, C.: 1996a, *Astron. J.* **112**, 1950

Gallart, C., Aparicio, A., and Vilchez, J. M.: 1996b, *Astron. J.* **112**, 1928

Geha, M. C., Holtzman, J. A., Mould, J. M., Gallagher, J. S., Watson, A. M., Cole,

A. A., Grillmair, C. J., Stapelfeldt, K. R., Ballester, G. E., Burrows, C. J., Clarke, J. T., Crisp, D., Evans, R. W., Griffiths, R. E., Hester, J. J., Hoessel, J. G., Scowen, P. A., Trauger, J. T., and Westphal, J. A.: 1998, *Astron. J.* **115**, 1045

Girardi, L., Bressan, A., Chiosi, C., Bertelli, G., and Nasi, E.: 1996, *Astron. Astrophys. Suppl. Ser.* **117**, 113

Graham, J. A.: 1982, *Publ. Astron. Soc. Pac.* **94**, 244

Grebel, E. K.: 1998, in P. Whitelock and R. Cannon (eds.), *The Stellar Content of Local Group Galaxies, IAU Symposium 192*, p. 1, Astronomical Society of the Pacific, San Francisco

Greggio, L., Marconi, G., Tosi, M., and Focardi, P.: 1993, *Astron. J.* **105**, 894

Hodge, P. and Miller, B. W.: 1995, *Astron. J.* **451**, 176

Holtzman, J. A., Burrows, C. J., Casertano, S., Hester, J. J., Trauger, J. T., Watson, A. M., and Worthey, G.: 1995, *Publ. Astron. Soc. Pac.* **107**, 1065

Holtzman, J. A., Mould, J. R., Gallagher, J. S., Watson, A. M., Grillmair, C. J., Ballester, G. E., Burrows, C. J., Clarke, J. T., Crisp, D., Evans, R. W., Griffiths, R. E., Hester, J. J., Hoessel, J. G., Scowen, P. A., Stapelfeldt, K. R., Trauger, J. T., and Westphal, J. A.: 1997, *Astron. J.* **113**, 656

Karachentseva, V. E.: 1976, *Comm. Special Obs.* **18**, 42

Kim, S., Staveley-Smith, L., and Dopita, M. A.: 1998a, in T. Richtler and J. M. Braun (eds.), *The Magellanic Clouds and Other Dwarf Galaxies, Proceedings of the Bonn/Bochum-Graduiertenkolleg Workshop*, p. 169, Shaker Verlag, Aachen

Kim, S., Staveley-Smith, L., Dopita, M. A., Freeman, K. C., Sault, R. J., Kesteven, M. K., and McConnell, D.: 1998b, *Astrophys. J.* **503**, 674

King, I. R.: 1965, *Astron. J.* **71**, 64

Krist, J.: 1995, in R. A. Shaw, H. E. Payne, and J. J. E. Hayes (eds.), *Astronomical Data Analysis Software and Systems IV*, p. 349, Astronomical Society of the Pacific, San Francisco

Landolt, A. U.: 1973, *Astron. J.* **78**, 959

Landolt, A. U.: 1983, *Astron. J.* **88**, 439

Lee, M. G.: 1995, *Astron. J.* **110**, 1129

Lee, M. G., Freedman, W. L., and Madore, B. F.: 1993, *Astrophys. J.* **417**, 92

Lee, Y.-W., Demarque, P., and Zinn, R.: 1994, *Astrophys. J.* **423**, 248

Lucke, P. B.: 1972, PhD dissertation, University of Washington

Massey, P. and Davis, L. E.: 1992, *A User's Guide to Stellar CCD Photometry with IRAF*

Mateo, M.: 1998, *Ann. Rev. Astron. Astrophys.* **36**, 435

Melotte, P. J.: 1926, *Mon. Not. R. Astron. Soc.* **86**, 636

Mighell, K. J.: 1997, *Astron. J.* **114**, 1458

Mighell, K. J. and Burke, C. J.: 1999, *Astron. J.* **116**, in press

Minniti, D. and Zijlstra, A. A.: 1997, *Astron. J.* **114**, 147

Mould, J.: 1997, *Publ. Astron. Soc. Pac.* **109**, 125

Olsen, K. A. G.: 1998, PhD dissertation, University of Washington

Olszewski, E. W., Suntzeff, N. B., and Mateo, M.: 1996, *Ann. Rev. Astron. Astrophys.* **34**, 511

Pagel, P. E. J. and Tautvaisiene, G.: 1998, *Mon. Not. R. Astron. Soc.* **299**, 535

Panagia, N.: 1998, *IAU Symposium* **190**, 53

Sandage, A. and Carlson, G.: 1985, *Astron. J.* **90**, 1464

Sandage, A. and Tammann, G.: 1974, *Astrophys. J.* **191**, 603

Schaller, G., Schaerer, D., Meynet, G., and Maeder, A.: 1992, *Astron. Astrophys. Suppl. Ser.* **96**, 269

Schild, R.: 1980, *Astrophys. J.* **242**, 63

Schlegel, D. J., Finkbeiner, D. P., and Davis, M.: 1998, *Astrophys. J.* **500**, 525

Stappers, B. W., Mould, J. R., Sebo, K. M., Holtzman, J. A., Gallagher, J. S., Watson, A. M., Ballester, G. E., Burrows, C. J., Casertano, S., Clarke, J. T., Crisp, D., Griffiths, R. E., Hester, J. J., Hoessel, J. G., Scowen, P. A., Stapelfeldt, K. R., Trauger, J. T., and Westphal, J. A.: 1997, *Publ. Astron. Soc. Pac.* **109**, 292

Stetson, P. B.: 1987, *Publ. Astron. Soc. Pac.* **99**, 191

Tolstoy, E.: 1996, *Astrophys. J.* **462**, 684

Tolstoy, E., Gallagher, J. S., Cole, A. A., Hoessel, J. G., Saha, A., Dohm-Palmer, R. C., Skillman, E. D., Mateo, M., and Hurley-Keller, D.: 1998, *Astron. J.* **116**, 1244

Tolstoy, E. and Saha, A.: 1996, *Astrophys. J.* **462**, 672

Tosi, M., Greggio, L., Marconi, G., and Focardi, P.: 1991, *Astron. J.* **102**, 951

Wolf, M.: 1909, *Astron. Nachr.* **183**, 187

Young, L. M. and Lo, K. Y.: 1997, *Astrophys. J.* **490**, 710

Appendix A

HSTPHOT

To better conduct photometry using HST WFPC2 data, it was necessary to write a new photometry package which accounted for the undersampled nature of the data. In addition to having a variable point spread function (PSF) caused by the position of a star on the chip (which standard packages such as DAOPHOT incorporate), it is also necessary to have a variable PSF caused by the position of a star on a pixel. For example, a star centered on the center of a pixel will have a significantly different PSF from a star centered on the edge of a pixel.

The first step was to build a library of synthetic PSFs, for which Tiny Tim 4.0 (Krist 1995) was used. PSFs were calculated at 64 positions on each chip in F555W and F814W, subsampled at 20 per pixel in the WF chips and 10 in the PC chip. Jitter was added to the images as recommended by Krist (1995) to account for charge diffusion effects near the edges of the pixels. These PSFs were then binned to one bin per pixel, for a range of different star positions within a chip. A 10x10 grid of possible centerings was used for the WF chips and a 5x5 grid was used for the PC chip (again, with 64 positions on each chip) for a total of 20,800 total PSFs in the library for each filter.

Before photometry could proceed, a sky image was calculated, using a robust median procedure. The mean of all pixels in a square around each pixel is calculated, with an iterative process discarding all pixels beyond 2.5σ of the mean. This sky image was then subtracted from the observed image (although the original observed image was retained for uncertainty purposes).

The first step in the photometry was to locate all stars, which was done by finding local maxima in raw counts and then by centering by convolving the data with the appropriate PSFs from the library. The PSF and pixel centering giving the highest signal-to-scatter (scatter determined with a χ^2 calculation) was selected as the star's preliminary center. A preliminary count rate was also determined for each. Once this process was completed, all located stars were subtracted from the image, using their preliminary PSF positions and count rates.

The solution for the PSF was then done with an iterative process. At the start of each iteration, any two stars within a certain distance were combined (adjusting the star subtraction as necessary). The routine then went through the list of stars, adding each star to the image, re-determining the photometry, and re-subtracting the star. If a star's photometry changed significantly, all surrounding stars were flagged as requiring another iteration. This process was then repeated until all stars converged.

A remarkable degree of positional accuracy was obtained through this fitting process. The positional determinations were tested by application to the Leo A WFPC2 data set (Tolstoy et al 1998), for which all images were taken with slightly different centerings (up to .25 arcsec difference). The fields had to be aligned, therefore, something done by attempting to match all stars with V magnitudes of 25 or brighter or I magnitudes of 24 or brighter. When aligning the photometry from the six F555W and F814W images, the PC stars (the 5x5 grid) had a 1σ scatter of 0.14 pixels and the WF stars (the 10x10 grid) had a 1σ scatter of 0.08 pixels. Thus the positional accuracy with this method is approximately 7-8 milliarcsec, and presumably could be increased if a grid of PSFs with higher resolution was calculated, as the grid size (10 milliarcsec difference between adjacent PSFs) accounts for nearly all of the scatter. For fainter stars, of course, the noise from photon statistics will dominate.

At the end of the process, a position, count rate, and χ^2 for each star was recorded. The count rate was adjusted for the CTE effect and calibrated as described in Holtzman et al (1995). A comparison between HSTPhot photometry of Leo A and the Tolstoy et al (1998) photometry from DOPHOT is shown in Figures A.1 and A.2.

The HSTPhot diagram contains only stars found in two of the three images for each filter with χ values for the PSF fit of less than 2. A number of improvements in the CMD are apparent. Most notably is the region to the red of the RGB, which the relatively large number of stars in the DOPHOT photometry might have led one to postulate differential reddening. The lack of those stars in the HSTPhot data indicates that they were most likely caused by cosmic rays, blended stars, or poorly fit PSFs. The red clump is significantly tighter in the HSTPhot results. Additionally, the space between the main sequence and RGB/BL contains fewer stars (especially between I=24 and I=25), helping to distinguish the features more cleanly and increasing confidence that the stars remaining in that region may be real (such as the possible MS turnoff at I=23.8, corresponding to an age of 670$\pm$40 Myr). The red supergiant feature is also much more sharply defined in the HSTPhot CMD.

A second comparison, this with DAOPHOT, is made in Figure 2.7.

The package also contains an artificial star routine, the results of which were used both for completeness corrections and for the generation of synthetic CMDs simulating the observed data quality. When running the tests, each star was added individually and analyzed, so as to minimize the cumulative effect of a large number of stars being added to a single image and thus altering the crowding of the image. In all work described here, enough artificial stars were used so that the number of observed stars was always the limiting statistical factor. The artificial star tests were made in both filters, allowing the construction of a database of results for any chip, position, magnitude, and color.

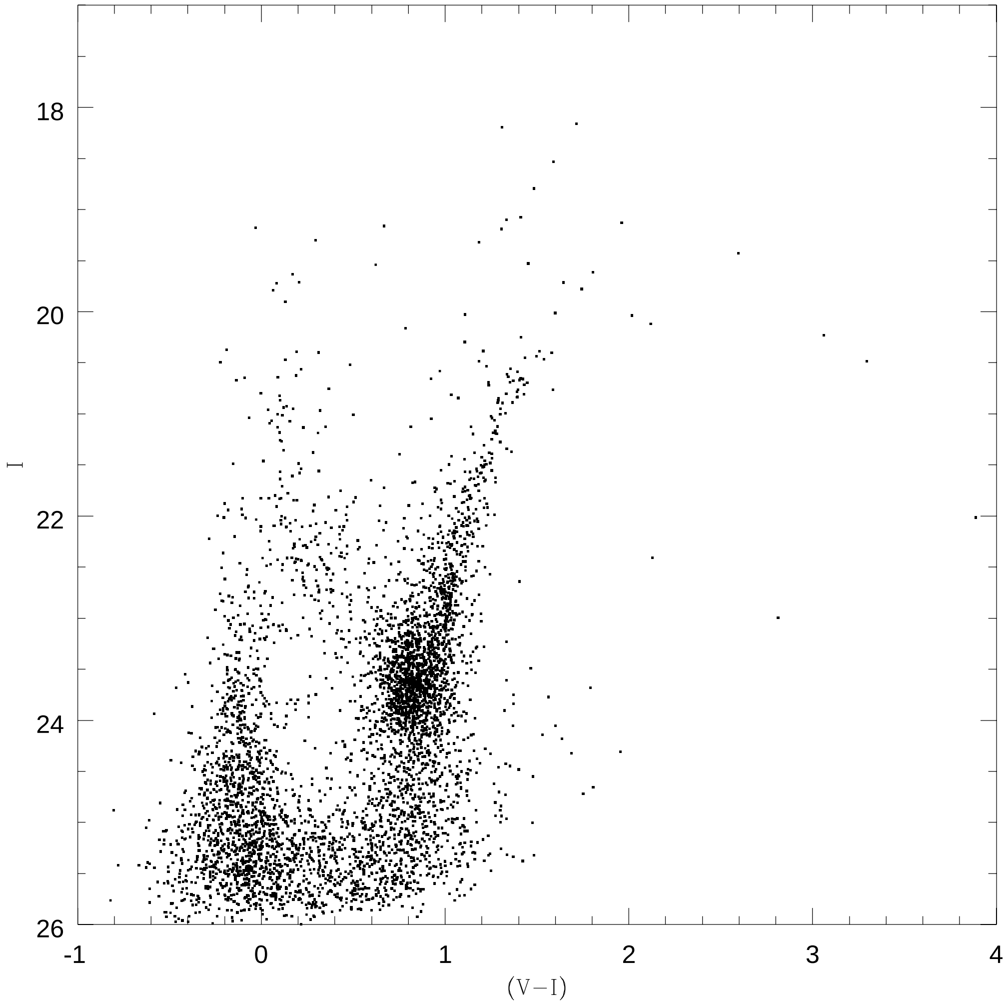

Figure A.1: $V-I, V$ CMD from all four WFPC2 chips for Leo A, as determined here by HSTPhot

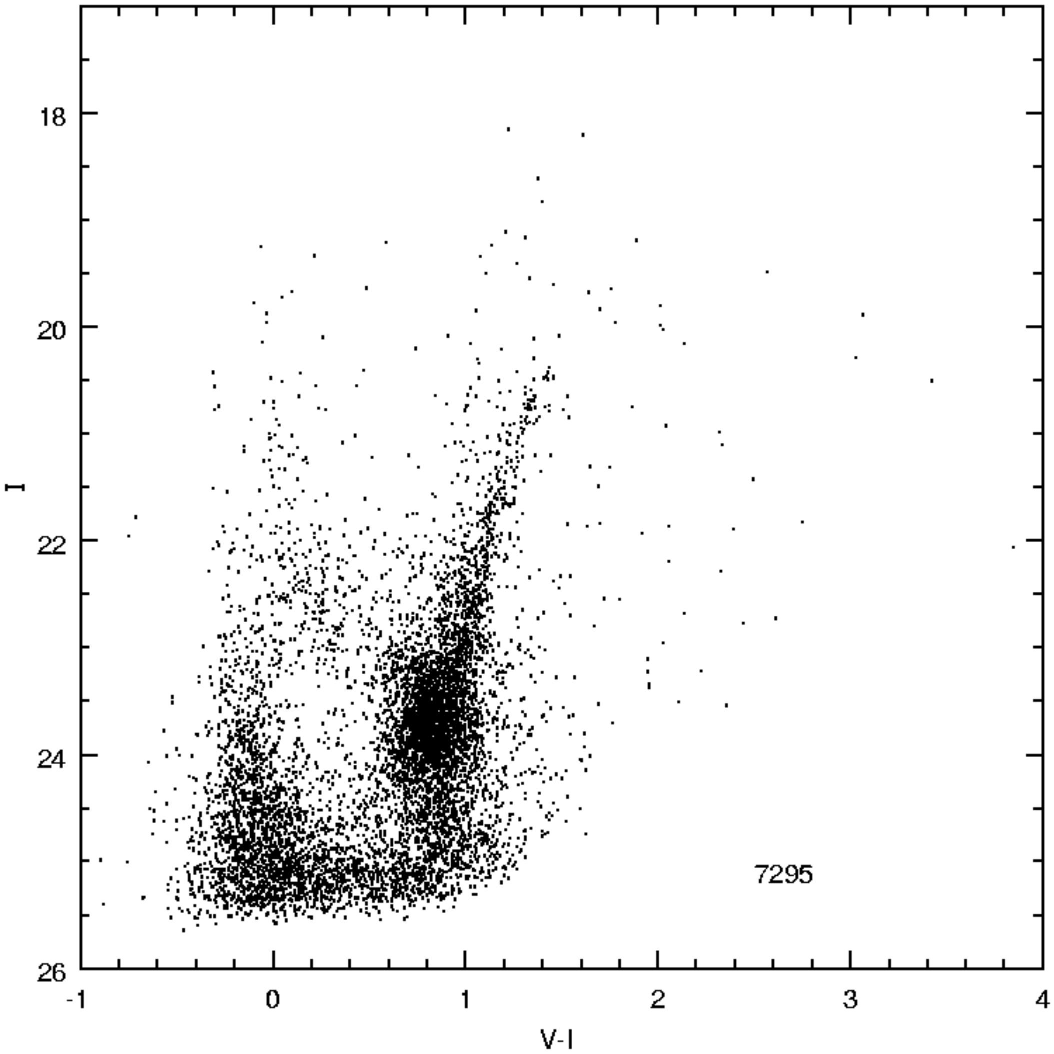

Figure A.2: $V-I, V$ CMD from all four WFPC2 chips for Leo A, from Tolstoy et al (1998)

VITA

Andrew Eugene Dolphin was born on June 30, 1972 in Bremerton, WA to Eugene and Penny Dolphin. As part of a navy family, he grew up all over the United States, living in Washington, Illinois, California (twice), Virginia, and North Carolina. His interest in astronomy began at age 7, when during one of many moves he discovered a small (two-inch) telescope the family owned and had forgotten. Upon receiving a thirteen inch telescope for Christmas one year, he and his father became hooked on backyard astronomy, a hobby both continue to enjoy. He graduated with high distinction with a B.S. in Physics from Harvey Mudd College in 1993, and immediately began graduate school at the University of Washington. Within a year of arriving in Seattle, he began working with Paul Hodge on stellar population studies and on galaxy evolution, the former becoming this dissertation. In addition to studying stellar populations, he is studying for a Master of Music in choral conducting with Abraham Kaplan.